Molecular beam mass spectrometric investigation of plasma-material interactions motivated by plasma-catalysis

A DISSERTATION SUBMITTED TO THE FACULTY OF THE GRADUATE SCHOOL OF THE UNIVERSITY OF MINNESOTA

BY

Jingkai Jiang

IN PARTIAL FULFILLMENT OF THE REQUIREMENTS FOR THE DEGREE OF DOCTOR OF PHILOSOPHY

Advisor: Prof. Peter J. Bruggeman

January, 2022

Acknowledgments

Time files and it has been four and half years since I started my Ph.D. program. The day when I had the new student orientation in Room 1130 of ME building was just like yesterday. I could still remember my feelings of nervousness and excitement at that time. I truly believe that, when feeling a time runs very fast, it means this journey was focused, fruitful, and enjoyable.

Firstly, I would like to acknowledge the funding sources to support my Ph.D. studies, from the University of Minnesota through the Mechanical Engineering Department Fellowship and the teaching assistantship (2017 Fall, 2018 Fall), from the National Science Foundation under the award number CBET 1703439, and the US Department of Energy, Office of Science, Office of Fusion Energy Sciences General Plasma Science Program under award numbers DE-SC-0020232, DE-SC0001939 and DE-SC0016053,

I might have not known what plasma was if I missed the recruiting seminar where I met Prof. Peter J. Bruggeman. It might be a fortune and I felt so lucky to join his group without

any background knowledge of plasma. I would like to express my dedicated thanks to my advisor, Prof. Bruggeman, who led me into the world of plasma and gave me the courage and very detailed guidance during the past four and half years. Every conversion with him not only enriched my understanding of research but also opened my mind in solving problems. His hardworking and rigorous attitude in research greatly inspire me and motivate me. It was an enjoyable experience to be advised by him and work with him.

I would also like to express my gratitude to Dr. Yolanda Aranda Gonzalvo, who offered me great help in building the molecular beam mass spectrometer system, who trained me using this system, who taught me a lot in performing experiments. Her great help smoothed my Ph.D. periods and definitely, I could not finish as much work as I finished without her help and guidance.

Furthermore, I would like to extend my thanks to all of my labmates for all the great help, collaboration, and insightful and interesting conversion. I enjoyed the unforgettable events, conference travel we had together. Even during the COVID-19 pandemic in 2020, the happiness in those virtual parties offered me vitality and hope after being locked down long time at home. Thanks to Yuchen Luo, Marien Semeni Semeni, Vighneswara Siva Santosh Kumar Kondeti, Gaurav Nayak, Ankit Moldgy, Yuanfu Yue, Jianan Wang, Stephen Exarhos, Tanubhav Kumar Srivastava, Brian Bayer, Sahil Mahajan, Samyak Jain and all the visiting scholars in our lab.

I would also like to thank all the people in CSE workshop who help me with my projects, Ronald Bystrom and Peter Ness, and others whose names are not listed here. As a mechanical engineer, I learned a lot about machining and designing from the CSE workshop.

To my collaborators, Prof. Oehrlein's group at the University of Maryland, Prof. Adamovich's group at the Ohio State University, and many other groups in PSC and PICI centers, I am grateful for their helpful discussion and suggestions regarding my research projects. To Prof. Kushner at the University of Michigan, I sincerely thank him for providing the GLOBALKIN codes used in this dissertation. I acknowledge the Minnesota Supercomputing Institute (MSI) at the University of Minnesota for providing resources that contributed to the results reported in this dissertation.

To my committee members Prof. Chris Hogan, Prof. Steven Girshick, and Prof. Aditya Bhan, I am grateful for their feedback and guidance in my research. Many thanks for their time for reviewing my dissertation and providing valuable insights and suggestions.

To our parents and families, I would like to thank them for their understanding and support in any decision I made. They always encourage me and let me pursue my dreams. No matter success or failure, I know that they are always there for me.

Lastly, but most importantly, I would like to express my greatest thanks to my wife, Yilin Liu. Yilin and I came together to the U of Minnesota to pursue our Ph.D. degrees in 2017. She gave me a lot of help during my Ph.D. period, not only in life but also in research work. We had a lot of valuable discussions on research and presentation slides which were extremely helpful to improve me. Also, she supported me for being gone for a 3-month internship to have an industrial experience. She is always my supporter and source of encouragement when I met failure. She is my lover as well as my best friend, without whom I could not make this possible. I am looking forward to our further endeavors, together!

Dedication

To my wife Yilin Liu and our families.

Abstract

Low-temperature atmospheric pressure plasmas are a source of many different highly reactive species that enable a variety of plasma-material processing applications. Nonetheless, the non-equilibrium nature and limited indirect tuning possibilities make it difficult to control reactive species production, particularly for atmospheric pressure plasmas. The underlying mechanisms of plasma-material interactions are currently not fully understood and more in-depth insights of the plasma-material interaction mechanisms would be beneficial for the advancement of several applications enabled by atmospheric pressure plasmas.

For a better control and optimization of the plasma sources, quantitative measurements of these plasma-produced gas-phase reactive species are needed as a starting point. Molecular beam mass spectrometry (MBMS) was used in this study as a powerful diagnostic technique to perform *in-situ* measurements of both long-lived and short-lived (radicals, ions) species fluxes at the plasma-material interface. An adjustable MBMS system was designed, built and implemented to fulfill optimal conditions of both neutral and ionic species measurements. Firstly, considering that the MBMS sampling is intrusive, the influence of the flow fields in free and substrate-impinging atmospheric pressure plasma jets (APPJs) on the distribution of reactive species density was investigated and models to account for reactions in the near surface boundary layer were developed. In addition, the capability of MBMS was further extended by developing detection and calibration approaches for the absolute measurement of singlet delta oxygen, $O_2(a^1\Delta_g)$ the first electronically excited state of O_2, vibrationally-excited nitrogen $N_2(v)$, as well as the

absolute density of ions. These advances enabled the following key findings reported in the first part of the thesis.

- The MBMS measurements of $O_2(a^1\Delta_g)$ showed that $O_2(a^1\Delta_g)$ is the dominant reactive species in the effluent of an RF-driven atmospheric pressure plasma jet (APPJ). The ability to measure axial and radial profiles of $O_2(a^1\Delta_g)$ impinging on a substrate in the effluent of the APPJ is a key advantage of the MBMS diagnostic method over well-established optical diagnostics.
- The spatially resolved measurements of $N_2(v)$ in the effluent of an APPJ were enabled by fitting the mass spectrometry signals with the electron-impact ionization cross sections of $N_2(v)$ as a function of electron energy, assuming a Treanor-like vibrational distribution function. The approach provides a complementary diagnostic technique for detecting $N_2(v)$ near substrates with excellent spatial resolution and detection limits, and also shows that RF-driven plasmas can produce large fluxes of vibrationally-excited nitrogen that is reported to be important in plasma catalysis.
- Absolute densities of positive ions in the effluents of an APPJ were obtained through calibration with a dc corona discharge with a well-known current density profile [3]. Positive ion densities in the effluent of the APPJ were found to be more than 4 orders of magnitudes lower than the densities of the dominant reactive neutral species (O, $O_2(a^1\Delta_g)$, O_3) in the afterglow region suggesting that plasma-surface interactions in this case are dominated by neutral radical interactions.

These results are examples of extended diagnostic capability in atmospheric pressure plasma that have a large potential to enable a better understanding of plasma-surface interactions.

With the established MBMS, the control of plasma produced species fluxes by tuning plasma operating parameters as well as the ion dynamics in the effluents of APPJs were also investigated in the second part of the thesis.

An extensive parameter study shows that for a fixed feed gas composition and plasma dissipated power, the ratio of short-lived (O, ions) and long-lived (O_3 and singlet oxygen) species fluxes can be changed by orders of magnitude by changing the treatment distance and the plasma modulation frequency. Furthermore, changing the gas flow rate is found to be potentially an effective approach to tune the ratio of the O and ion fluxes. The results presented in this contribution can be a valuable tool to control the reactive species fluxes to substrates by tuning plasma operating parameters for plasma-surface interactions.

A characterization of ion fluxes impinging on substrates as produced by a modulated RF-driven APPJ operating in a homogenous gas environment (Ar+1% O_2) was performed using MBMS. The influence of the RF modulation frequency (100 Hz-20 kHz) upon the ion fluxes was investigated by time-resolved measurements, and lifetimes of the dominant ions were obtained. Significant differences in the dynamics of the positive and negative ions were found and explained by large electron densities in the afterglow produced by electron detachment reactions from negative ions due to the large concentrations of atomic oxygen and singlet delta oxygen. Quantitative measurements of the ion densities causing these memory effects were reported. The results highlight the tremendous impact of

memory effects on plasma propagation and their corresponding pre-ionization densities which were measured for the first time.

The third part of this dissertation focuses on the interaction of plasma and catalysts in the context of partial oxidation of methane. Promising plasma catalysis synergy effects are observed for the conversion of chemicals, showing enhanced conversion compared with the plasma-only or catalysis-only conditions. The underlying mechanisms responsible for these highly beneficial synergistic effects are to date not understood but are typically suggested to be due to the production of reactive species. The established MBMS enabled the quantitative *in situ* measurements and a better control of reactive species (reactive neutral species and ions) in the gas phase which are needed to understand the fundamental mechanism of plasma-catalyst interaction. The MBMS results were correlated with the *in situ* measurements of changes in surface properties by collaborators at the University of Maryland. The key finding of this collaborative work is that a strong correlation between atomic O flux and CH_4 conversion was identified suggesting its importance for the oxidation of CH_4 to CO and CO_2, and that the formation of surface CH_n might be the rate-determining step of the production of CO and CO_2 at 500 ^oC in plasma catalysis. In addition, we showed for oxygenates that the heating effects initiated by the plasma significantly impacted the desorption rates of methanol from particle surfaces but the contribution from thermal catalysis was excluded. MBMS measurements and estimates of species lifetimes suggested that the synergistic effect in methanol production was caused by radical species most likely CH_3O_2, indicating surface reactions induced by secondary more long-lived radicals such as alkylperoxy radicals might be less impacted by transport limitations.

Contents

List of Table

List of Figures

Chapter 1

Introduction

Plasma is the fourth state of matter which is characterized by the presence of charged species (e^--ions). The electron (ion) density can vary up to 30 orders of magnitude. Electric fields accelerate charged species and energy can be transferred to free electrons much faster than ions due to their large mass difference. When the energetic electrons collide with neutral gas molecules, elastic or inelastic collisions could happen resulting in gas heating or chemical reactions, respectively. Low-temperature plasma (LTP) is a partially ionized gas where the temperatures of the electrons is significantly larger than the heavy particles. This non-equilibrium state consists of a complex composition of reactive species containing ionized and excited states of atoms, molecules and radicals. In recent decades, atmospheric pressure plasmas are of great interests to researchers and have been widely used for a variety of applications including material processing [1], decontamination [2] and environmental remediation [3]. The majority of applications relies on reactions introduced by the plasma produced reactive species. Hence, in order to better control and optimize the plasma sources, quantitative measurements of these reactive species are beneficial. The focus of this dissertation is to quantitatively characterize the reactive species produced by plasma at the plasma-surface interface, to help revealing the mechanism of plasma-surface interaction with a goal to improve applications and exploit their full potential.

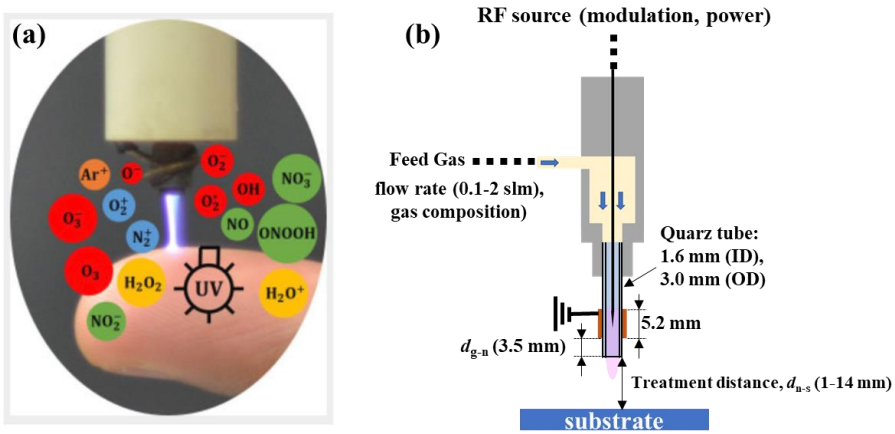

Figure 1.1: (a) Picture of a low-temperature atmospheric pressure plasma jet; (b) schematic of the APPJ used in this work.

In this chapter, different plasma sources operating at atmospheric pressure are introduced but the main content will be focusing on the atmospheric pressure plasma jets (APPJs) (Sec. 1.1). A description of the key diagnostic tool employed in this study, the molecular beam mass spectrometer (MBMS), is described (Sec. 1.2). Next, recent findings associated with the mechanisms of plasma-catalyst interaction are reviewed in Sec. 1.3. The motivation & objectives and the organization of this dissertation are described in Sec. 1.4 and Sec. 1.5, respectively.

1.1 Atmospheric pressure plasma sources

Many LTPs are operating at reduced pressures in the range of 10s mTorr to a few Torr, such as those used in the semiconductor industry [4]. In the recent decades, many atmospheric pressure plasma sources have been developed to reduce the cost of plasma processing, moving the processing pressure from vacuum to atmospheric pressure. Meanwhile, atmospheric pressure operation also extends the scope of possible applications of plasma processing. Substrates that are not vacuum compatible including living matter

now can be treated using the atmospheric pressure plasma. In addition, processes requiring high pressure such as catalysis become also possible.

There are many plasma sources operating at atmospheric pressure based on different principles, including corona discharge, gliding arc discharge, dielectric barrier discharge (DBD), RF-driven plasmas and microwave discharges [5]. Due to the numerous collisions between molecules at atmospheric pressure, the energy deposited in the plasma leads to gas heating, which can be an issue to temperature-sensitive applications. Therefore, different strategies are used to limit the averaged current in the plasma circuit to constrain the plasma operating in the glow discharge. For example, the use of high-voltage pulses with a duration of nanoseconds to microseconds to drive plasma, enables the gas temperature in many cases to maintain near room temperature. Another typical example is the DBD, one or both electrodes in this case are covered with dielectric materials. When the dielectric materials are fully charged, there will be no electrical fields across the gas to sustain the plasma making the plasma intrinsically self-limiting. Similarly, Some RF-driven discharges also use this strategy but their driving frequency (MHz) is higher than DBD (typically a few kHz). Nevertheless, for those applications which are not temperature-sensitive or even high gas temperature are favorable, gliding arc or microwave plasma might be ideal candidates. In short, the available atmospheric pressure plasma sources have highly different properties, which are beneficial to be applied to a broad range of applications and suitable plasma sources ought to be chosen based on the specific requirements of each application.

As one of the most popular plasma devices, APPJs are usually driven by RF or DC-high voltages. A few reviews on atmospheric pressure plasma jets can be found in [6]–[8].

In an APPJ the plasma is produced inside a capillary tube and gas convectively transports plasma-produced reactive species towards a substrate as shown in figure 1.1 [9]. In many cases the APPJ operates in a noble gas (He/Ar) surrounded by open air and the plasma extends outside the capillary tube and is referred to as 'plasma plume'. This plasma plume is often a propagating ionization wave. Such ionization waves lead to an optical emission structure that resemble the movement of a bullet despite that the plasma plume (on time-averaged) looks to be continuous observed by eye. The emission (photons) out of the tube originates from electronically excited molecules/atoms, produced by electron excitation. The lifetimes (radiative and collisional) of limiting electronically excited states at atmospheric pressure are usually on the order of 10 ns or less, leading to the distinct bullet formation. Reactive species including radicals and ions that are longer lived (up to microseconds) can be produced in the plasma plume, but also convectively transported from the region inside the capillary tube to the effluents. Two key advantages of APPJs are (1) the treatment zone and plasma operation zone are separate leading to larger controllability of the plasma and reactive species fluxes and (2) APPJ enable local substrate treatments, which are of importance for some applications. In addition, the APPJs can be operated in direct contact with the treated substrates or remotely. The direct contact refers to the plasma plume touching the substrates. Depending on the dielectric properties of the substrates, the plasma properties might be affected changing from the glow discharge to a stronger conducting channel. Details of this direct contact with substrates can be found in the reference [10]. As for the remote treatment, the tip of the plasma plume is not in direct contact with the substrate and in such case, the treatment is largely independent of the substrates. According to the different lifetimes of reactive species, short-lived species like

ions and radicals are more abundant in the direct treatment. On the other hand, the long-lived species are more dominant in the remote treatment. Hence varying the distance between APPJ nozzle and substrate enables the separation of short-lived and long-lived species.

The plasma source and typical plasma operation conditions used in this work are briefly introduced in this section. As shown in figure 1.1(b), the plasma jet was composed of a tungsten needle electrode with a diameter of 1 mm inside a cylindrical quartz tube. This tungsten needle was sharpened at one end to increase the electric field strength. The outer diameter (ID) of the quartz was fixed at 3 mm but the inner diameters (ID) vary in the range of 1.6-1.8 mm in the subsequent chapters. A copper ring was positioned outside the quartz tube and served as the ground electrode. The distance between the ground electrode and the quartz tube nozzle (marked as d_{g-n}) can be tuned to prevent the arcing formation and keep the plasma diffusive. A radio frequency (RF) sinusoidal voltage at a frequency near 13.56 MHz was used to drive the plasma, and a homemade matching box consisting of an inductor was used in the circuit to tune the power matching between the plasma with the source. In addition, the RF modulation was also implemented with different modulation frequencies and cycles for specific purposes, which will be introduced in detail in the following chapters. Typical values of all the tunable plasma operation parameters including feed gas composition, gas flow rate, modulation frequency and duty cycle, plasma dissipated power and treatment distance (marked as d_{n-s}) are all indicated in figure 1.1(b). Specific plasma conditions will be described in each chapter.

1.2 Molecular beam mass spectrometry

Molecular Beam Mass Spectrometry (MBMS) is used in this study to perform *in situ* measurements of the species fluxes produced by the plasma. MBMS is a powerful diagnostic method for near-substrate plasma processing characterization. Different from the commercial mass spectrometry devices using capillary inlet tubes to guide sampling species, MBMS has the ability to detect short-lived reactive species such as ions and radicals without conversion reactions due to many collisions inside the capillary tubes. Compared with for example optical laser diagnostic methods, MBMS has the advantage to be able to detect various species simultaneously including ions and to measure species fluxes or densities at the plasma-sampling orifice/substrate interface. This will allow linking the obtained results directly with plasma-surface interactions while densities from laser diagnostics require assumptions for the transport of the measured reactive species density at the measurement position to the interface. Hence, MBMS is one of the most powerful and promising diagnostic methods to help us obtain a fundamental understanding of the mechanism of plasma produced species near the substrate.

The existing commercial MBMS systems or the systems reported in the literature [11]–[13] are not able to provide optimized conditions for both neutral and ionic species measurements in a single system. The reason is that the sampling approach for measuring neutral and ionic species is not the same. In this section, we described the details of an adjustable MBMS system (built at the University of Minnesota) at the start of my PhD studies to enable the measurement with good sensitivity of both neutral and ionic species from LTPs.

1.2.1. Molecular Beam

The intensity of the created molecular beam reaching the mass spectrometer (MS) is a key factor in determining the sensitivity (and detection limit) of the whole system. At atmospheric pressure, the mean free path of the gas molecules is around ~70 nm, which is much smaller compared to the sampling orifice (typically 20-200 μm). Hence the Knudsen number defined as Eq. (1.1) is much smaller than 1, meaning that the sampling flow at the atmospheric side belongs to the continuum flow region.

$$Ku = \frac{\lambda}{L_c} \ll 1 \tag{1.1}$$

The gas mixture entering the sampling orifice will have an underexpanded, supersonic, continuum jet expansion. The molecular beam is created by this free jet expansion from a high-pressure gas source to a low-pressure background that determines the possible existence of a shock wave in the expansion. Two cases are described in [14] for different background pressures. For our design, due to the large ratio of source pressure to the background pressure (about 400,000), a smooth transition from continuum to free molecular flow after the supersonic expansion will occur without shock. This is because the local mean free path of the molecules during the expansion is considerably larger than the distance between the sampling orifice and the orifice of the first skimmer [15]. For the shock-free expansion, a "quitting surface model" was developed in [14] which assumes the flow transit from continuum flow region to the free molecular flow at the quitting surface, as shown in figure 1.2. An empirical relationship for the location of the quitting surface is also presented in [14]:

$$\frac{X_{qs}}{d} \sim \left(\frac{M_\infty}{C_1}\right)^{\frac{1}{(\gamma-1)}} \tag{1.2}$$

where X_{qs} represents the location of the quitting surface, d is the diameter of the sampling orifice, M_∞ is the terminal Mach number which is equal to $M_\infty = 1.17\ Kn_o^{-0.4}$ (Kn_o means the Knudsen number at the orifice), C_1 is a constant related to gas species. The specific design parameters related to the creation of the molecular beam will be calculated and shown in the next section.

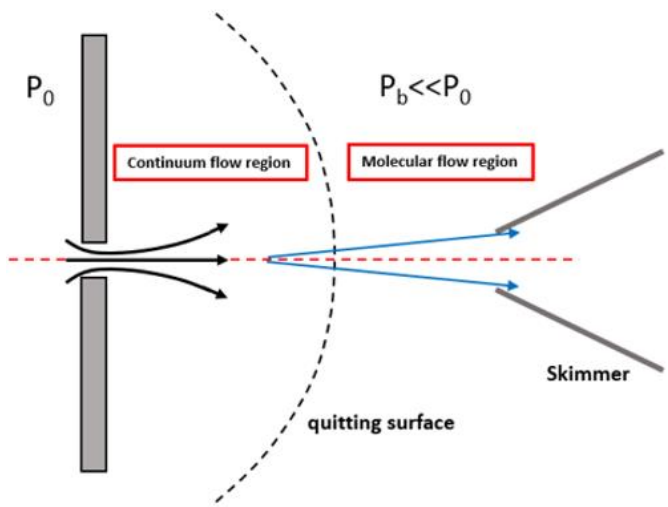

Figure 1.2: Continuum free-jet expansion under low background pressure in the reduce pressure stage.

1.2.2. MBMS system design parameters

An old MBMS system for *in situ* measurements of the concentration of gas phase was built by Soonam Park et al. [11] in the HTPL at the Univerisity of Minnesota in 2003. This system was designed for the detection of neutral radicals and molecules and was not able to measure ionic species. Hence, in addition to updating the system, redesigning and modifying the old MBMS was imperative to make it more broadly suitable to both measuring neutral and ionic species. Meanwhile, a newly purchased mass spectrometer (MS) with ion optics enabling automated data acquisition and plasma ion sampling was also employed. The schematic diagram of the new MBMS system is shown in figure 1.3.

The reduction by 9 orders of magnitude in pressure, is achieved through 3 different pressure stages separated by aligned skimmers and pumped down by three turbomolecular pumps. A detailed schematic of the pumps used, including the pumping speeds for N_2 is shown in figure 1.3.

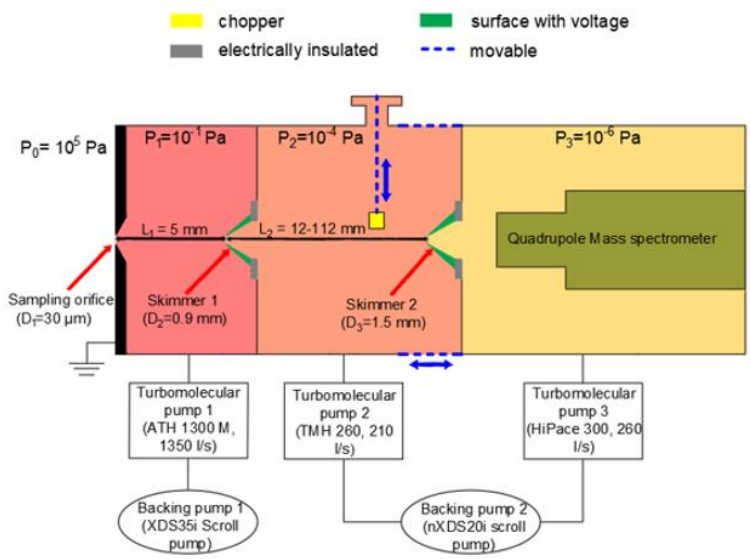

Figure 1.3: Schematic diagram of the MBMS system

The third vacuum stage is the hosting environment for the SIM900N quadrupole mass spectrometer (QMS) from Hiden Analytical Ltd. The reason for choosing a QMS is due to its lower cost, light weight, compact design, simple operation and high scan speed. The number density of neutral species in the molecular beam signal will drop roughly as the square of the beam path length [15]. Hence the decrease of the beam path length can contribute to a larger MS signal for neutral species. A resonant chopper with a fixed frequency of 200 Hz is installed on the second chamber through a magnetic feedthrough. It can be positioned between the two conical skimmers to chop the molecular beam signal. This requires an increase in the distance between the skimmers. To this end, we installed a

translational stage to still be able to sample with a minimum distance when the chopper is not used. This is a requirement for ion measurements (see further).

Table 1.1: Design parameters of MBMS

Parameter	Value	Parameter	Value
D_1	30 µm	L_1	5 mm
D_2	0.9 mm	L_2	12-112 mm
D_3	1.5 mm		

The diameter of the sampling orifice is chosen to be 30 µm, we use both stainless steel and Macor sampling orifice plates. The use of dielectric substrate is to measure the species in the active plasma zone to avoid the plasma transition from a diffusive mode to a constrict channel when using a metal sampling plate at small plasma-substrate distances. Two skimmers made of nickel are used to separate the 3 pressure stages with a diameter of 0.9 mm and 1.5 mm respectively. The skimmer and orifice design parameters are summarized in table 1.1. The typical operating pressures and mean free paths and collision frequency of molecules in each stage are presented in table 1.2.

Table 1.2: Typical working parameters of MBMS

Parameter	Ambient	Stage 1	Stage 2	Stage 3
Pressure, P (Torr)	760	1.8×10^{-3}	3.0×10^{-5}	8.0×10^{-7}
Mean free path of molecules, λ (m)	6.8×10^{-8}	2.8×10^{-2}	1.73	6.5×10^{1}
Collision frequency, Θ (s^{-1})	6.34×10^{9}	1.5×10^{4}	2.5×10^{2}	6.68

The diameter of the sampling orifice is chosen to be smaller than the typical sheath thickness at atmospheric pressure, to avoid penetration of the plasma into the first low-pressure stage [16]. The testing results of the system show that the pressure of the first

stage will be in the range of 1.0-3.0 mTorr when the turbomolecular pump is running at full speed, so the estimated quitting surface is predicted to be 0.2 mm from the sampling orifice. The tip of the first skimmer is placed 5 mm away from the sampling orifice, which is well inside the free molecular flow region according to the "quitting surface model".

1.2.3. Measurement of neutral atoms and molecules

Neutral species need to be ionized before entering the mass spectrometer. The system manipulates the ion trajectories through electrical and magnetic fields, and then sorts the ions based on their mass-to-charge ratio (m/z). A typical QMS consists of four components: ion source, energy analyzer, mass analyzer and detector, as presented in figure 1.4. In the case when the QMS is also able to sample ions directly from the plasma, it has ion optics before the ionizer to guide the sampled plasma-produced ions into the MS.

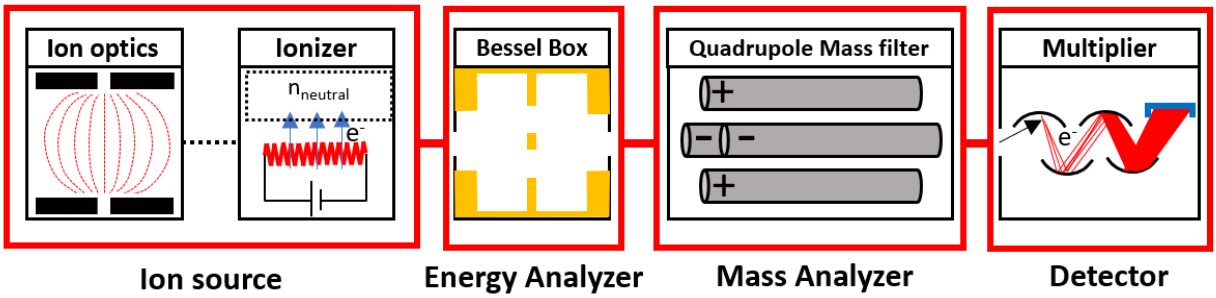

Figure 1.4: Conceptual illustration of the QMS

For measuring the neutral/radical species, residual gas analyzers (RGA) mode of the MS is used. The neutral species from the molecular beam first need to be ionized inside the ionizer by bombarding with the electrons. Then the created ions will enter the energy analyzer, a Bessel-box type energy filter in the QMS, which blocks the central part of the beam that is not deflected by the imposed electric field, helping to eliminate the plasma-produced photons and electrons reaching the detector. It can also be used as an ion energy filter. A quadrupole mass filter is made up of four parallel metal rods, which has the ability

of separating ions based on their mass-to-charge because each ion species has its own specific transmission RF voltage with a DC offset voltage. The last part of the QMS (the detector) is an ion-counting Secondary Electron Multiplier (SEM) composed of discrete dynodes, which are several cylindrically shaped metal sheets with low electron-work-function coatings. Ions strike on these sheets multiple times and create many secondary electrons, resulting in a higher detection sensitivity of the MS. The steps described above are the complete transition process inside the QMS for neutral species.

For neutral species, the detected signals do not all come from the sampling beam. It is composed of the beam signal and background signal that comes from the molecules present in the chamber or the remaining particles reflected from surfaces such as inside the ionizer system. A typical approach to separate the background from the molecular beam signal is to measure the signal of the beam and subtract the background obtained by a measurement when the beam is blocked. In the MBMS system, we implemented a tuning fork resonant chopper with the fixed frequency of 200 Hz in the second vacuum stage via a magnetic coupling feedthrough, to periodically block the molecule beam. The real signal from the sampling orifice can be obtained by subtracting the background signal from the total signal. When the system is running at the neutral measurement mode, the chopper is positioned inside the second vacuum stage to block the beam, as shown in figure 1.5(a). At this configuration, the distance (L_2) between the two skimmers is 68 mm, so the total molecular beam path from the sampling orifice to the inlet of the MS is 89 mm.

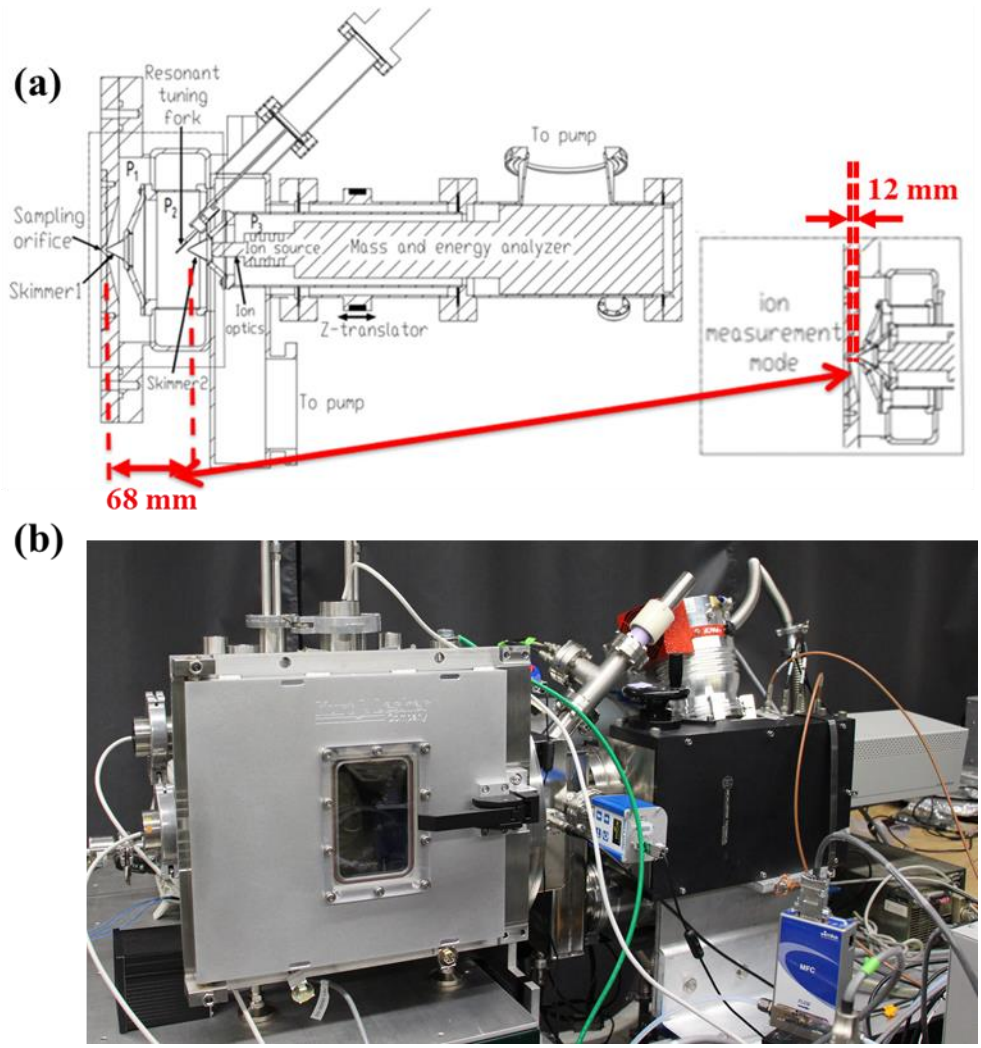

Figure 1.5: (a) Sectional view of the designed MBMS system; (b) picture of the established MBMS system.

Spatially resolved measurements can be performed with motorized x-y-z translation stages (25 mm travel range) in front of the sampling plate, as long as the settings of the MS are fixed. The minimum step size of the translational stage is 6 µm. Time-resolved measurements can be performed with a multichannel scalar detector (MCS). The temporal and spatial resolution of measurements can be as low as 1 µs and ~100 µm (about three times the orifice diameter), respectively. The picture of the established MBMS system is shown in figure 1.5(b). More details of MBMS system together with testing results will be covered in the Chapter 2.

1.3 Plasma catalysis

The highly reactive properties of LTP are beneficial for many applications, however the non-equilibrium nature and limited tuning parameters make LTP difficult to control. As many applications involve the interaction of LTP with materials, for the further advancement of application, a more detailed understanding of the underlying mechanisms of plasma-material interactions would be highly beneficial. Specifically, the mechanisms of the interaction between LTP and catalysts will be reviewed in this section.

Plasma catalysis refers to the combination of a gaseous discharge heterogeneously with a material that has catalytic properties, which gained increasing attention for the observed synergistic effects between plasma and catalysts for the conversion of chemicals. Whitehead [17] shows an example of plasma catalysis synergy for toluene removal in air at room temperature. It shows that the destruction rate in plasma catalysis is more than 3 times higher than the combination of plasma and thermal catalysis alone. Besides, researchers also have found that plasma catalysis showed an improved performance compared with the plasma-only or catalysis-only conditions in the conversion of methane [18]–[20] and greenhouse gases [21], reduction of nitrogen oxides [22], and nitrogen fixation [23]. However, the underlying mechanisms responsible for these highly beneficial synergistic effects are not clear. Possible reasons can be found in the many plasma constituents and plasma-induced effects, such as localized surface heating, surface charging (electrons and ions) effects, the presence of high electric fields, reactive/excited species fluxes, photon fluxes, morphology changes induced by plasma (e.g. etching), etc. It is known that the performance of catalytic processes depends on the relative binding energies (enthalpies of adsorption) of reagents, intermediates and products to the surface.

If the reagents are bound weakly, the coverage of the surface will be low and lead to a low surface reaction rate. In contrast, as the bonding to the surface becomes too strong, the surface coverage will be greater, and the reagents and products will be too stable to decompose or react. There exists an optimum described by the Sabatier principle showing that the catalytic activities have a volcano shape variation as a function of the strength of adsorption [24].

In this dissertation, I will focus on the CH_4 conversion in the presence of O_2 as an example system to study plasma-catalyst interaction. The conversion of CH_4 into valuable chemicals includes indirect and direct routes. The industry currently implements the indirect routes in which CH_4 is first converted into syngas (mixture of H_2 and CO) and then the syngas is further converted into different valuable products using the well-established methanol production technology or Fischer-Tropsch synthesis [25]. The use of nonthermal plasma offers an easier method to break the strong C-H bonding compared with the thermal catalysis in the methane conversion. For example, the plasma catalysis in steam methane reforming (SMR, $CH_4 + H_2O$) has been extensively investigated by Nozaki et al. [26]. The authors developed a DBD reactor containing catalyst for the SMR processes, where CH_4 was partially reformed by using the mixture of CH_4, N_2 and H_2O vapor. It was observed that CH_4 conversion in the hybrid reactor was much greater than the combination of DBD and thermal catalyst reactors, showing a synergistic effect in plasma catalysis. The authors explained the surface reactions using the Langmuir-Hinshelwood mechanism, specifically, the plasma could excite the CH_4 and H_2O molecules by electron-impacted reactions before they were chemisorbed on the active site of the catalysts. Both the dehydrogenation of CH_4 and water chemisorption were believed to be important because chemisorbed carbon could

block the active site without sufficient oxygen-related intermediates such as O and OH. Additionally, the experimental results of SMR using the DBD reactor without any catalysts indicated that the gas-phase CH_4 oxidation by plasma-produced oxidizers (O and OH) was limited to promote the SMR process.

As an alternative to the highly endothermic SMR process, dry reforming of methane (shorted as DRM, $CH_4 + CO_2$) with plasma catalysis attracts researchers' interests due to its ability to capture CO_2 from industrial and natural sources. Tu and Whitehead [18] developed three different packing methods for the single-stage plasma-catalysis system in the context of dry reforming of methane into syngas. The results showed that the partially packed catalyst resulted in a strong filamentary discharge which could significantly enhance the interaction between plasma and catalysts. The synergistic effect was observed when using 10% wt% Ni/γ-Al_2O_3 catalyst in flake form calcined at 300 ^{o} C. Snoeckx et al. [27] computationally investigated the influence of the operating parameters of a DBD source on the conversion and energy efficiency of dry reforming of methane. It was found that increasing the CO_2 concentration in the feed gas can increase the conversion rate and energy efficiency. Also, a higher number of filaments could lead to a higher conversion rate and energy efficiency. The best results were found to be 84% and 8.5% in conversion and energy efficiency, respectively. In addition, a review by Khoja et al. [28] extensively summarized the overall status and developments of DRM using catalytic DBD plasma. Researchers were devoted to improving the energy efficiency and conversion of DRM rate by changing materials in catalyst or supports, redesigning reactor configuration of DBD reactors or tuning plasma operating parameters. Nevertheless, a better understanding in

macroscopic and microscopic kinetics and fluid models for plasma catalysis is still needed to further improve the overall performance of DRM processes.

Similarly, another conversion method of CH_4, partial oxidation of methane (CH_4 + O_2) to syngas, has also been studied in the field of plasma catalysis. Partial oxidation occurs when the amount of oxygen is not sufficient for the complete oxidation of CH_4, resulting in the products of hydrogen and carbon monoxide. The ratio of products (H_2/CO) is 2:1, which is suitable for the subsequent synthesis into methanol or other chemicals. Pietruszka et al. [29] investigated the effects of different operating parameters on the product distribution of partial oxidation of methane in a DBD reactor with catalysts. It was found that the presence of Ni/Al_2O_3 in the discharge region could lead to the oxidation of CO to CO_2 at 300 ºC and above. Plasma-produced reactive species were supposed to be responsible for the change in surface chemistry. Song et al. [30] studied the hydrogen production from partial oxidation of methane using a DBD reactor with NiO/γ-Al_2O_3 catalysts. The experimental results showed that the CH_4 conversion and H_2 yield using the DBD reactor with catalysts inside increased from 60.1% and 21.3% to 83.6% and 28.4% respectively, compared with the one without catalysts. Also, the catalyst activity was improved at low catalyst temperature and the formation of by-products was reduced. It was commented that the plasma excited the reactants and therefore the absorption energy of CH_4 and O_2 on the catalyst surface was reduced; on the other hand, the plasma also promoted the desorption of products from the catalyst surface. Shareei et al. [31] investigated the partial oxidation of methane at room temperature using a DBD reactor with NiO-CaO/Al_2O_3 as catalysts. The results showed that a 100% CH_4 conversion was achieved by optimizing the Ar flow rate and applied voltage.

Except for the partial oxidation of methane into syngas, the direct conversion of CH_4 into liquid oxygenates by plasma catalysts also attracts researchers' attention in recently years. The remote location of natural gas resources and the difficulties in transporting methane requires such a technology to covert CH_4 into liquid chemicals before transportation. Loenders et al. [32] conducted microkinetic modelling to assess the potential of the partial oxidation of CH_4 into oxygenates. The results showed that vibrational excitation enhanced the turnover frequency of the catalytic dissociation of CH_4, which could potentially improve the selectivity in CH_3OH, HCOOH and C_2 hydrocarbons. The authors also examined the role of various radicals produced by the plasma in the surface chemistry and this resulted in suggestions on how plasma composition should be tuned to improve the yield of the desired products. Li et al. [33] performed selective oxidation of methane to methanol in CH_4/O_2 plasma using Ni-based catalysts at low temperature and atmospheric pressure. 50% and 81% selectivity in CH_3OH and liquid oxygenates were achieved respectively. A chemical kinetic modelling was also performed to show the dominant production pathway of CH_3OH. Chawdhury et al. [34] investigated the partial oxidation of CH_4 into liquid fuels and chemicals over three γ-Al_2O_3 supported metal catalysts (N_i, Cu and Fe) in a co-axial DBD reactor at room temperature and atmospheric pressure. The combination of DBD with catalysts improved the selectivity of oxygenates up to 71.5% compared to the case without catalysts (58.3%). Among the three catalysts, Fe/ γ-Al_2O_3 showed the highest selectivity in CH_3OH (36%) and a significant yield of 4.7%. The authors also proposed the surface reaction pathways for producing CH_3OH, and they indicated that surface CH_x were critical for the methanol production. The

origin of the surface CH_x was either from the gas-phase or through the dissociation of absorbed CH_4.

The above studies all observed synergistic effects between plasma and catalyst in their experiments, nonetheless, few of the studies provide specific explanations of the synergistic effect while many different hypotheses are reported. Publications which focus on the mechanism of plasma-catalyst interaction are very rare. Zhang et al. [35] investigated the plasma-catalyst interactions using an APPJ and catalyst powder by time-resolved diffuse reflectance infrared Fourier transform spectroscopy (DRIFTS) in the context of partial oxidation of methane. The authors explained the mechanism of the reduction in downstream gas phase CO at 500 ºC observed in a previous study [36]. The DRIFTS C-O signal at the catalyst surface increased with an increase in catalyst temperature as well as a decrease in plasma-catalyst distance. Additional addition of oxygen in the APPJ feed gas caused the oxidation of C-O at the catalyst surface, resulting in an increase in gas-phase CO_2. This finding suggests that the CO production could be tuned by the amount of O_2 addition from the APPJ.

In the context of ammonia synthesis, there were several publications in recently years which provided new insights in the plasma-catalyst interaction. Through numerical modelling, Mehta et al. [37] pointed out that vibrationally excited species created by plasma could enhance the adsorption onto catalyst surfaces and increase the reactivity, and that the plasma enhancement would be beneficial for metals that bind reagents too weakly in thermal catalysis. While the result is very interesting and might be one of plasma actions responsible for synergy, it is not supported by experiments and many other species and effects might contribute to the observed synergistic effects which were not considered in

the model. The complex composition of plasma is the motivation to perform detailed experiments to assess the importance of different reactive species. As reported in [24], much more efforts are needed to investigate timescales involved in the production and removal of species in the gas and surface phase and how these species are distributed on the catalytic surface and within the plasma volume.

Barboun et al. [38] performed ammonia synthesis in a DBD plasma-assisted catalytic reactor. The results of varying the gas composition indicated that the overall reaction and gas-phase reaction are in first order with both N_2 and H_2 composition. However, the rate contribution from the plasma-catalyst interaction are in first order with N_2 but in zeroth order in H_2. This result indicated that the activation of N_2 by the plasma is the most critical step in driving the plasma-assisted catalytic reaction.

Winter et al. [39] investigated the contribution of different reaction mechanisms to the NH_3 production at the catalyst surface. It was found that the ammonia yield could be impacted by plasma-derived intermediates (NH_x, x=1,2,3) and their interactions with the catalyst surface. In addition, the surface temperature and plasma irradiation both promoted NH_3 desorption from the catalyst surface, resulting in an enhancement of gas-phase NH_3 production. The two-stage plasma catalysis experiments confirmed the significance of plasma irradiation. There were two reactors (batch reactor and flow reactor) used in this study. The experiments of the batch reactor were conducted at 12.5 Torr instead of the atmospheric pressure for the flow reactor. As explained by the authors, this low-pressure condition of the batch reactor was required to obtain a good signal-to-noise ratio for the FTIR measurements. The authors correlated the trends obtained in the batch reactor to those measured in the flow reactor to bridge the pressure gap. Nevertheless, the plasma

properties and diffusion lengths of species at 12.5 Torr and atmospheric pressure (760 Torr) are very different. It is expected that ions impinging on the catalyst surface at 12.5 Torr have larger energies than those at atmospheric pressure. Also, plasma-produced short-lived species including NH_x can sustain higher concentrations at the catalyst surface for the low-pressure environment. These two possibilities induced by the pressure gap might change the mechanism responsible for synergy in plasma catalysis.

Furthermore, in order to determine absorbed NH_x intermediates (x=1,2,3) on the catalyst surface, Barboun et al. [40] conducted inelastic neutron scattering (INS) experiments with a sequential treatment of catalysts using N_2 and H_2. The experimental results indicated that NH_x species could be formed through surface reactions (thermal hydrogenation) between the absorbed nitrogen introduced by the plasma and the plasma activated or thermal H_2. As explained, the role of plasma was to activate nitrogen via vibrational excitation, electronical excitation or dissociation, resulting in an enhancement in the adsorption of N on the catalyst surface which normally requires the elevated temperature and pressure. Following the nitrogen adsorption, hydrogen produced by the plasma or thermally can hydrogenate the surface-bounded N species. This study provides a solid evidence and better understanding of the surface reaction in the complicated plasma-catalyst interaction.

In short, although all these studies provided many insights in the mechanism of plasma-catalyst surface interaction, further studies quantifying plasma-produced reactive species onto the catalyst surface at atmospheric pressure are still needed particularly for the CH_4-O_2 system and are part of this dissertation.

1.4 Motivation and objectives

One of the goals of this dissertation is to further explore the mechanism underpinning plasma-catalyst interaction specifically for the partial oxidation of methane. The scientific understanding of plasma surface interaction requires the *in situ* measurements of the species fluxes incident on and out of the substrate and the characterization of surface activities [41]. *Ex situ* measurements cannot capture the species involved in the reactions because the short-lived species will keep reacting and disappear. Also, the surface properties might change due to subsequent reactions during the *ex situ* analysis. The *in situ* measurement of the plasma-generated reactive species fluxes ought to be correlated with the *in situ* measurements of changes in surface properties.

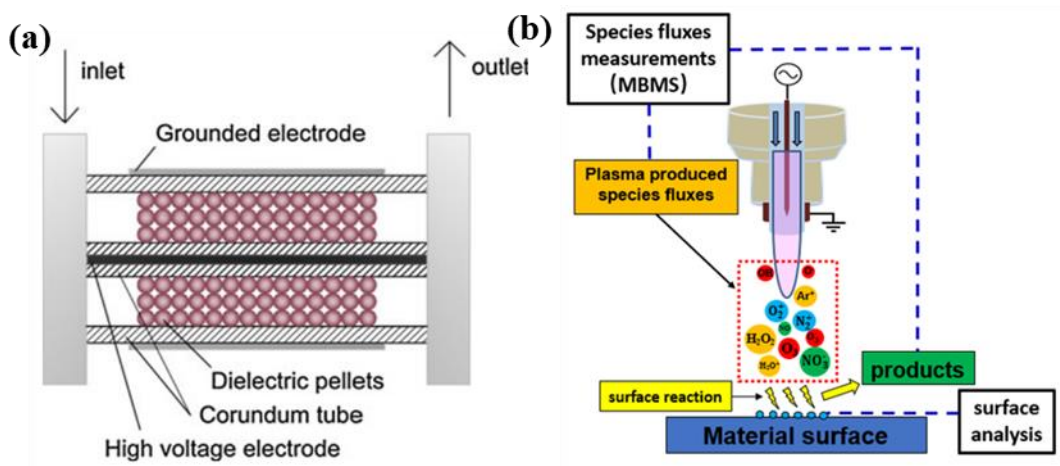

Figure 1.6: (a) Schematic diagram of the dielectric packed-bed plasma reactor (reprinted with permission from ref [42] © 2011 Springer Nature); (b) experimental strategy illustration for plasma-material interaction.

The common method of combining catalysis with plasma is to use DBD packed-bed reactors allowing for excellent contact between plasma and catalysts [18],[20],[43],[44]. Schematic diagram of the dielectric packed-bed plasma reactor adapted from [42] is illustrated in figure 1.6(a). The main drawback of the configuration of such a plasma source

is the inconvenience for the optical diagnostic methods and the large inhomogeneity of the plasma. The gas temperature of the packed-bed reactor is also not homogeneous making it not suitable for evaluating potential local heating effects on the catalyst performance caused by the plasma. These limitations of the packed bed reactor make it difficult, if not impossible, to investigate the cause of the synergistic effect. Hence, it is necessary to find a well-characterized plasma source instead of the DBD packed-bed reactor to perform the research. As discussed before, APPJs can be an alternative as it allows to decouple the plasma and catalyst as APPJs can operate remotely with convective transport of reactive specials to the catalytic surface. In addition, a lot of efforts have been devoted to the characterization of the APPJ source [45]–[47] providing a solid background to start the research. On the other hand, the APPJ impinging on a catalyst surface also allows for performing the *in situ* characterization of the catalyst surface which might be more difficult in DBD packed-bed reactors. Due to the presence of many short-lived species in the plasma, the catalyst surface properties might change quickly after exposing to the ambient air, hence it is necessary to perform *in situ* characterization of the catalyst surface. This work is collaboration with Prof. Oehrlein's group at the University of Maryland who performed detailed surface analysis for the same plasma conditions. Several *in situ* surface characterization methods such as DRIFTS and ATR-FTIR are applied for the same plasma conditions as used for MBMS measurements, allowing a correlation of the plasma-produced species fluxes with their surface analysis results. This will allow us to assess which species are responsible for the observed surface modifications and lead to a further understanding of the fundamental mechanisms of the synergistic effects. A schematic of the approach is shown in figure 1.7(b).

The objectives of this thesis can be summarized as the follows:

1. To establish an advanced MBMS system, enabling the detection of both ionic and neutral species, and to extend the diagnostic ability of MBMS.

2. To understand the influences of operating parameters of RF-driven APPJ on species density/flux as well as the plasma dynamics.

3. To establish the link between the variations of species fluxes to the *in situ* changes of the catalyst surface conditions measured at the University of Maryland to identify key species responsible for changes in catalyst surface and chemical conversion in CH_4 and O_2 gas streams.

1.5 Scope of this dissertation

The main content of this dissertation consists of three parts. The first part (chapter 2-5) focuses on the development of the MBMS system. The diagnostic ability of MBMS is tested and further extended. The second part (chapter 6-7) relates to the understanding of the plasma sources by MBMS. The control of plasma produced species fluxes as well as ion dynamics are investigated. The third part (chapter 8) is related to the application of plasma-catalysis. The MBMS results help to identify the species responsible for plasma-surface interaction in the context of partial oxidation of methane. Details of each chapter are as follows.

In Chapter 2, the MBMS system is described in detail and its capability is shown by the measurement of the absolute densities of O and O_3 as a function of nozzle-substrate distance in the afterglow of the plasma jet operating in open air were measured. Pseudo-1D plug flow modelling was also implemented and the modelling results agree with the

experimentally observed trends of O and O_3 densities. The influence of the gas flow fields in free and substrate-impinging APPJs on the distribution of O density was also investigated.

In Chapter 3, the measurement and calibration method of singlet delta oxygen ($O_2(a^1\Delta_g)$), the first electronically excited state of O_2 by MBMS and one of the dominant reactive species in O_2 containing plasmas are presented. The threshold ionization method is used to differentiate the ground state oxygen and singlet delta oxygen. The ability to measure axial and radial profiles of $O_2(a^1\Delta_g)$ impinging on a substrate in the effluent of the APPJ is a key advantage of the MBMS diagnostic method over previously reported optical methods.

In Chapter 4, the calibration method of absolute ion density was developed with a corona discharge as the reference ion source. Positive ion densities in the afterglow region of an Ar+1% O_2 APPJ were found to be about 3-4 orders of magnitudes lower than the densities of the dominant reactive neutral species (O, $O_2(a^1\Delta_g)$, O_3) at a distance larger than 2 mm from the visible plasma plume. The results illustrate the ability of molecular beam mass spectrometry to enable a quantitative evaluation of both neutral and ionic species in many applications using APPJs.

In Chapter 5, quantitative measurement method of vibrationally excited N_2 was developed by MBMS. The mass spectrometry signals were fitted with the electron-impact ionization cross sections as a function of electron energy to indicate a vibrational temperature. This method further extends the capability of MBMS to quantitatively measure vibrationally excited species of N_2 near interfaces which might have future importance for studying ammonia synthesis through the plasma-catalysis route.

In Chapter 6, different plasma operating parameters were investigated to alter the dominant species densities in an Ar-O_2 plasma jet. The impact of the surface-dependent loss probability and boundary layer reactions on the species flux to a substrate is also reported. The results will contribute to a more detailed understanding of the roles of reactive species in plasma catalysis or plasma-surface interactions in general.

In Chapter 7, the influence of the RF modulation frequency upon the ion fluxes was investigated by time-resolved measurements using MBMS. The lifetimes of different ions were obtained, and the quantitative measurements of ion densities enabled a better understanding of the memory effects between modulation cycles. This is particularly important also for MBMS studies as our measurement approach involves the modulation of the RF plasma for background subtracting.

In Chapter 8, the synergistic effects of partial oxidation of methane into syngas in plasma catalysis was studied. We directly link the impact of plasma on operando catalyst surface species and chemical conversion yields with measured species fluxes by MBMS to assess key plasma-produced species impacting methane conversion processes in the presence of O_2, leading to a further understanding of the fundamental mechanisms in plasma-catalyst interaction.

In Chapter 9, a detailed study of plasma-produced species and conversion in the context of direct conversion of methane to oxygenates at room temperature was performed. The products and plasma-produced species with or without catalysts were both quantified using MBMS, and the synergistic effects were observed in methanol production. This study investigated the roles of secondary more long-lived radicals played in surface reactions due to the reason that they might be less impacted by transport limitations.

The summary and conclusions, as well as the perspectives on future work are presented in Chapter 10.

Chapter 2

Absolute spatially and time-resolved O, O_3 and air densities in the effluent of a modulated RF driven atmospheric pressure plasma jet obtained by molecular beam mass spectrometry[1]

[1] This chapter is adopted from the previous publication J. Jiang, Y. Luo, A. Moldgy, Y. Aranda Gonzalvo, and P. J. Bruggeman. "Absolute spatially and time-resolved O, O_3, and air densities in the effluent of a modulated RF-driven atmospheric pressure plasma jet obtained by molecular beam mass spectrometry." Plasma Processes and Polymers 17, no. 6 (2020): 1900163.

2.1 Introduction

Cold atmospheric pressure plasmas jets (CAPPJs) produce a chemical-rich gaseous environment containing reactive species including ions and excited states of atoms and molecules. This is enabled by energetic electrons with energies above 1 eV while the gas temperature is maintained close to room temperature. The high reactivity at low gas temperatures is beneficial for a variety of heat-sensitive medical applications including wound healing [48], treatment of dental diseases [49], and cancer treatment [50]. These plasma-medical applications require the plasma source to be safe for treating patients. Significant effort has been dedicated to minimizing current (to avoid electric shocks), heat flux (to keep target temperature below 40°C) and limit UV fluence [51], although less work has been devoted to assessing the flux of the large amount of possible different reactive species to a target surface.

Low-temperature atmospheric pressure plasma can also be applied for the conversion of chemicals particularly when exploring promising plasma-catalysis synergy effects [17]. Indeed, a combination of plasma with catalysis has been found to lead to a higher conversion efficiency than the cumulative effect of catalysis and plasma conversion separately. The underlying mechanisms responsible for these highly beneficial synergistic effects are, to date, not understood and are typically suggested to be due to the enhancement of a catalytic activity by plasma-produced reactive species [24]. As is the case with biomedical applications, detailed measurements of species fluxes to catalytic surfaces are currently lacking.

The further advancement of medical applications and plasma catalysis requires us to establish a link between the plasma operating conditions and the produced gas-phase

species fluxes that reach the biological samples or catalytic surfaces and enable the beneficial action of the plasma. This requires the quantitative characterization of the plasma-produced reactive species fluxes which can be achieved by molecular beam mass spectrometry (MBMS). MBMS is very suitable to measure reactive species impinging on a target surface because the plasma jet can be placed perpendicular to the sampling plate of MBMS allowing for scanning of the spatial profile of the species fluxes. Laser diagnostic methods such as laser-induced fluorescence (LIF) or two-photon absorption LIF (TaLIF) are similarly powerful in the detection of reactive species. However, the measurement of absolute species densities can be very challenging by LIF or TaLIF at the substrate surface due to the vignetting and scattering of the laser beam near the substrate. In addition, TaLIF of O with nanosecond pulsed lasers for conditions with strongly varying gas composition is challenging as it is impossible to correct for variations in quenching of the excited state due to its sub-nanosecond lifetime without additional independent measurement.

Previous research work has shown that reactive oxygen and nitrogen species generated by the CAPPJs are the main factor which is enabling the biological impact of plasma [52]. Recent work in our lab found that OH and ClO^- generation in solution correlates with bacterial inactivation [53]. The formation of ClO^- in the liquid phase was attributed to the reaction of plasma-produced O with Cl^- in the saline solution. Two-photon absorption laser-induced fluorescence (TaLIF) measurements of O on similar CAPPJs showed that the O density as a function of axial distance drops very fast [54],[55]. This decrease in O seems to be on a similar length scale as the distance-dependent effects observed in the bacterial inactivation study. The assessment of reactive species involved in bacterial inactivation was performed in the liquid phase by scavenger measurements [53]. This indirect method

was capable of finding correlations between the presence of reactive species with bacterial inactivation but does not provide a quantitative analysis of the related species concentration or fluxes which induce the reactivity.

Ozone (O_3) has a strong oxidizing property and can be widely used in many medical fields [56]–[58]. A large amount of research has been devoted to the quantitative measurement of O_3 production using optical diagnostic techniques for different plasma sources [59]–[63]. Nonetheless, as O_3 is measured by absorption, the recirculating flow in the presence of a jet impinging on a target significantly complicates spatially resolved density measurements for CAPPJs. Zhang et al. [47] reported spatially resolved ozone densities in the same time-modulated RF driven atmospheric pressure plasma jet as used in this study. The production and destruction of O_3 were investigated through experimental measurements and the results from a pseudo-1D plug flow model. This showed that the depletion of O_3 in the core of the plasma was due to the large atomic oxygen density. The good quantitative agreement between the experimental and modelling results for the ozone density validated the pseudo-1D plug flow model approach for plasma jets and offered insights in the densities of a large number of additional species. This approach was shown to be very suitable for studying non-thermal plasma jets with complex reaction sets in open air for biological applications. The experiments performed by Zhang et al. [47], like the majority of the reported work, were for free jets without substrate. However, most of the biological applications have the jet impinging on a substrate such as a liquid or a biological sample. The gas flow structures of free jets and substrate-impinging jets are very different [64], and one cannot directly extrapolate the species densities measured in free jets to assess species fluxes incident on the substrates.

Both O and O_3 are also important in the context of plasma catalysis applied for, for example, the partial oxidation of methane. The production of O and O_3 fluxes incident on catalysts could possibly be responsible for the observed synergistic effects between plasma and catalysis [24]. Detailed knowledge of absolute densities of O and O_3 at the catalytic substrate is thus very valuable for studying the underlying mechanisms of plasma catalysis. The goal of this work is to measure the concentrations of O, O_3 and the air in the effluent of a time-modulated RF driven plasma jet in open air at the position of the substrate using MBMS. Time-resolved measurements of atomic oxygen, molecular oxygen and ozone during the modulated period are also shown to illustrate the effect of flow disturbance by the plasma on the production of ozone. A pseudo-1D plug flow model as in literature [47] will be used to assess the trends of O and O_3 densities as a function of distance for substrate-impinging plasma jets. A major effort of the paper is on the accurate calibration of the MBMS particularly taking into account the effect of the change in gas composition in the jet on the MBMS measurement. The measured O flux is also linked with ClO^- formation in a saline solution to quantitatively show that the proposed mechanism, $O+Cl^- \rightarrow ClO^-$, is consistent with the estimated plasma-produced O flux to the liquid.

2.2 Experimental setup and measurement methods

2.2.1 Plasma source

The plasma jet used in this work consisted of a tungsten needle electrode (d= 1 mm) with a sharp tip inside a cylindrical quartz tube. The inner diameter of the quartz tube was 1.8 mm and the outer diameter was 3 mm. A copper ring acting as the ground electrode was positioned outside the quartz tube at a distance of 1 mm from the nozzle. The electrodes were held in a plastic enclosure of diameter 25.4 mm. The plasma jet was driven by

applying a radio frequency sinusoidal wave at a frequency of 12.6 MHz and duty cycle modulation of 50% at 50 Hz such that the plasma ON and plasma OFF times were 10 ms each. The RF high voltage waveform was generated by a function generator (Tektronix AFG2021) and amplified by an RF power amplifier (Amplifier Research 750A250A). The amplifier was matched to the plasma jet by a homemade matching box consisting of an inductor. A more detailed description of the plasma source can be found in the previous work [65]. The average dissipated power in the plasma was 7.6 ±0.15 W and the plasma-on power was 15.2 ±0.3 W. This power was obtained by multiplying the measured current and voltage waveforms as described in detail elsewhere [66]. For all the measurements in this work, Ar+1% O_2 was fed through the quartz tube at a total flow rate of 1.5 standard liter per minute (slm) controlled by two mass flow controllers (MKS GE50A). The temperature and relative humidity of the ambient air in the laboratory during the experiments were about 21.5 °C and 47% respectively.

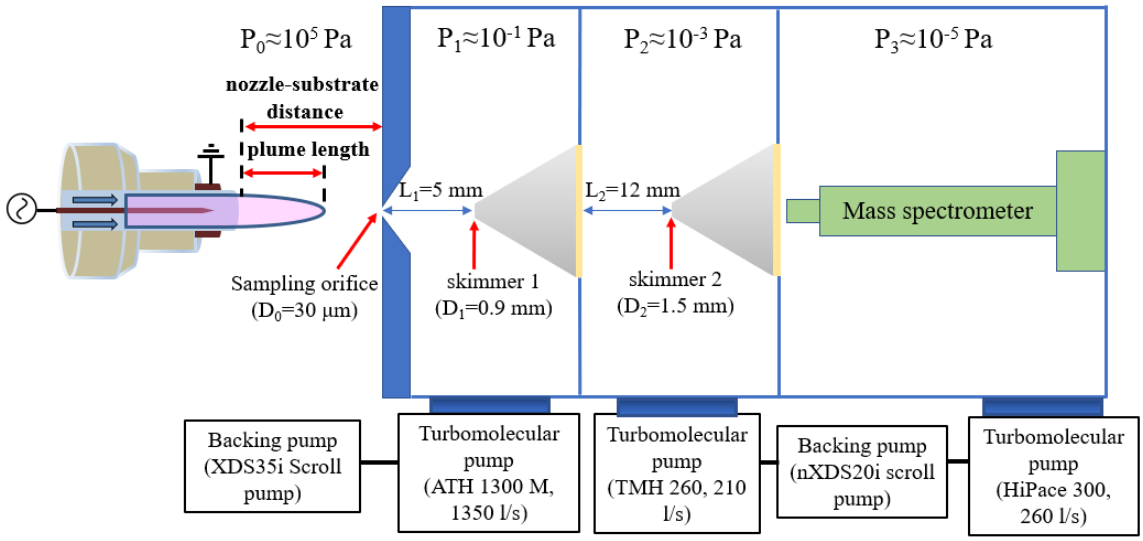

Figure 2.1: Schematic of the MBMS system.

2.2.2 Molecular beam mass spectrometer (MBMS)

Figure 2.1 shows a schematic representation of the MBMS system used in this study. The reduction by 9 orders of magnitude in pressure from atmospheric pressure to the pressure of the chamber containing the quadrupole mass spectrometer SIM900N (Hiden Analytical Limited), was achieved through 3 different pressure stages separated by aligned skimmers and pumped down by three turbomolecular pumps. The turbomolecular pump of the first stage was an ATH 1300 M Maglev Hybrid turbomolecular pump (Alcatel Vacuum Technology) with a pumping speed of 1350 l/s, capable of dealing with the large inflow of gas from atmospheric pressure through the 30 μm orifice. The turbomolecular pumps for the second and third stages were a TMH 260 (Pfeiffer Vacuum) with the pumping speed of 210 l/s and a HiPace 300 (Pfeiffer Vacuum) with the pumping speed of 260 l/s, respectively. The pressures of the three vacuum stages were measured by the pressure gauges, a KJLC 275i Pirani gauge for the higher pressure stage and KJLC 354 Ion gauges for the other two stages. The inlet of the 2nd and 3rd stage was equipped with skimmers with a diameter of 0.9 mm and 1.5 mm respectively. During the measurements, the pressure in the first stage was 1.5 mTorr. This pressure is low enough to ensure that the supersonic gas flow entering the sampling orifice will go through a smooth transition into a molecular flow region [14], without the formation of a Mach disc. The tip of the first skimmer was placed 5 mm away from the sampling orifice, which is well inside the free molecular flow region according to the quitting surface model [11],[14].

The plasma jet was positioned horizontally in front of the sampling plate of the MBMS, as shown in Figure 2.1. The source was mounted onto motorized x-y-z translation stages (MTS25-Z8, Thorlabs) allowing for the positioning of the jet with respect to the sampling orifice with an accuracy of 6 μm. All the measurements presented in this work were

recorded along the axis of symmetry of the jet without having the plasma plume in direct contact with the sampling plate.

2.2.3 Species measurement

The operation of the mass spectrometer (MS) is based on manipulating the ion trajectories by electric fields to differentiate ions with different mass-to-charge ratios. For the measurements of neutral species, the neutral and radical species have to be ionized before entering the quadrupole of the MS. The measurement of dominant stable species like O_2, O_3 and N_2 is relatively easy and can be achieved by setting the ionizer with a standard *in situ* O_3 electron energy of 70 eV.

The detection of the short-lived reactive species or radicals such as atomic oxygen being a minority species in its parent gas O_2, can be more challenging. Electron impact ionization of radical species can result in the same ionic species as the dissociative ionization of their parent molecules which complicates radical detection by MS. However, the ionization potential of the radical is usually much lower than the energy required to produce the same ion from the parent molecule by dissociative electron impact. This can be used to our advantage to exclude the contribution in the MS signal from the parent molecule. For example, O^+ can be formed from the direct ionization of O radicals and the dissociative ionization of O_2 molecules [67]:

$$\mathrm{O} + \mathrm{e}^- \rightarrow \mathrm{O}^+ + 2\mathrm{e}^-, (\mathrm{E}_1 = 13.8\ \mathrm{eV}) \qquad \text{(R1)}$$

$$\mathrm{O}_2 + \mathrm{e}^- \rightarrow \mathrm{O}^+ + \mathrm{O} + 2\mathrm{e}^-, (\mathrm{E}_2 = 18.0\ \mathrm{eV}) \qquad \text{(R2)}$$

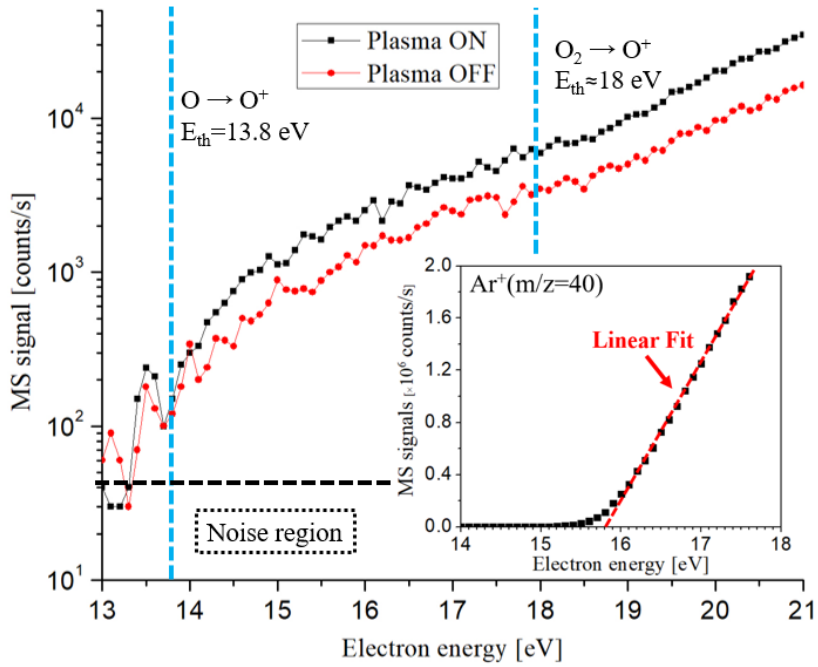

Figure 2.2: MS signal for O^+ (m/z=16) measured in the effluent of the jet (16 mm from the nozzle exit) as a function of the electron energy for the plasma-on and plasma-off cases. The black dashed line corresponds to the detection limit. Insert provides a threshold ionization mass spectrometry measurement of Ar.

E_1 and E_2 are the threshold energies required for the respective ionization processes. In Figure 2.2, the recorded MS signals for O^+ (m/z=16) are shown as a function of the electron energy, for both of the plasma-on and plasma-off cases. This approach is called threshold ionization mass spectrometry (TIMS). The absolute electron energy scale of the ionization source was calibrated by performing threshold ionization measurements of Ar and N_2 showing a shift of 0.4 eV in electron energy. All the electron energies reported in this paper were corrected for this shift. In addition, the threshold ionization energy measurement of Ar was consistent with an electron energy resolution of less than 0.2 eV of the ionizer.

For the plasma-off case, the MS should not detect any O^+ signal when the electron energy was below the threshold of dissociative ionization (18.0 eV) because the O radicals were only expected to exist in the plasma-on case. However, as the plasma jet was operated in

ambient air with a complex gas composition, other gases with a lower dissociative energy might contribute to this O^+ background. It is also possible that thermal dissociation of O_2 or other gases occurred on the hot filament in the ionizer leading to the formation of O radicals subsequently detected by the MS. Hence, the background signal (plasma off) needs to be subtracted from the total O^+ signal of the plasma-on case to differentiate between the O^+ coming from the plasma-produced O radical and the O^+ originating from other sources. The electron energy for measuring atomic O was set at 14.8 eV for all experiments reported in this paper.

2.2.3.1 Time-resolved MBMS measurements

In order to measure the species evolution during the modulation period of the plasma, or measure the molecular beam signal and background, time-resolved measurements were performed with a multichannel scaler (MCS) device. As it takes 1.3 ms for the gas molecules to cover the distance of 1.6 cm between the nozzle and the MBMS sampling orifice at a flow rate of 1.5 slm, the modulation frequency of the plasma was chosen to be 50 Hz. The obtained period of this modulation cycle is an order of magnitude large than the gas residence time of the plasma jet, and allowed for the convective removal of the plasma-produced species during each plasma modulation cycle. Hence, there are no short-lived and reactive species present in the jet during the plasma off period. This plasma modulation method, allows using the plasma off period as a background signal for the measurement of reactive species. This approach differs from the direct modulation of the molecular beam as used in references [15],[68]–[72] but has the potential advantage that it does not lead to a potentially significant change in species densities in the ionizer induced by modulation of the beam [73]. This approach is valid when the gas temperature variation is minimal so the plasma is not changing the gas density drastically as is the case for the

far effluent of the jet in this work. The MCS separately stored the signal counts of the MS in different bins according to their arrival times. The number of the bins (channels) used in the experiments was 200, corresponding to a time resolution of 0.1 ms. The MCS's internal 40 MHz clock is used to synchronize the trigger signal from the function generator with a jitter of maximum 25 ns, allowing for the accumulation of the signals during multiple measurement sweeps.

In this work, time-resolved measurements of different species (O, O_2 and O_3) with a time resolution of 0.1 ms were performed using a multichannel scaler triggered by the TTL signal from the function generator corresponding to the RF modulation cycle. The time-resolved measurements were accumulated over 3000 cycles.

2.2.3.2 Time-of-flight (TOF) of ions in MBMS

There is a time delay between the trigger signal corresponding with the plasma modulation and the moment when the plasma-produced species reach the detector due to the convection time of species and the transit time in the MBMS. The total transport time of species consists of three parts:

$$t_{total} = t_{atm} + t_{vac} + TOF \tag{2.1}$$

where t_{atm} is the convection time of species at atmospheric pressure from the plasma to the MBMS sampling orifice; t_{vac} is the time required for the species inside the molecular beam to travel from the sampling orifice to the entrance of the MS; and TOF is the time of flight of the ions through the MS. In order to analyze the time delay, it is particularly important to correct for differences between species for TOF as we can assume that t_{atm} and t_{vac} are in good approximation species independent. TOF is a function of ion mass, the initial kinetic energy of the ions, and the various electric potentials applied along the ion path in the mass spectrometer, which can be written as [74]:

$$TOF = d_{ext}\frac{\sqrt{2m}}{\sqrt{e(K_{ion}-V_{ext})+\sqrt{|eV_{endcap}|}}} + d_{en}\sqrt{\frac{m}{|2e(V_{endcap}-V_{cylinder}-K_{ion})|}} +$$

$$d_{mass}\sqrt{\frac{m}{|2eV_{te}|}} + d_{det}\sqrt{\frac{2m}{|eV_{dyn}|}} \quad (2.2)$$

where d_{ext}, d_{en}, d_{mass}, and d_{det} are the lengths of the extractor, energy filter, the mass filter and the detector respectively and $V_{ext,}$ and V_{dyn} are the potentials applied to the extraction section and the dynode. V_{te} is the transit energy, K_{ion} is the initial ion energy and m is the ion mass. The calculated averaged TOF for O^+, O_2^+, $O_3^+$are 49 μs, 70 μs and 85 μs, respectively.

2.3 MBMS calibration

2.3.1 Absolute calibration of O

The absolute densities of the species can be obtained with a reference gas of a known absolute density. This approach is straightforward for stable species (like O_2) as they can be directly supplied as a calibration gas from a gas bottle. However, for short-lived radicals like O produced by the plasma, this approach is not possible and another stable species ideally with the same molecular mass needs to be used. We used methane having the same molecular mass as O (m/z=16) for the absolute calibration of O and the absolute O density can be obtained using the following equation [75]:

$$n_o = n_{CH_4}\left(\frac{S_{O\to O^+}}{S_{CH_4\to CH_4^+}}\right)\left(\frac{\sigma^{CH_4\to CH_4^+}}{\sigma^{O\to O^+}}\right) \quad (2.3)$$

where $n_{CH_4}$is the CH_4 density and $S_{O\to O^+}$and $S_{CH_4\to CH_4^+}$ are the recorded MS signals from the measurement and calibration. The measured CH_4 calibration signal contains contributions of the molecular beam signal and the background gas in the ionizer. This background can be several times larger than the contribution of the beam [68]. $S_{CH_4\to CH_4^+}$

in Equation 2.3 refers to the beam contribution of the signal and not to the overall signal including the background contribution. The ratio of the beam and total signal for the ionizer in this work was determined to be around 0.25 by integrating a chopper in the MBMS system. This is enabled by having the pressure stage containing the mass spectrometer installed on a translation stage. The integration of the chopper led to a larger distance between sampling orifice and mass spectrometer and a significant reduction in radical signal, hence this approach was not used for radical measurement. The obtained beam-to-total signal ratio was multiplied with the total MS signals for stable species CH_4 to obtain $S_{CH_4 \rightarrow CH_4^+}$. Using the theoretical estimation of this ratio provided in the paper [68] yields a very similar value of 0.26 if we assume the molecular beam covers most of the area of the center hole of the ionizer. The cross sections for the direct ionization of O and CH_4 used in the calculation were 4.1×10^{-18} and 6.0×10^{-18} cm^2 respectively corresponding to an electron energy of 14.8 eV [76],[77].

The calibration measurements need to be performed for the same gas mixtures in order to keep the sampling distortion due to the supersonic expansion in the first stage the same. Gas temperature variations induced by the plasma can affect the gas density at the sampling orifice of the MBMS and impact the MS signal. To minimize this effect, we do not present any data for d < 12 mm to ensure that the gas temperature variation is less than 100 K corresponding to gas density variations of less than 30%. This is particularly required as the calibration data is obtained at room temperature. The gas mixture was prepared by mixing argon (1.5 slm) with different amounts of CH_4. The plasma jet is placed at a distance of approximately 0.85 mm between the MBMS sampling orifice and nozzle to minimize air mixing. The results of the CH_4 calibration is shown in Figure 2.3. The CH_4 densities

and the MS signals have a linear relationship and a linear fit yields a calibration factor of $(7.80\pm0.16)\times10^{12}$ cm^{-3}/(counts/s).

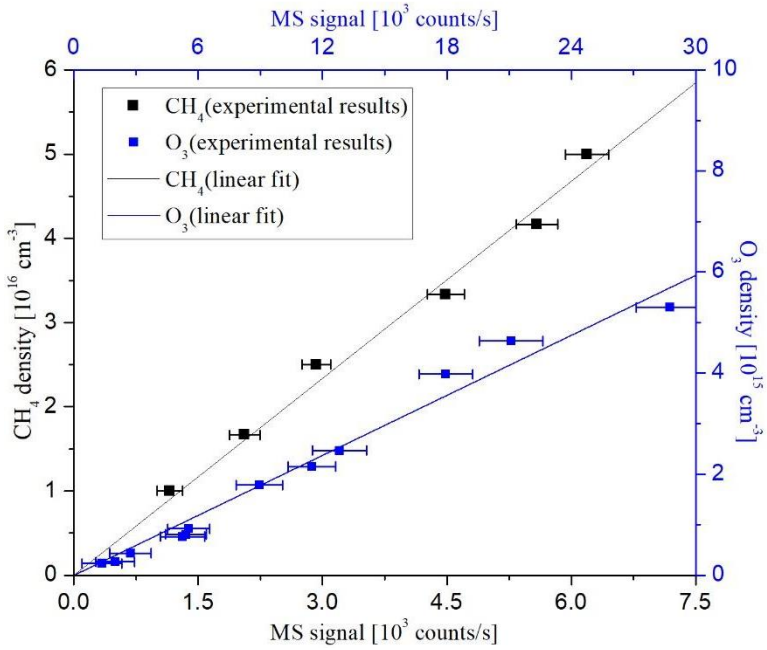

Figure 2.3: CH_4 and O_3 calibration curves obtained in the following gas mixtures: Ar and Ar+20% air for CH_4 and O_3 respectively.

2.3.2 O_3 calibration

O_3 was calibrated with known O_3 densities measured by UV absorption measurements as previously reported [45]. An identical remote DBD plasma source [78] was installed in front of the MBMS system to provide a homogenous O_3 source that was blown at a flow rate of 5 slm towards the sampling orifice in a tube with a diameter of 5 cm to perform the absolute density calibration. The UV absorption measurement was performed inside the tube at the position of the sampling orifice to obtain the average absolute densities of O_3 along the path of the UV light. For O_3 measurements, the background signal (plasma-off) is subtracted from the plasma-on signal for both the plasma and calibration measurements. However, the background for the 50 Hz modulated plasma remains 17% above the gas only background as O_3 relaxation in the background gas of the ionizer takes ~20 ms to reach the

O_3-free background as measured by beam modulation at 20 Hz. This small effect was additionally corrected for. The results of the O_3 calibration are shown in Figure 2.3. A linear relationship between O_3 densities and the MS signals was found and a linear fit yields a calibration factor of $(1.98\pm0.06)\times10^{11}$ cm^{-3}/(counts/s).

2.3.3 Air fraction calibration

The calibration of air was performed by positioning the nozzle very close to the MBMS sampling orifice using different Ar/air mixtures. The air fraction was determined using the MS signal for Ar and N_2:

$$S_{ratio}[\%] = 100 \cdot \frac{S_{N_2}/0.78}{S_{N_2}/0.78+S_{Ar}} \tag{2.4}$$

where S_{N_2} and S_{Ar} represent the detected signal of N_2 (m/z=28) and Ar (m/z=40), respectively. The calibration results are shown in Figure 2.4. A linear relationship between the S_{ratio} and the air fraction is found with a slope of 0.82.

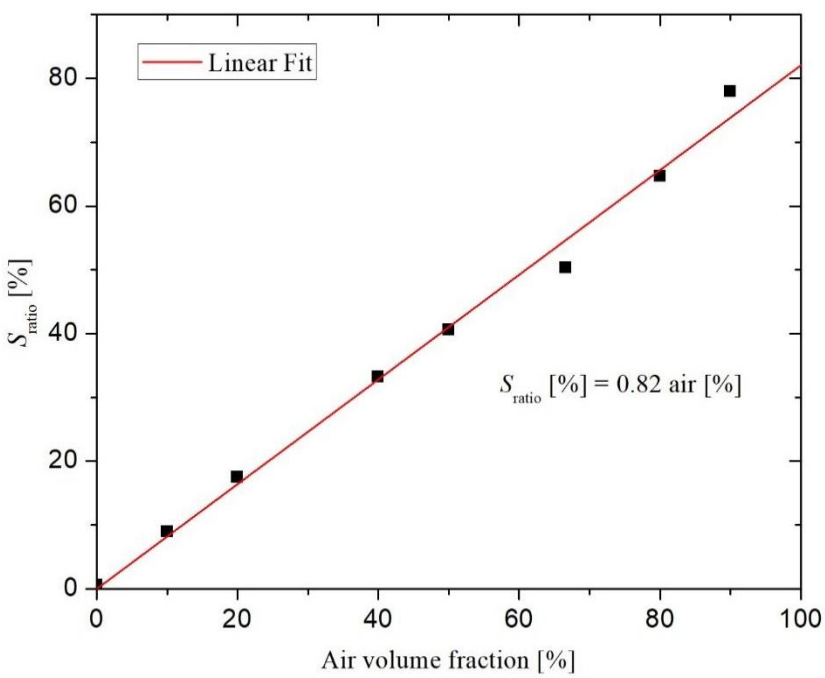

Figure 2.4: Air volume fraction calibration curve using different Ar/air mixtures.

2.3.4 Correlations for the change in background gas composition

During the sampling process the distortion produced by the supersonic expansion due to, for example, scattering of species with the background molecules or from surfaces, can affect the number of the molecules/atoms reaching the MS. This transmission efficiency is background-gas-dependent. Indeed, light molecules in a heavy background gas tend to have a larger radial spread during the diverging expansion. All measurements of this work were performed in ambient air and the background gas composition was different at different nozzle-substrate distances due to the air entrainment in the Ar jet effluent, possibly impacting concentration measurements. Hence, the influence of different ambient air concentrations in Ar on the measured MS signals needs to be taken into consideration. Figure 2.5 shows the recorded MS signals of a fixed CH_4 density (1.65×10^{16} cm^{-3}) and O_3 density (2.0×10^{15} cm^{-3}) as a function of the air fraction in Ar. The constant O_3 densities were obtained by adjusting the power of the DBD source at a specific Ar + air mixture used as the feed gas. The CH_4^+ (m/z=16) signal is in good approximation independent of the air fraction when the air mixing fraction is below 70%. For larger air fractions, the CH_4^+ (m/z=16) signal increases as the concentration of air increases. The MS signals for a given O_3 concentration are more strongly influenced by the background gas composition, having a 40% increase when the air fraction increases from 60% to 75%. The maximum change in MS signal is almost a factor of 3 for the measured range. The increase of air fraction decreases the mass of the background gas, making O_3 comparatively heavier than the background gas. Hence, the increase in MS signals of O_3 with increasing air fraction is due to the concentration of heavier species on the axis of symmetry of the molecular beam.

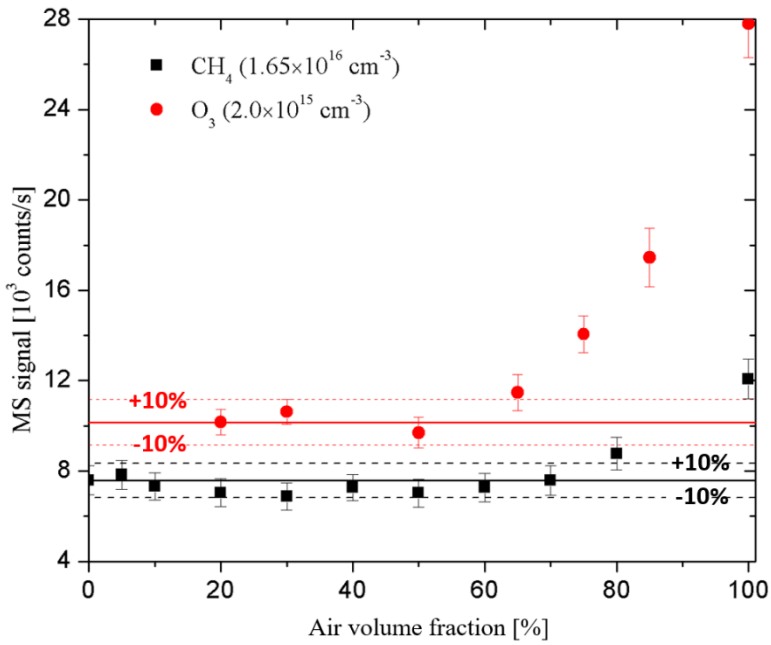

Figure 2.5: CH_4 and O_3 MS signal as a function of air fraction in Ar.

2.4 Pseudo-1D plug flow model

The pseudo-1D plug flow model used in this work was first reported by van Gaens and Bogaerts [79]. This model has been successfully used to simulate free plasma jets [47],[79]–[81]. The main purpose of the model in this work is to calculate the steady-state species densities near the substrate as a function of the axial position of the substrate with respect to the jet nozzle. The plasma jet itself and the afterglow region can be in first approximation regarded as a long cylinder with the assumptions that the axial transport of mass and energy is mainly due to advection, and that the radial transport of species can be neglected. More details about the pseudo-1D plug flow model can be found elsewhere [79]. This method is extended to a jet impinging on a substrate in this work. However, unlike for free jets, the flow patterns and the axial gas velocity distributions are different for the cases of different nozzle-substrate distances. A 2D computational fluid model is used to calculate the fluid flow for each distance between the plasma jet and substrate. The 0D

reaction kinetic model GLOBALKIN developed by the group of Kushner [82] was used. The reaction sets for $Ar/N_2/O_2/H_2O$ mixtures including 55 different species and 1890 reactions reported previously was adopted in this work [79]. An example of the axial power density profile, gas temperature and ambient air fraction used as input for the pseudo-1D plug flow model for a substrate distance of 22 mm is shown in Figure 2.6. The power density profile was adopted from the previous work where the power deposition of the jet used in this work has been investigated in detail by comparing model-predicted and measured O and NO densities in a free jet [81]. The gas temperature profile was taken from the experimental results [47].

MBMS is able to measure the air mixing fraction at the position of the substrate, but not the air fraction distribution between the nozzle and substrate. A 2D k-ε turbulent flow model with species and thermal energy transports in Ansys Fluent was used to simulate the ambient gas mixing in the flow. The Schmidt number in the simulation was adjusted to mimic the turbulence induced by the plasma effect and match the simulated air fraction and the measured air fraction at the substrate within 5%. Figure 2.6 shows the averaged air fraction variation in the flow when the nozzle-substrate distance was 22 mm and also includes the corresponding MBMS measurement of the air fraction at the substrate.

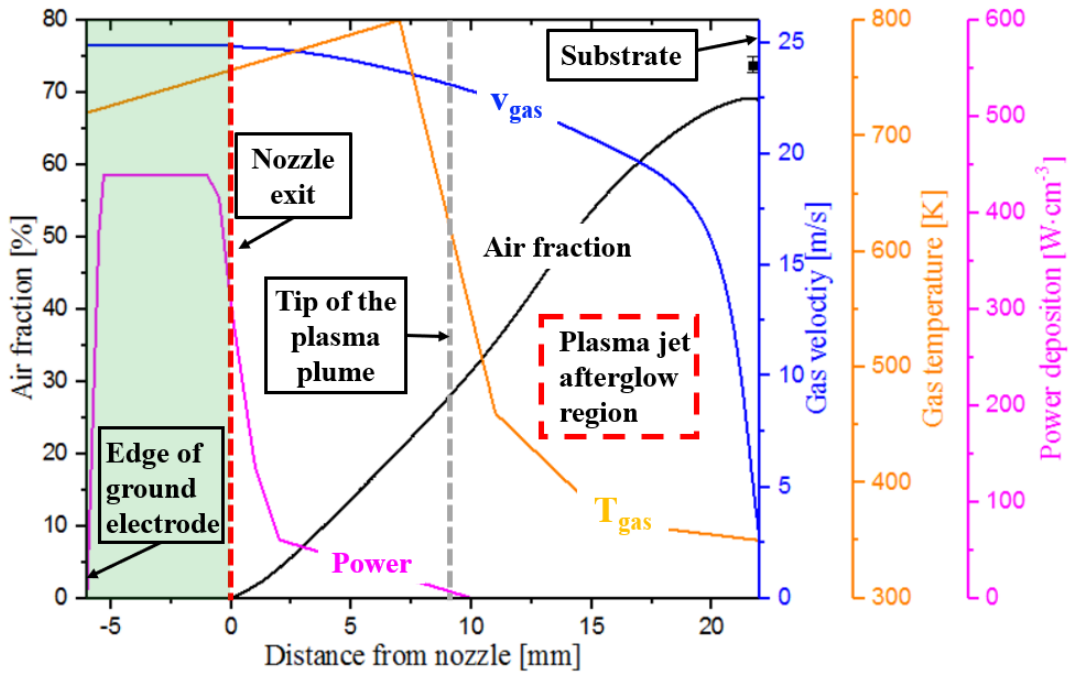

Figure 2.6: Input parameters of the pseudo-1D plug flow model as a function of the axial position along the plasma jet axis for a nozzle-substrate distance of 22 mm. The air concentration measured by MBMS (■) at a distance of 22 mm from the jet is also shown. The visible length of the plasma jet is about 9 mm (indicated with a dashed gray line).

2.5 Linking MBMS results with plug flow model

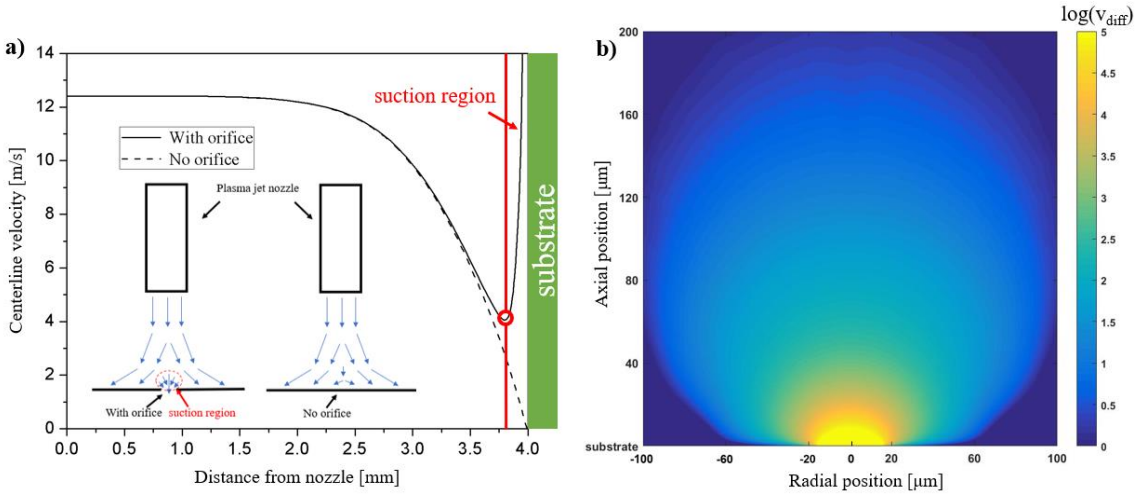

Figure 2.7: Comparison of CFD simulation results with and without an orifice on the substrate for the nozzle-substrate distance of 4 mm: a) Sketch of the flow pattern and simulated velocity along the axis of symmetry, b) Velocity difference distributions (V_{diff}) obtained by subtracting the flow field with and without orifice.

As discussed before, one of the advantages of MBMS is that it can directly measure the species incident on the substrate. In practice, the sampling orifice affects the flow field and samples a zone around the orifice, as illustrated in Figure 2.7(a). Before analyzing the data obtained by MBMS, it is therefore necessary to assess the size of the suction region and determine the methods for comparing the measurements with the pseudo-1D plug flow model.

At atmospheric pressure, the mean free path of gas molecules is around 68 nm, which is much smaller than the sampling orifice (30 μm). As the pressure difference across the orifice is much larger than the critical pressure ratio [14], the velocity of the gas flow will reach the speed of the sound at the inlet of the orifice. Hence, a 2D compressible fluid model from Ansys Fluent was used to simulate the flow field and determine the suction region. Figure 2.7(a) shows the simulated results with and without the orifice when the nozzle-substrate distance is 4 mm. The main difference of the velocity along the axis of symmetry between the two cases is observed for the region within 200 μm from the substrate. Figure 2.7(b) shows the velocity profile difference between the cases with and without the orifice. The flow field is mainly changed within 200 μm from the sampling orifice. The gas residence time in the suction region is around 18 μs, which is negligible compared with the jet flow residence time when the nozzle-substrate distance is within the range of 14-22 mm (between 1-2 ms). Hence, in order to compare the reported modelling and experimental results consistently, the modelling results at the substrate in this work represent the densities 200 μm away from the substrates, corresponding to the outer limit of the sampling suction region of MBMS in the experiments, as shown in Figure 2.7(b).

This suction region is not affected by the nozzle-substrate distance and can be considered constant for all the conditions in this work.

2.6 Results and discussion

2.6.1 Time-resolved measurements of O, O_2 and O_3

Figure 2.8 shows the time-resolved measurements of O, O_2 and O_3 at a nozzle-substrate distance of 16 mm and 22 mm. The calculated TOF delays between species are shorter than the time resolution of 0.1 ms and have no influence on the data in Figure 2.8. The recorded O densities are in the first-order constant during the plasma-on time. The O density quickly drops down to the background level when the plasma is switched off. The measured decay time for O is about 0.5 ms both at 16 mm and 22 mm cases, matching the O decay times obtained by TaLIF measurement in the same jet [54]. The delay time between the plasma-on time and the increase of the O density was much longer than previously obtained by TaLIF [54]. However, the TaLIF measurements were performed at the axial position of 0.5 mm in the active plasma and the measurements reported in Figure 2.8 were at 16 mm and 22 mm in the plasma effluent. In the latter case, the O radicals need to be transported to the substrate and the delay is due to the convective transport time of O from the active plasma to the substrate which is approximately 1.3 ms.

In addition, obvious increases in the O_2 and O_3 densities were observed. This was due to the enhancement of the air mixing triggered by a transient vortex-induced when the plasma is switched on and off. As previously reported [46], transient vortices were observed immediately after the plasma is switched on and off for power modulation at 50 Hz. The created transient vortices then propagate along the jet and it takes about 1 ms for the vortex to reach a distance of 2 cm corresponding to the position of the substrate and the delay time

for O_2 in Figure 2.8. These transient vortices enhance mixing of the surrounding air into the Ar jet effluent, resulting in a temporal increase in the oxygen density. The two observed maxima in the O_3 densities correlate with the observed maxima in the O_2 densities. These maxima remain after correcting for the O_3 density due to the change in air concentration (see Figure 2.5) for d=16 mm but not for the case d=22 mm where the seemingly measured increase in the O_3 density is due to a transient increase in the air concentration. O_3 is mainly produced by the following reaction [83]:

$$O + O_2 + M \rightarrow O_3 + M, \qquad \text{(R3)}$$

where M is a third body being O_2, Ar or N_2. At a fixed O density, an increase in O_2 density (R3) will cause an increase in the production rate of O_3, leading to a higher O_3 density. Furthermore, the decay time for the measured O_3 density is consistent with the gas residence time of 1.3 ms. The decay time for O_2 is however significantly longer than for O_3. This increased relaxation time up to 2-3 ms is consistent with the time necessary for the jet to go back to a more laminar steady-state flow after the flow disturbance as observed by Schlieren measurements [46].

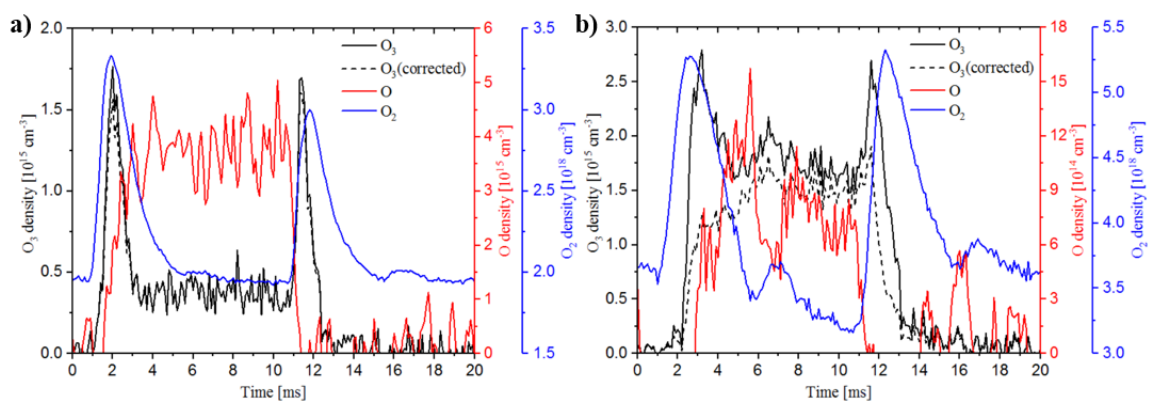

Figure 2.8: Time-resolved measurements of O, O_2 and O_3 for the duration of one RF modulation cycle at a nozzle-substrate distance of (a) 16 mm and (b) 22 mm. The dashed line corresponds to the corrected O_3 densities after eliminating the effects of air concentration using the calibration curve in Figure 2.5. The plasma is on from 0 to 10 ms.

2.6.2 O, O_3 and air concentrations as a function of distance

Figure 2.9 shows an overview of the time-averaged O and O_3 densities during the plasma-on time, complemented with the average concentrations of air both for plasma-on and plasma-off. The impact of air mixing during plasma-on becomes significant when the distance between the plasma nozzle and the MBMS sampling orifice is larger than 18 mm. The O density gradually decreases with increasing nozzle-orifice distance and the O_3 density has the opposite trend. These trends illustrate that large densities of O cannot co-exist with O_3 as it leads to the dissociation of O_3 by O [47]:

$$O + O_3 \rightarrow O_2 + O_2. \qquad \text{(R4)}$$

In the region near the nozzle, O_3 is mainly destroyed by the abundance of atomic oxygen; when the atomic oxygen density decreases in the far effluent region, the O_3 density starts to increase. The atomic oxygen is converted into O_3 through reaction (R3). Figure 2.9 also enables us to estimate the detection limit of O and O_3 which is 1.5×10^{15} cm^{-3} and 3×10^{14} cm^{-3}, respectively, for the experimental conditions.

The measured O and O_3 densities are compared with the pseudo-1D plug flow model results and the comparison is shown in Figure 2.10. The modelling results are radially averaged densities and the experimental results are the time-averaged densities at the position of the suction region on the axis of symmetry. The modelling results reproduce the experimental trends of O and O3 densities and a quantitative agreement with the experimental data is also found in the far effluent. The particular large discrepancy between modeled and experimental O densities at ≤10 mm could be due to the influence of the sampling plate on the discharge (visible plasma plume length is ≈ 9 mm). The sampling plate affects the plasma plume length when the tip of the plume is nearly touching the surface, resulting in a change of electrical characteristics such as the plasma impedance

and power coupling and distribution [10]. In addition, as at the closet distances the gas temperature is larger, there could be an additional contribution of uncertainty in the measured O density due to enhanced difference in temperature of background/calibration signal and plasma-on signal. Nonetheless we did not report MBMS measurements for distances less than 12 mm to minimize these effects. The discrepancy between modeled and experimental O densities also gradually increase from 12 mm to 22 mm. This might be due to the overestimation of O_2 mixing into the jet leading to a faster decay of O through formation of O_3. The difference between the absolute values of the O_3 densities obtained by modelling and experiments might have three origins. First, spatially resolved measurements of O_3 densities in the free jet show that the O_3 density on the axis of symmetry is lower than the off-axis O_3 density up to 14 mm from the nozzle [47]. This is consistent with a lower measured O_3 concentration in the center of the jet compared to the radially averaged density from the model. Secondly, the production of O_3 is strongly impacted by the O_2 concentration (and thus air concentration). The input air concentration in the pseudo-1D plug flow model is calculated based on a turbulent model to obtain agreement with the measured air concentration at the substrate. This might have led to an overestimation of air and correspondingly an overproduction of O_3 in the region near the nozzle where the flow is close to laminar [46]. Lastly, the discrepancy could have also been enhanced by the presence of water vapor impurity in the feed gas. As an example the O_3 density decreases by 25% if 100 ppm water vapor impurity is added to the feed gas in the model.

The O density at 22 mm in Figure 2.8(b), was measured in an Ar-air mixture with 75% air. O is often measured by TaLIF and requires a measurement of the quenching rate of the

excited state O ($3p^3P$) to obtain absolute densities. At 22 mm, the quenching time is 80 ps which is challenging to measure even by picosecond TaLIF with the current detector in use [84]. This makes MBMS an excellent alternative to TaLIF for such conditions.

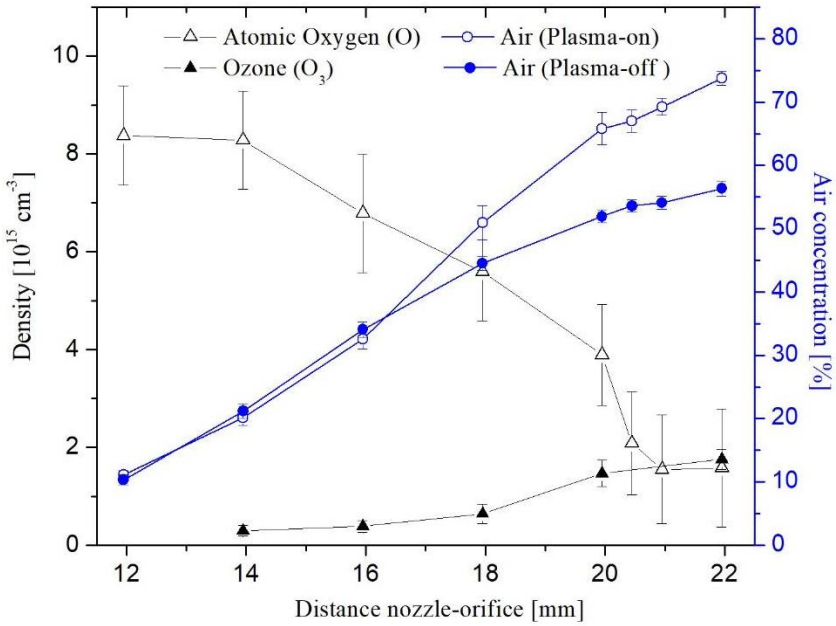

Figure 2.9: Absolute O, O_3 densities and air mixing fraction as a function of distance.

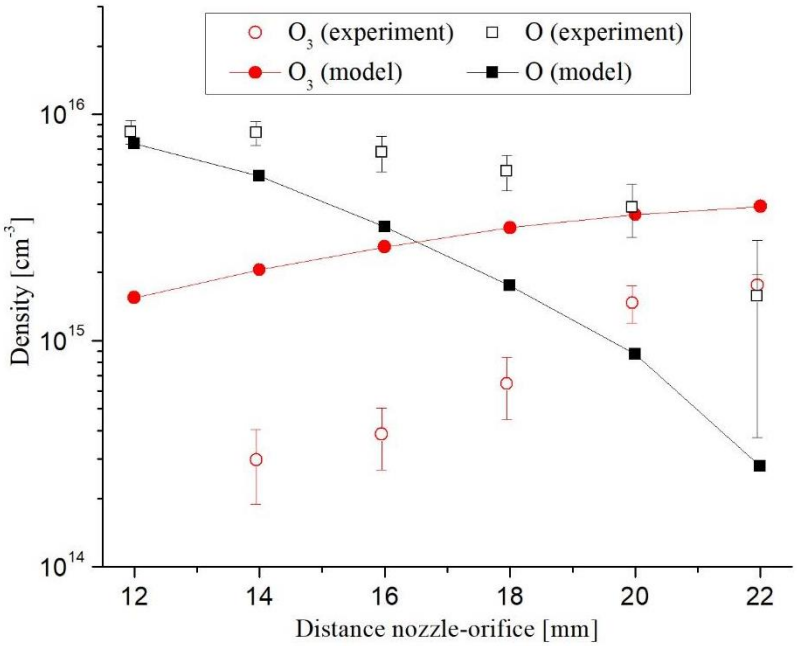

Figure 2.10: Comparison of O and O_3 densities as a function of time obtained from the experiment and the pseudo-1D plug flow model.

2.6.3 Comparison of O and O_3 densities in a jet with and without substrate

Due to the lack of detailed species density measurements of jets impinging on a substrate, the measured species densities in free plasma jets are often used to estimate species fluxes incident upon substrates for applications. Figure 2.11 shows the densities of O and O_3 and axial velocities as a function of the distance from the nozzle, for the same jet with and without substrate at 22 mm. All the input parameters of the model for these two cases were assumed to be the same except for the axial velocity distribution in the flow and the air admixing fraction. The air density in the free jet was obtained from the previous Raman scattering measurements [85]. These two cases allow us to assess the effects of both air admixing and changes in axial velocity distribution. The averaged axial velocity of the free jet flow reduces closer to the nozzle compared to the jet impinging on the substrate. This has a major effect on short-lived species such as O. The longer residence time for the free jet flow makes it difficult for short-lived species to survive at a large distance from the nozzle. This is consistent with previously reported TaLIF measurements in the free jet [81]. The difference between the two cases decreases in the stagnation region near the substrate because convective transport in this boundary layer reduces and transport becomes diffusion dominated. In addition, the different flow patterns with and without substrate can cause a difference in the air fraction along the jet axis. The measured air admixing fraction of the free jet used in the model is 12% lower than that of the impinging jet at the distance of 22 mm. Lower O_2 density along the jet decreases the conversion of O into O_3 through reaction (R3) and results in a higher O density, as shown in the comparison of curves without substrate but with different air admixing data as shown in Figure 2.11. Considering the effects of both air admixing and axial velocity distribution for the 22 mm case, the

species densities for the impinging flow will be higher than that for the free jet flow, particularly for short-lived species.

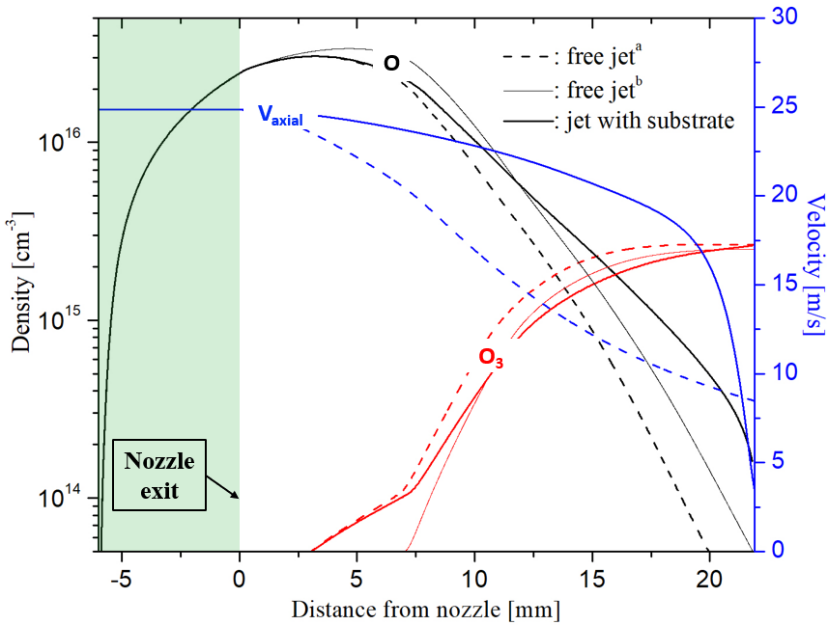

Figure 2.11: Pseudo-1D plug flow modelling results for the same jet with and without substrate (d=22 mm): Densities of O and O_3 and axial velocities as a function of the distance from the nozzle. [a]The air admixing data is based on MBMS result with substrate; [b]The air admixing data is obtained from Raman scattering measurements without substrate [85].

2.6.4 Linking ClO^- formation with O flux

The production of ClO^- associated with bacterial inactivation is reported to likely occur through a reaction between the plasma-produced atomic oxygen and Cl^- in the solution [53]:

$$O + Cl^- \rightarrow ClO^- \qquad \text{(R5)}$$

Hence the production rate of ClO^- is an indication of the flux of O to the solution. We tried to measure the O density under the same plasma conditions as the previously reported ClO^- production rate, but the results showed that the O density was below the detection limit of 1.5×10^{15} cm^{-3}. However, the O density as a function of distance in the free jet with the same plasma conditions as used from the non-touching liquid treatment is reported [86]. Based on these measurements, we estimate the O density at the substrate at a distance of 6

mm, corresponding to the nozzle-liquid distance, with the pseudo-1D plug flow model. The estimated O density at a substrate positioned at 6 mm as shown in Figure 2.12 is 7.0×10^{14} cm^{-3}, close to the detection limit. The previously reported ClO^- formation rate is 0.3×10^{16}/s [53]. The O flux can be calculated by the formula [87]:

$$\Gamma_l = \frac{1}{4} n V_{th} \cdot \alpha_O \cdot A, \tag{2.5}$$

where n is the absolute density of species, V_{th} is the thermal velocity of O, A is the gas-liquid contacting area estimated by the inner diameter of the nozzle, and α is the mass accommodation coefficient used to describe the probability of impinging O atoms on the liquid surface being absorbed into bulk liquid. Unfortunately, the accommodation coefficient of O, α_O, is not reported in literature and we use the accommodation coefficient of OH (α_O=0.83) instead [87].

Estimating the O flux by Equation 5 yields a value of 1.7×10^{17}/s which is almost 2 orders of magnitude larger than the ClO^- production rate. This shows that only 1-2% of the absorbed O in the liquid reacts with Cl^- and forms ClO^-, allowing for ample of other O recombination reactions. As O is the dominant reactive species at 6 mm [86], this suggests that the proposed reaction (R5) is indeed the most likely pathway for ClO^- production.

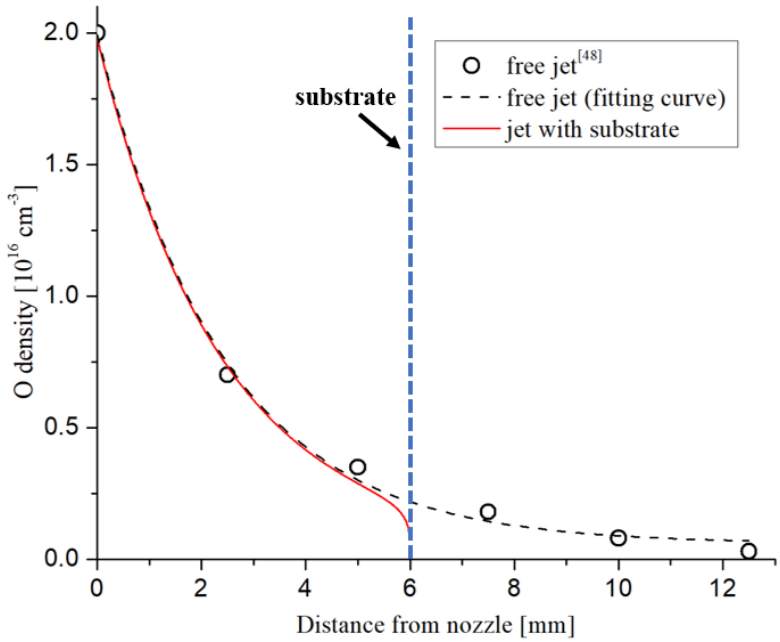

Figure 2.12: Estimated difference of O in the free jet and the jet impinging on a substrate positioned at 6 mm comparable to the jet used for the conditions of OCl^- generation.

2.7 Conclusion

In this work, a time-modulated RF driven atmospheric pressure plasma jet in Ar+1% O_2 operating at 7.6 W was investigated by a molecular beam mass spectrometer. The absolute densities of O and O_3 as a function of nozzle-substrate distance in the afterglow of the plasma jet operating in open air were measured. The detection limits of O and O_3 were 1.5×10^{15} cm^{-3} and 3×10^{14} cm^{-3} respectively. O densities gradually decrease with increasing nozzle-orifice distances and O_3 densities have an opposite trend. Time-resolved measurements of O, O_2 and O_3 during the modulated period showed the temporal increase in O_2 and O_3 densities caused by the transient vortices induced by the switching on and off of the plasma during the modulated cycle. Pseudo-1D plug flow modelling was also performed and the modelling results agree with the experimentally observed trends of O and O_3 densities as a function of the nozzle-substrate distance. It was also shown that the O density distribution as a function of the distance from the nozzle was significantly

different for the free and substrate-impinging plasma jets mainly due to the differences in the flow fields. Previously reported ClO^- production rates in saline induced by the same plasma jet are two orders smaller than the O flux to the saline solution. This is consistent with the previously proposed ClO^- production through the reaction of plasma produced O with Cl^- in solution.

Chapter 3

Spatially resolved density measurements of singlet delta oxygen in a non-equilibrium atmospheric pressure plasma jet by molecular beam mass spectrometry[1]

[1] This chapter is adopted from the previous publication J. Jiang, Y. Aranda Gonzalvo, and P. J. Bruggeman. "Spatially resolved density measurements of singlet delta oxygen in a non-equilibrium atmospheric pressure plasma jet by molecular beam mass spectrometry." Plasma Sources Science and Technology 29.4 (2020): 045023. Due to copyright licensing CONFLICTS, the chapter is NOT INCLUDED IN THE FINAL VERSION of this dissertation but can be found at https://doi.org/10.1088/1361-6595/ab7f4b. The abstract is provided on the next page.

3.1 Abstract

Singlet delta oxygen ($O_2(a^1\Delta_g)$), the first electronically excited state of O_2, plays an important role in many applications. We report the first measurements of absolute densities of $O_2(a^1\Delta_g)$ in an atmospheric pressure plasma jet (APPJ) by molecular beam mass spectrometry (MBMS). The ability to measure axial and radial profiles of $O_2(a^1\Delta_g)$ impinging on a substrate in the effluent of the APPJ is a key advantage of the MBMS diagnostic method over previously reported optical methods. The measured large $O_2(a^1\Delta_g)$ densities in the APPJ effluent, up to one order of magnitude higher than the O density, underline the potential importance of $O_2(a^1\Delta_g)$ in many applications using APPJs.

Chapter 4

Absolute ion density measurements in the afterglow of an RF atmospheric pressure plasma jet[1]

[1]This chapter is adopted from the previous publication J. Jiang and P. J. Bruggeman. " Absolute ion density measurements in the afterglow of a radiofrequency atmospheric pressure plasma jet." Journal of Physics D: Applied Physics 54.15 (2021): 15LT01. Due to copyright licensing CONFLICTS, the chapter is NOT INCLUDED IN THE FINAL VERSION of this dissertation but can be found at https://doi.org/10.1088/1361-6463/abdc91. The abstract is provided on the next page.

4.1 Abstract

Atmospheric pressure plasma jets (APPJs) can enable large fluxes of reactive species impinging on treated substrates in many applications. The relative importance of ionic versus neutral reactive species fluxes produced by APPJs is to date mainly deduced from modeling due to the challenge of measuring absolute ion densities/fluxes. In this study, a calibration was performed to determine the absolute densities of cold ions in the afterglow region of an RF-driven atmospheric pressure plasma jet (APPJ) in Ar + 1% O_2 by molecular beam mass spectrometry. Positive ion densities were found to be about 3-4 orders of magnitudes lower than the densities of the dominant reactive neutral species (O, $O_2(a^1\Delta_g)$, O_3) in the afterglow region of the APPJ at a distance larger than 2 mm from the visible plasma plume. The results illustrate the ability of molecular beam mass spectrometry to enable a quantitative evaluation of both neutral and ionic species in many applications using APPJs.

Chapter 5

Vibrationally excited N_2 measurements in the effluent of an atmospheric plasma jet by molecular beam mass spectrometry[1]

[1] This chapter describes work that is collaboratively performed with Prof. Igor Adamovich's group at the Ohio State University. The 0D kinetic modelling in this chapter is performed by Prof. Igor Adamovich's group.

Nitrogen fixation is one of the most important industrial chemical processes sustaining our society's food production [88]. In order to achieve the activation energy to break the triple bond of molecular nitrogen to enable ammonia production and achieve sufficiently larger ammonia production yields, high operating temperatures (>700 K) and high pressures (100-200 bar) are required in the conventional Haber-Bosh process based on the thermal catalysis. Nonetheless, cold atmospheric pressure plasmas (CAPPs) offer opportunities for operating this process at moderate conditions, e.g., atmospheric pressure and close-to-room temperature. In CAPPs, the energetic electrons transfer their energies acquired from electric fields to other atoms/molecules producing various reactive species including ions, radicals, electronically and vibrationally excited species, while maintaining the gas temperature at close-to-room temperature [23]. Several synergistic effects were previously observed in the combination of plasma and thermal catalysts (referred to as plasma catalysis) in different chemical processes, such as the conversion of methane [18]–[20],[89], reduction of nitrogen oxides [22],[90] and nitrogen fixation [91],[92]. An alternative approach of nitrogen fixation is through the production of NO_x from air originally through the Birkeland-Eyde process which is now also explored with low temperature plasmas [93].

In the context of ammonia synthesis, vibrationally excited N_2 is commonly hypothesized to be a key factor responsible for the observed synergistic effect [94],[95]. The energy stored in the vibrational quanta contributes to overcoming the energy barrier in the dissociation of N_2 at the catalytic surface. To replace or at least compete with the Haber-Bosch process, the current challenge is how to further increase the energy efficiency and the production yields of NH_3 in plasma-catalysis processes or alternatively through NO_x formation [23]. Possible strategies for further improvements are suggested as enhancing

the vibrational excitation by the plasma, which requires the development of diagnostic techniques for the quantitative measurements of vibrationally excited N_2 [23]. While vibrational excitation of N_2 has been proposed as a key mechanism enabling the enhancement of thermal catalysis by plasma [37], this suggested mechanism was based on models. To date, these models have not been verified by the measurement of ground state vibrationally excited N_2 molecules mainly because of a lack of such measurements for conditions typically used for plasma catalysis.

Vibrationally excited N_2 in different plasmas have been previously measured by laser-based diagnostic techniques including coherent anti-stokes Raman spectroscopy (CARS) and spontaneous Raman scattering by several groups [96]–[99]. In addition, there are a few publications regarding the measurements of excited N_2 using molecular beam mass spectrometry (MBMS) [100],[101]. Agarwal et al. [100] measured the excited N_2 in a low-pressure N_2 plasma operating at 1 torr and attributed the shift of the ionization potential of N_2 (~3.6 eV) to the possible presence of $N_2(A^3\Sigma_u^+)$ or vibrationally excited $N_2(X^1\Sigma_g^+)$. Große-Kreul et al. [101] previously indicated the existence of vibrationally excited N_2 in a He-N_2 atmospheric pressure plasma jet (APPJ), however, no detailed information regarding the vibrational temperature or density of vibrationally excited N_2 was extracted from the measurements. Motivated by these studies, in this letter we are reporting an extension of the capability of MBMS to quantitatively measure the vibrational temperature of molecular N_2 in CAPPs near substrates.

An RF-driven APPJ operating in a homogenous gas environment in a vacuum vessel was investigated by MBMS measurements performed in the APPJ effluent. The plasma jet used in this study was identical to the one used in [102] and more information on the

experimental setup can be found in this reference. Detailed plasma conditions will be indicated in the caption of each figure. Similar to the method used for the MBMS measurements of singlet delta oxygen by MBMS [102], we also use the threshold ionization approach to measure vibrationally excited N_2. The ionization potential of ground-state N_2 is 15.6 eV and the shift in threshold of ~3 eV in Ar+1% N_2 APPJ (Figure 5.1 (a)), indicates the presence of excited N_2 species. The possible species leading to this shift in threshold ionization energy include vibrationally excited N_2 or the lowest electronically excited and the metastable state of N_2, $N_2(A^3\Sigma_u^+)$ with excitation energy of 6.2 eV [103]. The density of other electronically excited species like $N_2\left(B^3\Pi_g\right)$ and $N_2(C^3\Pi_u)$ will be too small to be detected as the measurement is performed in the afterglow and the gas residence time is larger than the radiative lifetime of these states.

As shown in eq. (5.1), the MS signal (S_i) of a measured species i is proportional to its electron-impact ionization (EII) cross-section (σ_i) [104]:

$$S_i \sim n_{i,ionizer}\sigma_i(E_{el})\beta I_e T(m_i)\theta(m_i), \tag{5.1}$$

where $n_{i,ionizer}$ is the density of the species i in the ionizer, β the ion extraction efficiency, I_e the electron emission current, $T(m_i)$ and $\theta(m_i)$ respectively represent the mass-dependent transmission efficiency of the mass analyzer and the mass-dependent sensitivity of the detector. As the proportionality factor is a geometrical factor, for a certain species with a given $n_{i,ionizer}$, the MS signals are proportional to the EII cross-sections as a function of electron energy in the ionizer (E_{el}). This relation allows to evaluate the vibrational temperature of $N_2(v)$.

The N_2^+ ion produced by the ionization of ground-state N_2 or vibrationally excited N_2 in the ionizer, results in an MS signal $S_{N_2^+}(E_{el})$. The possible contribution of $N_2(A^3\Sigma_u^+)$ is discarded which will be motivated in detail later. If the vibrational distribution function (VDF, f_v) of the sampled $N_2(v)$ is already known, then the sum of the EII cross-sections of different N_2 species will be proportional to $S_{N_2^+}(E_{el})$:

$$\sum_{v=1}^{v=n} f_v\left(T_{vib}, T_g\right)\sigma_i(E_{el}) \sim S_{N_2^+}(E_{el}), \tag{5.2}$$

where the VDF is dependent in a non-equilibrium plasma on the vibrational temperature (T_v) and the gas temperature (T_g) with T_v typically much larger than T_g. T_v can be varied to fit the normalized MS signals with the normalized total EII cross-section when T_g and the VDF are known. The sum in equation (5.2) does not consider the lowest vibrational level as the collected mass spectra are taken from a modulated plasma and are subtracted with the signal recorded during the plasma off time. Hence the contribution of the ground state N_2 density is subtracted.

Gas temperature. In this work, the gas temperature of the sampled gas was determined using the ideal gas law based on the Ar^+ signals from the MBMS for the plasma ON and OFF cases. The highest temperature was measured to be less than 330 K, and in good approximation we can assume that the gas temperature is room temperature. This also allows to consider the total plasma off N_2 density to be in good approximation equal to the N_2 (v=0) density in the plasma.

EII cross-sections. The EII cross-sections of the vibrationally excited N_2 are not available in the literature and it is assumed that they are the same as for the ground state N_2 with the threshold energy shifted by the vibrational quanta (E_v):

$$\sigma_{N_2(v)}(E_{el}) = \sigma_{N_2(v=0)}(E_{el} - E_v). \tag{5.3}$$

This is a common assumption used in modelling [80].

Total EII cross-section. The width of the electron energy of the ionizer of the system used in this study is 0.5 eV [102]. A Gaussian distribution with a full width at half maxima (FWHM) of 0.5 eV is used to describe the electron energy distribution. The convolution of the electron energy distribution and the EII cross-sections of different N_2 species is calculated accordingly to obtain the modified EII cross-sections $\sigma'_{N_2(v)}$:

$$\sigma'_{N_2(v)} = (\sigma_{N_2(v)} * G_{FWHM=0.5\ eV})(E_{el}). \tag{5.4}$$

Vibrational distribution function. The anharmonicity of N_2 and complex collisional vibrational energy transfer can yield a complex VDF of N_2 in non-equilibrium plasmas. The higher vibrational levels are overpopulated compared with the Boltzmann distribution, and hence the well-known Treanor distribution is used to describe a non-equilibrium VDF of diatomic molecules:

$$f(v, T_v, T_0) = B\ exp(-\frac{\hbar\omega v}{T_v} + \frac{x_e \hbar v v^2}{T_0}), \tag{5.5}$$

in which x_e is the coefficient of anharmonicity and B is determined by ensuring that the sum over all vibrational levels yields 1. Nevertheless, the Treanor distribution is a parabolic function having an inversion point at $v_{min}^{Tr} = \frac{1}{2x_e}\frac{T_0}{T_v}$. The VDF of N_2 has been extensively studied by state-to-state (STS) finite rate methods [105]–[107] and analytical theory by Rusanov and Fridman group [108]–[110]. This approach was validated by Viegas *et al* [28] in CO_2 plasma which showed that the theoretical Treanor distribution is only valid up to

its minimum [111], and is followed by a plateau region of the VDF. In this work, we adapted the hyperbolic function for the plateau region from [110]:

$$f(v, T_v, T_0) = B\frac{v_{min}^{Tr}}{v}\ exp\left(-\frac{T_0\hbar\omega}{4x_e T_v^2} - \frac{1}{2}\right),\ v > v_{min}^{Tr}. \tag{5.6}$$

When the vibrational energies exceed a critical value, a transition from the plateau region to a quickly decreasing Boltzmann distribution should occur according to analytical theory. The criteria of this transition point can be found in [110]. In this study, we truncate the VDF of N_2 at level v=12 for simplicity, assuming that the densities of higher vibrational levels are sufficiently low and do not significantly contribute to the MS signal for the vibrational temperatures measured in this work with the exception of the highest measured T_v which is discussed in detail below.

The measurements have been complemented with a 0D kinetic model describing the N_2 plasma kinetics including 40 vibrational levels as found in [112]. The volume between the needle electrode and the grounded electrode of the APPJ is taken as the plasma volume to calculate the power density from the measured plasma power. The gas velocity on the center axis of the jet as obtained from a 2D computational fluid mechanics model as described in [113] is used to convert the calculated results as a function of time to the spatial coordinate consistent with a plug flow description of the plasma jet.

The normalized MS signals of N_2 and EII cross-sections of $N_2(v)$ in the effluent of an Ar+1% N_2 APPJ, as shown in Figure 5.1(a). The vibrational temperatures are respectively fitted as ~2600 K, ~2300 K and ~1900 K for the MS measurements at a distance of 2 mm, 8 mm and 14 mm from the APPJ nozzle using the Treanor-like VDF as described above. Figure

5.1 (a) also shows that the measurements significantly deviate from the Boltzmann distribution.

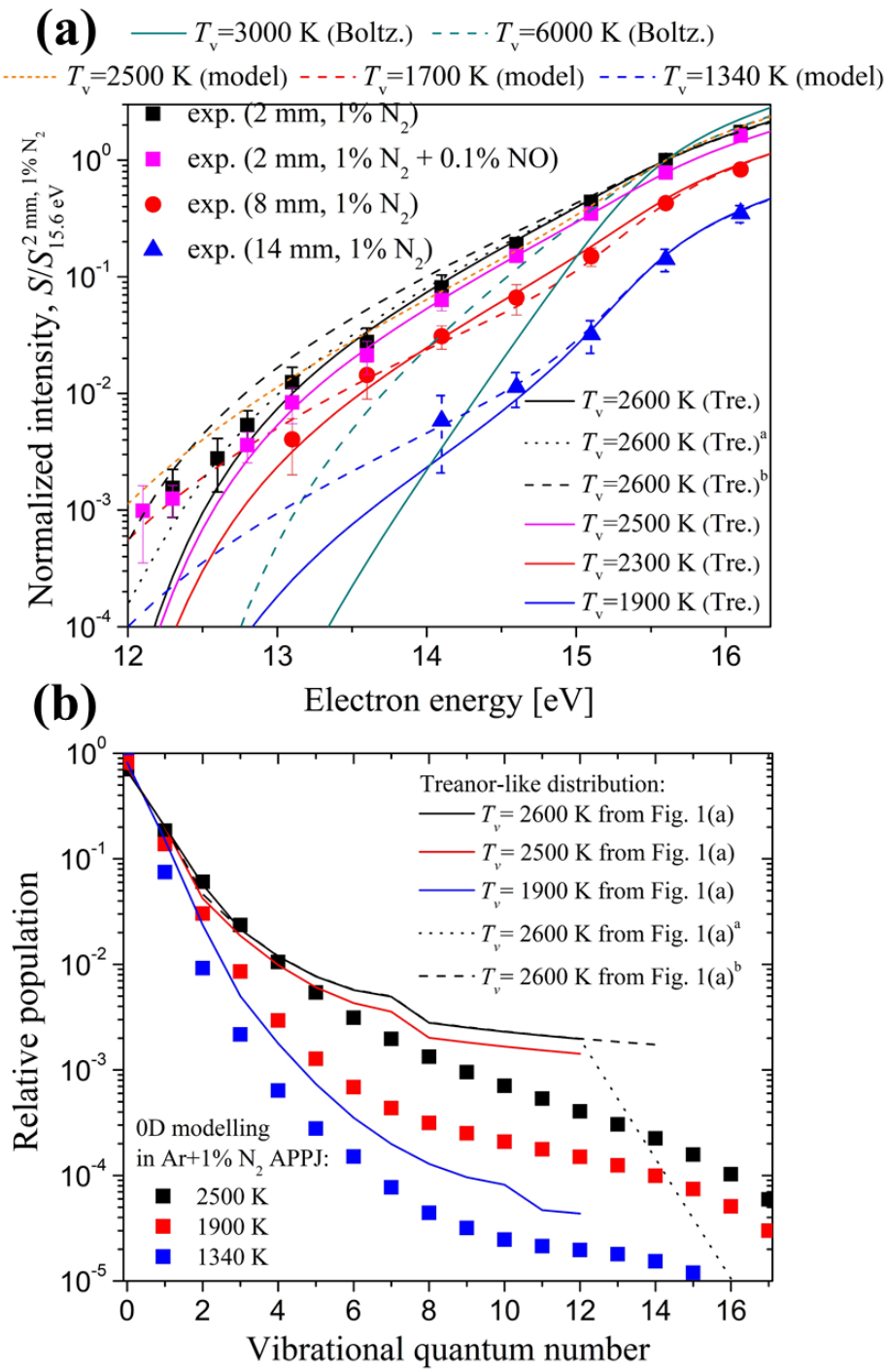

Figure 5.1: (a) Normalized MS signals of N_2^+ and EII cross-sections of $N_2(v)$ as a function of electron energy. The plasma conditions are: feed gas – Ar (1 slm) + 1% N_2,

RF modulation-20 kHz at 50% duty cycle, plasma dissipated power - 1.3 ±0.1 W. with exception of the case marked as 1% N_2+ 0.1% NO which included an additional 0.1% NO and was operated with a plasma dissipated power of 3.6 ±0.1 W. The distance represents the distance from the nozzle of the jet to the substrate. A fitting of the MS spectra with the calculated VDF's by the 0-D kinetics model is also included. (b) Comparison of measured VDFs of N_2(v) with 0D modeling prediction for selected cases shown in Figure 5.1(a). The non-smooth transition between v is 7 and 8 is due to the transition between the Treanor distribution and the plateau region. The superscript 'a' and 'b' in both figures indicates that these two fittings consider vibrational levels v>12. The superscript 'a' represents a fitting truncated at v=20, and the vibrational levels higher than v=12 follow a quickly decreasing Boltzmann distribution with temperature parameter equal to the gas temperature. The superscript 'b' represents a fitting truncated at v=14 with the plateau region extended.

The MS signal recorded at a distance of 2 mm from the APPJ nozzle significantly deviates from the fitting in the ionizer electron energy region between 12.0 and 12.5 eV. Considering that the VDF of N_2 is truncated at v=12, this deviation is likely due to the contribution to the signal of higher vibrational levels (v>12). The two fits include an extrapolation of the plateau region up to v=14 and an extension of the VDF up to v=20 assuming a decrease of the higher vibrational levels according to a Boltzmann distribution and assuming an extrapolation of the plateau region. These fitting approaches bring the deviation between the MS signal and the fit within the experimental accuracy. Another possible explanation of the tail in the mass spectrum signal at low electron energies is the presence of the metastable $N_2(A^3\Sigma_u^+)$ with an energy of 6.2 eV. However, the density of $N_2(A^3\Sigma_u^+)$ predicted by the 0-D model is ~10^{12} cm^{-3}, which is too small to significantly contribute to the measured MS signal and further confirms that the $N_2(A^3\Sigma_u^+)$ is not the reason for the observed deviation. This is further confirmed by the addition of 0.1% NO, an effective quencher of $N_2(A^3\Sigma_u^+)$[114] but not effective in vibrational – translational energy transfer with N_2(v) [115][116] to the feed gas of the APPJ which did not lead to any significant change in the mass spectrometer signal (Figure 5.1(a)).

Figure 5.1(b) shows a comparison of the VDF between the Treanor-like distribution implemented in Figure 5.1(a) and the model predicted VDF for the Ar+1% N_2 case. Excellent agreement is found for the first 6 vibrational levels. This comparison provides further support for the use of the Treanor distribution at least up to the vibrational level 6 to fit the MS signals.

The modeling predictions of T_v and the atomic N density as a function of distance in the effluent of the APPJ operating in Ar+1% N_2 are compared with their respective MBMS measurements in Figure 5.2. Note that the experimentally obtained T_v in Figure 5.2 was determined by the ratio of MS signals at 14.6 eV and 15.6 eV. The comparison shows that while the measured N density has a good match with the model prediction, the calculated T_v decays more rapidly compared to the experimental data. The decay of T_v can be impacted by gas mixing in the APPJ effluent, an effect not included in the 0D model. However, cold N_2 gas admixing from the surrounding would lead to a reduction in the experimentally measured T_v and hence cannot explain the discrepancy between experiment and model. Nonetheless, in order to quantify the effect of gas mixing in the jet effluent on the measured T_v, the distance between the discharge region and the substrate is changed at a fixed nozzle-to-substrate distance ($d_{n\text{-}s}$=5 mm) to maintain a constant gas flow pattern [117]. The increased deactivation of N_2 (v) on the wall of the quartz tube can be neglected as the radial diffusion time constant is of the order of 10s ms while the axial convection gas residence time ~1 ms. When comparing the results with the case of a fixed nozzle-to-substrate distance but with the axial distance rescaled on the same axis considering the difference in gas residence time no significant difference was found. Therefore, the decrease of the

vibrational temperature is dominantly determined by the collisional processes and not significantly influenced by gas mixing.

In order to assess the impact of the assumed VDF on the determined T_v from the experiment, we also used the VDFs obtained by the model to fit the experimental data, as shown in Figure 5.1(a). With the modeled VDFs, vibrational levels up to 40 are considered in the fitting processes. The result shows an excellent fit when using the modeled VDFs and yields a significantly lower T_V. This T_v, fitted with modeled VDFs (Figure 5.2), matches evidently the modeled T_v. This indicates that the discrepancy in T_v between model and experiment is significantly impacted by the assumed VDF particularly for higher vibrational levels used to fit the MS data and underlines the necessity for an accurate VDF to interpret the MBMS data.

The analysis of the modeling results indicates that V-T relaxation in collisions with N are the most dominant processes responsible for the decay of T_v. The rate coefficients obtained from the quasi-classical trajectory calculation predictions by Esposito et al [118], over a wide range of temperatures and vibrational quantum numbers were used in the 0-D model. However, these rate coefficients have never been measured at ambient temperatures according to the authors' knowledge. As both electron-impact excitation of N_2 and V-V relaxation are reported in detail in the literature, the uncertainties in the rates of V-T relaxation might be the largest uncertainty although the excellent agreement between experiment and model, including the fitting of the measured total ionization cross sections by the MBMS as shown in Figure 5.1(a) gives additional confidence in the data.

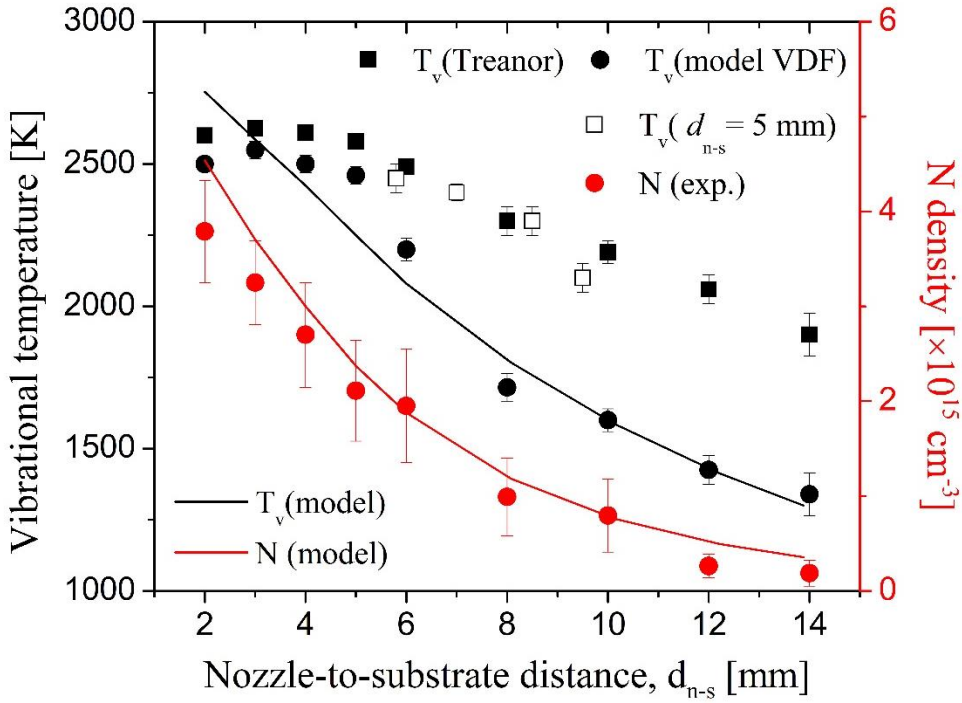

Figure 5.2: Comparison between the vibrational temperature of $N_2(v)$ and N density in Ar+1% N_2 APPJ obtained by MBMS measurements and 0-D kinetic modeling predictions as a function of APPJ nozzle to substrate distance. The open squares (converted to the same axial distance unit to account for the difference in gas residence time) represent the data obtained by changing the discharge region from the substrate but at a fixed nozzle-to-substrate distance ($d_{n\text{-}s}$=5 mm).

Figure 5.3(a) presents vibrational temperatures of $N_2(v)$ in different Ar+N_2+O_2 APPJs as a function of the nozzle to substrate distance in the APPJ effluent. For all the cases, the vibrational temperature decreases with increasing distance. The 1% N_2 case has the highest vibrational temperature even the plasma dissipated power is only one-third of the cases with added O_2. Also, there is no significant difference between the case of 0.1 and 1 % O_2 concentrations. Higher O_2 density can lead to a higher electron temperature which might be favorable for the vibrational excitation of N_2 considering the well-known 2.3 eV resonance peak in electron–N_2 collision [119]. However, the increase of O_2 concentration enhances the deactivation of $N_2(v)$ via the vibrational-vibrational (V-V) relaxation reactions between $N_2(v)$ and O_2, and also drastically impacts the radical densities of N and

O. As shown in Figure 5.3 (b) the N density drops below the MBMS detection limit upon addition of O_2 but is replaced by O and NO at similar densities. This might explain the small difference between the cases with different O_2 concentrations.

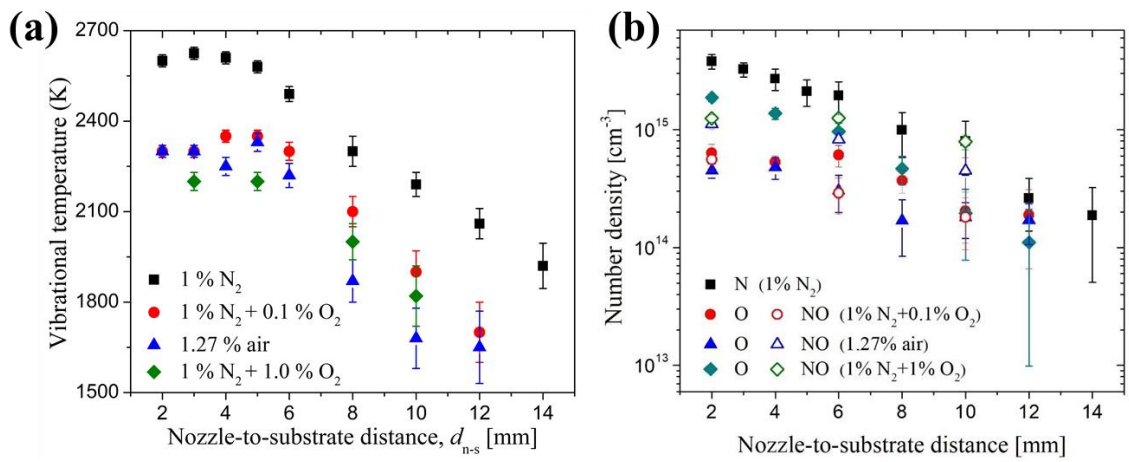

Figure 5.3: (a) Vibrational temperatures of $N_2(v)$ in $Ar+N_2$ or $Ar+N_2+O_2$ mixtures in the APPJ effluent as a function of nozzle-to-substrate distance. The plasma conditions of the case marked as 1% N_2 are identical to the one in Figure 5.1. The cases marked as 1% N_2 + O_2 have the same plasma conditions as the 1% N_2 case with the only exception that the plasma dissipated power is 3.6 ±0.1 W. (b) N, O and NO densities as a function of nozzle-to-substrate distance in different plasma conditions. The plasma conditions correspond to those in Figure 5.3(a).

Although there are some differences between reaction rate coefficients of V-T relaxation of $N_2(v)$ upon collisions with N and O, it is commonly accepted that the V-T relaxation by collisions with O and N dominates V-T relaxations over collisions with molecules and noble gas atoms [115],[116],[120]–[122] . Hence the V-T relaxation in O_2 containing mixtures will be due to O atoms. However, the V-V relaxation of $N_2(v)$ upon collisions with O_2 will also impact T_v as in the presence of 1% O_2 the time scale of the V-V reaction with O_2 reduces to 10^{-2} ms [120]. Hence, a significant part of the vibrational energy of $N_2(v)$ is transferred on a timescale much smaller than the gas residence time to $O_2(v)$ which

is converted more efficiently to translational energies via the more efficient V-T relaxation pathways of $O_2(v)$ explaining the lower T_v in the presence of O_2.

In conclusion, vibrationally excited N_2 measurements in the effluents of APPJs by MBMS were presented in this letter. For the first time, the MS signals were fitted with the EII cross-sections to obtain a vibrational temperature of ground state N_2 by assuming a Treanor-like VDF and considering the calculated VDF by a 0-D kinetic model resolving 40 vibrational levels. The vibrational temperatures of $N_2(v)$ decrease with increasing distance from the APPJ nozzle and are strongly coupled with the decrease in N density. The vibrational temperature of $N_2(v)$ decreases upon the addition of O_2 to the feed gas, possibly enhanced by V-V relaxation upon collisions with O_2. The method and results presented in this letter further extend the capability of MBMS to quantitatively measure vibrationally excited species. Although this method relies on the assumption of the VDF of N_2, it provides a complementary diagnostic technique for detecting $N_2(v)$ near substrates with excellent sensitivity. The reported results might enable a more quantitative analysis of the role of vibrational excitation in plasma catalysis in the context of NH_3 or N_xO_y synthesis.

Chapter 6

Tuning plasma parameters to control reactive species fluxes to substrates in the context of plasma catalysis[1]

[1] This chapter is adopted from the previous publication J. Jiang and P. J. Bruggeman. "Tuning plasma parameters to control reactive species fluxes to substrates in the context of plasma catalysis." Journal of Physics D: Applied Physics 54.21 (2021): 214005. Due to copyright licensing CONFLICTS, the chapter is NOT INCLUDED IN THE FINAL VERSION of this dissertation but can be found at https://doi.org/10.1088/1361-6463/abe89a. The abstract is provided on the next page.

6.1 Abstract

The key reactive plasma-produced gas phase species responsible for the enhanced conversion of chemicals in plasma catalysis compared to thermal catalysis have to date not been identified. This outstanding question is mainly due to the inherent large variety of plasma-produced species and the challenge of controlling and measuring the flux of each constituent of the cocktail of reactive species to a (catalytic) substrate. In this paper, we explore the possibility to control the dominant reactive species fluxes, relevant for plasma-catalysis, to a substrate in the effluent of an RF driven Ar-O_2 plasma jet. The absolute species densities of the major reactive species (O, $O_2(a^1\Delta_g)$, O_3 and ions) were quantified by molecular beam mass spectrometry (MBMS) to assess the possibility of using treatment distance, O_2 admixture concentration, plasma dissipated power, RF modulation frequency and duty cycle as well as the feed gas flow rate to alter the dominant species densities. Selected experimental results were also compared with a pseudo-1D plug flow model. The short-lived and long-lived species can be effectively separated by changing the treatment distance and the RF modulation frequency. Furthermore, adjusting the O_2 admixture concentration enables to change the ratio of the $O_2(a^1\Delta_g)$ and O_3 density. The changes in the trend of ion and O flux were found to be very similar for nearly all investigated parameters. Nonetheless the gas flow rate was able to significantly change the ratio of the O and ion density in the plasma jet effluent. The impact of the surface-dependent loss probability and boundary layer reactions on the species flux to a substrate and how this qualitatively relates to the MBMS density measurements is further addressed.

Chapter 7

Ion fluxes and memory effects in an Ar-O_2 modulated RF-driven atmospheric pressure plasma jet[1]

[1] This chapter is adopted from the previous publication J. Jiang and P. J. Bruggeman. "Ion fluxes and memory effects in an Ar-O_2 modulated RF-driven atmospheric pressure plasma jet." Plasma Sources Science and Technology 29.4 (2020): 045023. Due to copyright licensing CONFLICTS, the chapter is NOT INCLUDED IN THE FINAL VERSION of this dissertation but can be found at https://doi.org/10.1088/1361-6595/ac2045. The abstract is provided on the next page.

7.1 Abstract

In this paper, we report a characterization of ion fluxes impinging on substrates as produced by a modulated RF-driven atmospheric pressure plasma jet operating in a homogenous gas environment (Ar+1% O_2) using molecular beam mass spectrometry (MBMS). The influence of the RF modulation frequency (100 Hz-20 kHz) upon the ion fluxes was investigated by time-resolved measurements, and lifetimes of the dominant ions, O_2^+, NO^+, O^-, O_2^- and O_3^-, were found to be 28±2 μs, 117±8 μs, 7.3±0.4 μs, 17±1 μs, and 23±2 μs, respectively. The absolute ion densities in the near afterglow region were found to be on the order of 10^{11} cm^{-3}. Significant differences in the dynamics of the positive and negative ions were found and explained by significant electron densities in the afterglow produced by electron detachment reactions from negative ions due to the large concentrations of atomic oxygen and singlet delta oxygen. Transitions in ion flux dynamics for different modulation frequencies and at the startup of the plasma were analyzed together with ICCD images recording the plasma propagation, to assess the dynamics of plasma plume propagation and how it is impacted by "memory effects". Quantitative measurements of the ion densities enabling these memory effects are reported. The results in this paper highlight the tremendous impact of memory effects on plasma propagation and their corresponding pre-ionization.

Chapter 8

Plasma catalytic partial oxidation of methane into syngas: synergistic effects and reaction mechanism[1]

[1] This chapter describes work that is collaboratively performed with Prof. Gottlieb Oehrlein's group at University of Maryland. This chapter is based on the collaborative paper Li et al. " Characterization of plasma catalytic decomposition of methane: role of atomic O and reaction mechanism." Accepted by *J. Phys. D. Appl. Phys.* https://doi.org/10.1088/1361-6463/ac4728

8.1 Introduction

Plasma catalysis has received a lot of attention in recent years due to its potential application in industrial chemical processes such as ammonia and syngas synthesis [23]. When compared to gas conversion by plasma and thermal catalysis alone, synergistic effects in plasma catalysis enabling higher conversion rates and lower activation energies were reported in many studies [30],[36]. Nevertheless, the mechanisms underpinning plasma-catalysts interactions are to date not fully understood, which is an inhibitor for further improvement and scale up to enable the implementation of plasma catalysis in industry.

Compared with thermal catalysis, plasma-produced reactive species such as radicals, electronically and vibrationally excited species are suggested to be responsible for the observed synergistic effects because of the lower reaction energy barriers or the possible new reaction pathways initiated by them on catalyst surfaces. For example, Mehta et al. [37] postulated that plasma-produced vibrationally excited N_2 decreased dissociation barriers on catalyst surfaces in ammonia synthesis based on a microkinetic model. They also predicted that the plasma enhancement would be beneficial for metals that bind reagents too weakly in thermal catalysis. While the modelling result is promising, it has not been confirmed by experiments and many other plasma-produced species and effects might contribute to the observed synergistic effects which were not considered in the model. Further studies regarding the reactive species on the catalyst surface at atmospheric pressure are still needed to have a better understanding of plasma-catalyst interactions.

In this chapter, the partial oxidation of methane into syngas ($CH_4 + ½ O_2 \rightarrow CO + 2H_2$) is selected as an example system to investigate the plasma-catalyst interaction. Syngas,

a mixture of CO and H_2, is used to make industrial chemicals and fuels such as methanol by the subsequent synthesis. Pietruszka et al. [29] investigated the influences of plasma operating parameters on the product distribution of partial oxidation of methane in a dielectric barrier discharge (DBD) reactor with catalysts, and found that the presence of Ni/Al_2O_3 in the discharge region could lead to the oxidation of CO to CO_2 at 300 ºC and above. Plasma-produced reactive species were supposed to be responsible for the change in surface chemistry. Song et al. [30] studied the hydrogen production from partial oxidation of methane using a DBD reactor with $NiO/\gamma\text{-}Al_2O_3$ catalysts. They showed that the CH_4 conversion and H_2 yield using a DBD reactor filled with catalyst pellets inside increased from 60.1% and 21.3% to 83.6% and 28.4% respectively, compared with the DBD reactor without catalysts. It was hypothesized that the plasma excited the reactants and therefore the absorption energy of CH_4 and O_2 on the catalyst surface was reduced, and that the plasma also promoted the desorption of products from the catalyst surface. While many studies have been reported that study gas conversion, previous studies which focus on the mechanism of plasma-catalyst interaction are very rare.

As motivated in Chapter 1.4, the atmospheric pressure plasma jets (APPJs) are used as the plasma source instead of a DBD reactor, enabling the decoupling of plasma and catalysts. The tunable parameters of APPJs help to create highly different plasma conditions which are beneficial for assessing the roles of different reactive species produced by the plasma. Successful examples can be found in the utilization of APPJs in nanoparticle synthesis [123] and bacteria inactivation [53].

In this chapter, we correlate the plasma-produced species fluxes with the *in situ* measured changes of the species adsorbed on the catalytic surfaces. This will allow assessing which

species might be responsible for the observed surface modifications and lead to a further understanding of the fundamental mechanisms leading to the synergistic effects. The characterization of the catalytic surface and downstream gas phase was performed by collaborators at the University of Maryland using diffuse reflectance infrared Fourier transform spectroscopy (DRIFTS) and IR absorption. The plasma-produced reactive species fluxes were quantitatively measured at the University of Minnesota by molecular beam mass spectrometry (MBMS) for the same plasma operation conditions.

8.2 Experimental setups and conditions

The schematic of the plasma-catalyst reactor is shown in figure 8.1. At the University of Maryland, the APPJ was incorporated with a high-temperature reaction chamber through a homemade flange, enabling the *in-situ* catalyst surface characterization using DRIFTS. The obtained absorbance spectra were analyzed and found to be due to CO, CH_n and oxygenates adsorbed at the catalyst substrate. Details of the DRIFTS setup and characterization can be found in [36].

The downstream gases of the reactor were monitored by real-time absorption by Fourier-transform infrared spectroscopy (FTIR). The exhaust of the plasma-catalyst reactor was guided into a homemade absorption cell with a 15 cm optical path length sealed with two ZnSe windows, where the absorption measurements were performed. Detailed information on the setups and methods can be found in [36].

8.2.3 Characterization of plasma-produced species fluxes

Densities of reactive species produced by APPJs were measured by molecular beam mass spectroscopy (MBMS) at the University of Minnesota. The APPJ was installed in a vacuum chamber, perpendicularly to the sampling substrate of the MBMS, as shown in Figure

8.1(b). The most dominant reactive species produced in Ar + O_2 APPJ were measured in this study. The interpretation of the MBMS results including the analysis of the suction region and boundary layer effects were performed in chapters 2 and 6. These results indicate that the species densities measured by MBMS can represent the densities of the species reaching the catalyst bed in the plasma-catalyst reactor in this study as the sampling does not occur in the diffusive boundary layer. The details of the measurements have been reported in chapters 2 and 3.

8.2.4 Catalyst materials

Nickel (Ni) is a common catalyst used in thermal catalysis for the partial oxidation of methane. Hence, Ni catalyst in the form of powder with a weight percentage of 65% and supported by 13 wt% alumina and 12 wt% silica, was used in this experiment. The size of the Ni power was ~10 µm according to the SEM image [35]. Another powder material, kieselguhr (>95% amorphous silica), was used as a non-reactive substrate as a reference measurement to enable us to assess the impact of the Ni catalyst. Both Ni catalysts and kieselguhr were loosely packed in the catalyst holder (indicated in figure 8.1), to ensure a low flow resistance through the catalyst holder. Moreover, as pointed out in [35], the gas flow through the APPJ was at most 600 sccm to ensure the catalyst was not fluidized in the reactor.

8.2.5 Experimental conditions

Mixtures of different concentrations of O_2 (0.5%, 1.0% or 1.5%) in Ar (200 sccm) were flown through the APPJ into the chamber, and 2 sccm CH_4 mixed in 400 sccm Ar was injected downstream of the APPJ near the catalyst bed. The CH_4 and O_2 feed mixed downstream of the APPJ. Note that the CH_4 is not present in the main discharge region of

the APPJ. The distance between the nozzle of the quartz tube and the catalyst bed was fixed at 5 mm in the plasma-catalyst reactor. For the MBMS measurements, the densities of reactive species were also measured at 5 mm from the jet nozzle, where the catalyst bed was replaced by a stainless-steel substrate containing a sampling orifice [113]. The measured species fluxes by the MBMS are independent of the material of the sampling substrate. The APPJ was not touching the catalyst bed for all the conditions in this study, and the plasma power was in the range of 0-3.5 W.

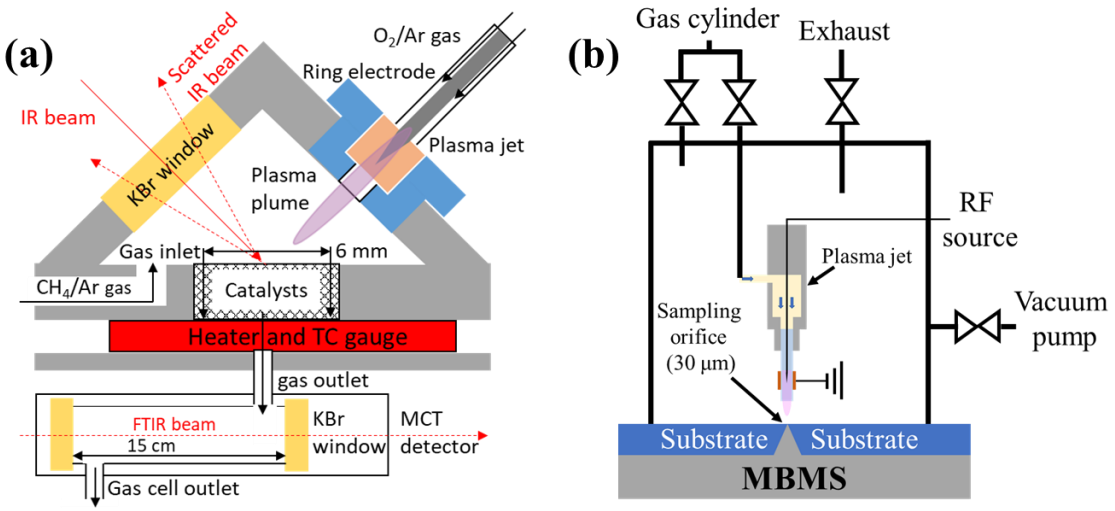

Figure 8.1: (a) Schematic of the setup used for studying plasma-catalyst interactions including DRIFTS and downstream absorption measurements [36]; (b) Schematic of the MBMS setup to measure plasma-produced reactive species. (a) Reprinted with permission from ref [124] © 2021 IOP Publishing.

Before the start of the measurements, the gas lines and reactor chamber were pumped down to 10^{-5} torr and refilled with pure argon flow to eliminate CO_2 and water vapor impurities. In addition, the temperature of the catalyst bed was adjusted from room temperature (25 ^{o}C) to 500 ^{o}C in this study. The heating rate of the catalyst bed was 10 ^{o}C/min.

8.3 Results and discussion

8.3.1 Impact of catalyst heating

Considering that the catalyst bed will be heated up to 500 ºC in the following experiments and the MBMS measurements are performed at room temperature, this temperature increase might potentially affect the plasma-catalyst interaction, particularly the reactive species fluxes reaching the catalysts. It is therefore important to assess the influence of heating on the plasma-produced species flux in this specific reactor before further analysis.

Kieselguhr powder was firstly tested and treated by the APPJ to assess the CH_4 conversion at two different temperatures (25 °C and 500 °C). Kieselguhr is mostly made of amorphous silica which does not have any catalytic properties. This means that the CH_4 conversion should be dominated by gas-phase reactions and all the products of interest are anticipated to be produced directly by the plasma. Figure 8.2 shows the CH_4 densities as well as CO and CO_2 densities at the outlet of the reactor in figure 8.1(a) as a function of the plasma dissipated power for kieselguhr powder at 25 °C and 500 °C. The results show that there are no significant differences observed in both CH_4 conversion and CO and CO_2 production, indicating that the heating of the kieselguhr bed up to 500 ºC has a negligible effect on the CH_4 conversion.

In addition, the potential heating effect on the plasma-produced species flux to the catalyst bed can be further understood when comparing the estimation of the timescales of gas convection and thermal diffusion. The convection timescale over a distance of 1 mm when approaching the catalyst bed is estimated to be ~1.7 ms, based on the gas velocity entering the catalyst holder obtained from mass continuity. The timescale of thermal diffusion is estimated to be on the order of ~45 ms over a distance of 1 mm (based on l^2/α, with l the

characteristic length and α, the thermal diffusivity of Ar 2.2 ×10^{-5} m^2 s^{-1}), which is much larger than the corresponding convection timescale (~1.7 ms). Therefore, the convection dominates over the heat diffusion and there is a negligible temperature gradient in the upstream gas phase before the catalyst holder when the catalyst is heated. Hence the plasma-produced reactive species fluxes measured at 25°C are representative for both the catalyst operating at 25°C and 500°C.

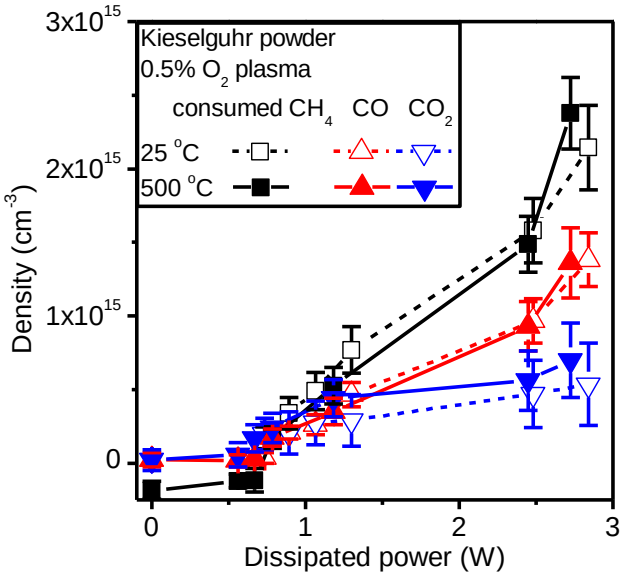

Figure 8.2: CH_4, CO and CO_2 densities as a function of plasma dissipated power with kieselguhr powder at a temperature of 25 °C and 500 °C. Reprinted with permission from ref [124] © 2021 IOP Publishing.

8.3.2 Is there a synergistic effect?

The synergistic effects in plasma catalysis can be expressed either in the form of higher conversion rates or lower activation energies. Temperature-programmed experiments were performed for the Ni catalyst to evaluate the influence of plasma on the activation energy. The temperature of the catalyst bed increased continuously from 25 °C to 500 °C with a heating rate of 10 °C/min for both plasma ON or plasma OFF conditions. Real-time CH_4 densities at the reactor outlet were recorded. The specific experimental conditions are

detailed in figure 8.3. It can be seen in Figure 8.3(a) that the conversion of CH_4 is significantly enhanced when the catalyst bed temperature exceeds the activation temperature. Also, there is a significant shift (~50 ^oC) in the activation temperature between the plasma ON and OFF cases. The Ni catalyst was activated at about 360 ^oC without the plasma, and this activation temperature was lowered to about 310 ^oC with the 1 W APPJ. The influence of the change in gas temperature induced by the plasma can be neglected because the gas temperature in the afterglow of the 1 W APPJ is close to room temperature (~310 K). The plasma involvement can help to lower the activation energy required to break the strong chemical bonding of molecules that usually require high temperatures. This result also shows that synergistic effects exist even when the plasma is not in direct contact with the catalysts. Furthermore, when comparing the CH_4 conversion at 25 ^oC for both plasma ON and OFF cases, the difference is very small (on the order of ~10^{14} cm^{-3}), indicating that the plasma-induced CH_4 conversion at 1 W is much smaller than the catalyst-induced CH_4 conversion at elevated high temperatures (500 ^oC).

Figure 8.4 shows a comparison between the plasma catalysis with the catalyst bed at 500 ^oC with the sum of the plasma and pure thermal catalytic reaction at 500 ^oC as a function of plasma dissipated power in terms of CH_4 conversion and ($CO + CO_2$) production. The results show that plasma catalysis at 500 ^oC consumes about 31% (with an uncertainty of ±10%) more CH_4 than the sum of plasma and thermal catalysis when using 3.5 W APPJs. Consistently, the sum of the products CO and CO_2 in plasma catalysis is also about 32% (with an uncertainty of ±22%) higher than the sum of the other two cases. As in the case of kieselguhr this was not observed, this increase in conversion is related to the catalyst.

Figure 8.3(b) shows the real-time recorded downstream CO and CO_2 densities during the temperature ramp. The plasma power was set at 3 W in this case to enhance the plasma-catalyst interaction resulting in more noticeable results. The CO and CO_2 curves have distinct trends. CO formation starts to decrease at about 200 ^{o}C and CO_2 formation is favored at high temperatures. A possible explanation is that CO is oxidized to CO_2 at elevated temperatures. Nevertheless, it is observed that the decrease in CO cannot compensate for the increase in CO_2, which means other reactions in addition to CO oxidization occur at catalyst surface at high temperatures.

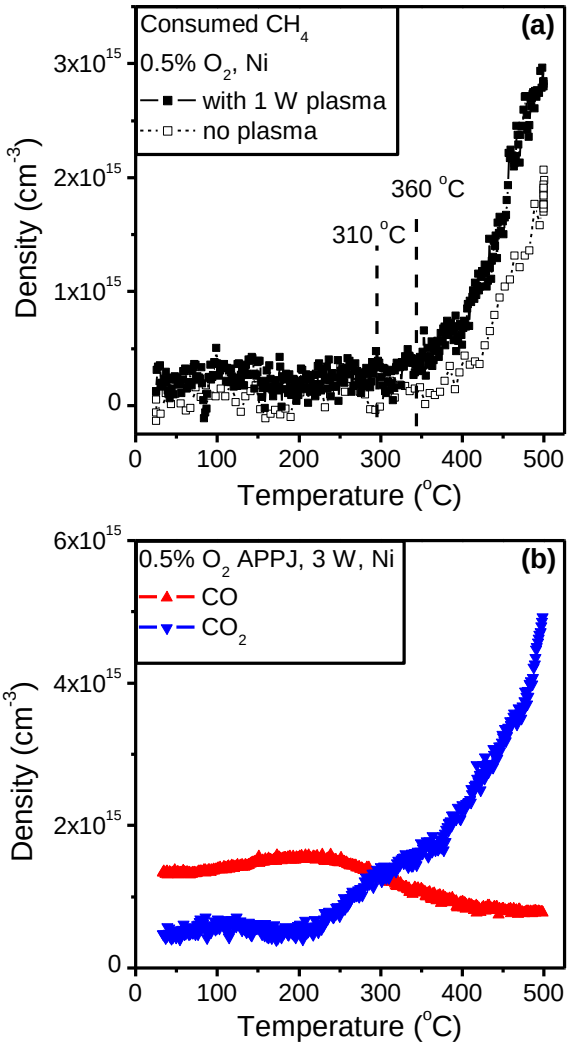

Figure 8.3: (a) CH_4 consumption as a function of the applied catalyst bed temperature with and without the 1 W Ar/O_2 plasma. (b) Downstream densities of CO and CO_2 as a function of catalyst temperature under the treatment of 3 W Ar/O_2 APPJ. Reprinted with permission from ref [124] © 2021 IOP Publishing.

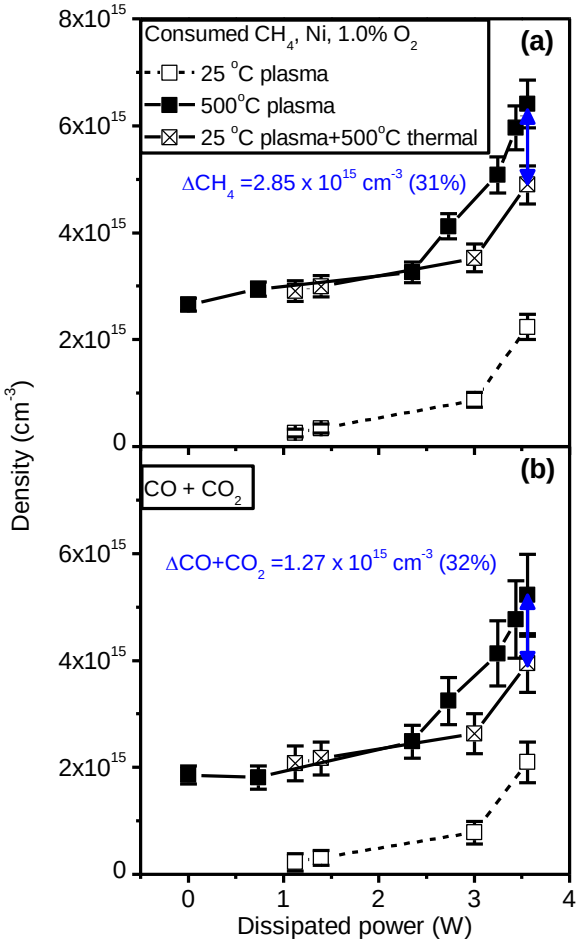

Figure 8.4: Comparison of plasma catalysis at the applied catalyst bed temperature of 500 °C with the sum of plasma and pure thermal catalytic reaction at 500 °C in terms of (a) CH_4 conversion, and (b) CO + CO_2 production as a function of plasma dissipated power. Reprinted with permission from ref [124] © 2021 IOP Publishing.

8.3.4 Importance of plasma-produced reactive species in plasma-catalyst interaction

To understand the plasma-catalyst interaction or the observed synergistic effect, the correlation between the CH_4 conversion and plasma-produced species is required. The most dominant reactive species produced in $Ar+O_2$ APPJs were previously measured to be O, $O_2(a^1\Delta_g)$ and O_3 [117]. In this section, we first study the effects of plasma power, O_2 concentration and catalyst temperature on the CH_4 conversion as well as CO and CO_2

production. Then the dominant plasma-produced species (O, $O_2(a^1\Delta_g)$ and O_3) are correlated with the conversion of CH_4 to assess the importance of each reactive species.

8.3.4.1 Effects of plasma power, O_2 concentration and catalyst temperature

In this study, the CH_4 is not fed through the ionizing plasma, and the entrainment of CH_4 into the plasma jet effluent, where reactive species able to dissociate the highly stable CH_4, enable gas-phase CH_4 dissociation. Figure 8.5 shows the consumed CH_4densities as well the produced CO and CO_2 densities as a function of plasma dissipated power at two applied catalyst bed temperatures (25 ^oC and 500 ^oC). In general, CO and CO_2 are found to account for about 90% of the CH_4 conversion, indicating that the formation of other products is less pronounced. In addition, the CH_4 conversion is less than 10%, most likely due to mixing limitations of CH_4 with the plasma effluent.

It is shown in figure 8.5 that increasing the plasma power generally enhances the CH_4 conversion and CO and CO_2 production. At 25 ^oC when the catalyst is not thermally activated, increasing the O_2 concentration decreases the CH_4 conversion rate for a fixed plasma power. This is associated with the reduction in plasma plume length with increasing O_2 concentration in the feed gas, resulting in reduced entrainment of CH_4 in the plasma effluent containing the reactive species that enable gas-phase dissociation of CH_4.

Due to the very large dissociation energy of CH_4, only a few plasma-promoted reactive species will be able to dissociate CH_4 in the gas phase at sufficiently high rates to contribute significantly to the absorbed CH_4 dissociation. These species include energetic electrons and O atoms. To assess the importance of gas-phase CH_4 dissociation in the afterglow region of the APPJ, a simple estimation was performed to evaluate the possible roles of

electrons and O atoms based on the reaction rate coefficients of the following CH_4 dissociation reactions:

$$e^- + CH_4 \rightarrow e^- + CH_3 + H,\ k_1 = f(T_e) \quad \text{(R1)}$$

$$O + CH_4 \rightarrow CH_3 + OH,\ k_2 = 2.26\times10^{-12}\ (T/298)^{2.20}\exp(-3819.84/T)\ \text{cm}^3\ \text{s}^{-1} \quad \text{(R2)}$$

The role of other dominant reactive species such as $O_2(a^1\Delta_g)$ and O_3 can be ruled out due to their low energies, although recombination of O_3 can lead to the formation of O in the plasma effluent. The threshold energy of R1 is ~10 eV according to the cross-section data from [125]. Assuming an electron temperature of 2 eV, consistent with the measurements in [85] using a similar plasma jet in the Ar+0.5% O_2 + 0.33% CH_4 gas composition, the non-Maxwellian nature of the electron energy distribution function (EEDF) significantly deplete the high energy electrons (>10 eV), and an upper limit of k_1 is estimated to be 5×10^{-14} cm^3 s^{-1} with BOLSIG$^+$ (12/2019) [126] using the PHELPS database from LXCat [127]. On the other hand, the rate coefficient of the competing reaction k_2 at 350 K (gas temperature in the jet effluent) is calculated to be 5.9×10^{-17} cm^3/s. Note that CH_4 mostly diffuses into the jet effluent instead of the active plasma region, particularly for larger O_2 concentrations with shorter plasma plume lengths. At the tip of the plasma plume, the O density is in excess of 2×10^{16} cm^{-3} and the electron density is on the order of 10^{12} cm^{-3}. This suggests the dissociation of CH_4 by O density is likely more effective than electron-induced CH_4 dissociation. This might suggest significantly different conditions compared to a DBD system where transient high electron temperatures are obtained and CH_4 dissociation has been attributed to electron-induced reactions [128]. Nevertheless, the characteristic timescale of these reactions remains slow for the investigated plasma conditions to fully explain the gas-phase conversion and other dissociation reactions

involving electronically excited state molecules, such as O(1D), cannot be excluded. Further analysis requires detailed modeling and simpler transport conditions which are out of the scope of this work.

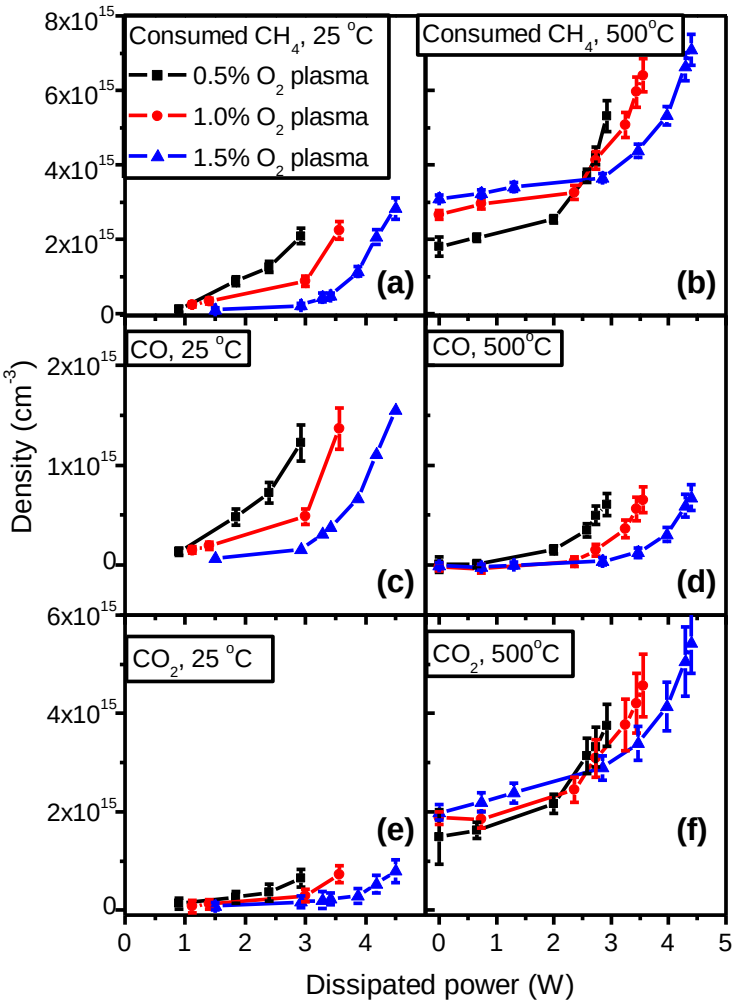

Figure 8.5: Measured densities of CO, CO_2 and CH_4 at the reactor exhaust under various plasma powers at the applied catalyst bed temperature of 25 °C or 500 °C: CH_4 consumption at 25 °C (a) and 500 °C (b), CO production at 25 °C (c) and 500 °C (d), and CO_2 production at 25 °C (e) and 500 °C (f). Reprinted with permission from ref [124] © 2021 IOP Publishing.

In addition, figure 8.5 also shows that at 500 °C when the thermal catalysis becomes active, larger O_2 can lead to higher CH_4 conversion and CO_2 production. This is consistent with

the results shown in section 8.3.2. CO production is not affected by the O_2 concentration, and it is inhibited at 500 °C compared to 25 °C due to the oxidation of CO into CO_2.

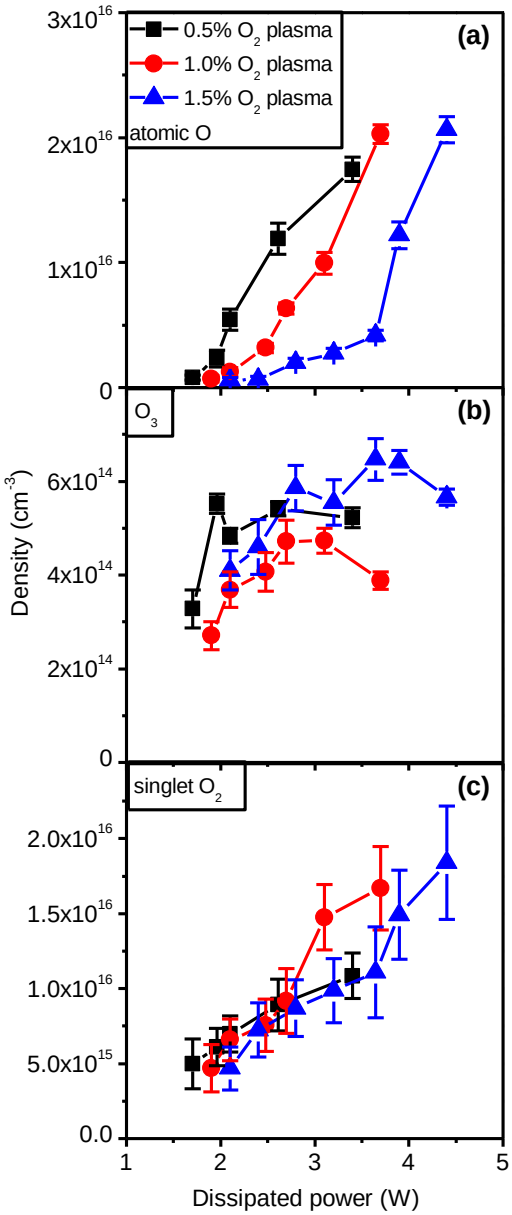

Figure 8.6: O, $O_2(a^1\Delta_g)$ and O_3 densities at a distance of 5 mm from the APPJ nozzle as a function of plasma dissipated power. Reprinted with permission from ref [124] © 2021 IOP Publishing.

8.3.4.2 Quantification of plasma-produced species

The dominant reactive species (O, $O_2(a^1\Delta_g)$ and O_3) produced by the APPJ are quantified by the MBMS system using the same conditions as the experiments in the plasma-catalyst reactor. The highest gas temperature corresponding to the highest plasma dissipated power (4.5 W) in this study was ~350 K indicated by the measurements of Ar using MBMS. This small temperature increase (~50 K) is suggested to be unlikely associated with the synergistic effects and not considered in the further analysis. Figure 8.6 presents the densities of O, $O_2(a^1\Delta_g)$ and O_3 as a function of plasma dissipated power for three different O_2 concentrations. It shows that the O density has a similar trend with the CH_4 consumption as a function of plasma dissipated power, as indicated in figure 8.5. However, O_3 and $O_2(a^1\Delta_g)$ densities only have a change of less than a factor of 3 within the investigated power range, of which the variation trends are not similar to the CH_4 conversion. Therefore, the importance of O_3 and $O_2(a^1\Delta_g)$ are unlikely the origin of in the synergistic effects, and the correlation of O and consumed CH_4 is quantified in more detail below.

8.3.4.3 Correlation between plasma-produced O and consumed CH_4 fluxes

The unit of species density (cm^{-3}) will be converted into averaged particle fluxes ($cm^{-2}\ s^{-1}$) in this section in the correlation. The averaged convective fluxes are obtained using the following relation:

$$\Gamma = n_k v = n_k \frac{Q}{A}, \tag{8.1}$$

where Γ is the average particle flux ($cm^{-2}s^{-1}$), n_k the density of species k (cm^{-3}), Q the volumetric flow rate (cm^3s^{-1}) and A the catalyst bed cross section (cm^2).

Figure 8.7 shows the correlation between O fluxes and the consumed CH_4 and produced CO and CO_2 fluxes. It is found that there exists a linear relationship between O and

consumed CH_4 as well as CO and CO_2 production. The other two species ($O_2(a^1\Delta_g)$ and O_3) do not show such a correlation. For the 25 °C cases, the curves for different O_2 concentrations almost overlap with each other. Nonetheless, for the 500 °C cases, a change in O_2 concentration impacts the convection due to the thermal catalysis enabled conversion of CH_4. The fluxes of consumed CH_4 and produced CO_2 are larger for higher O_2 concentrations.

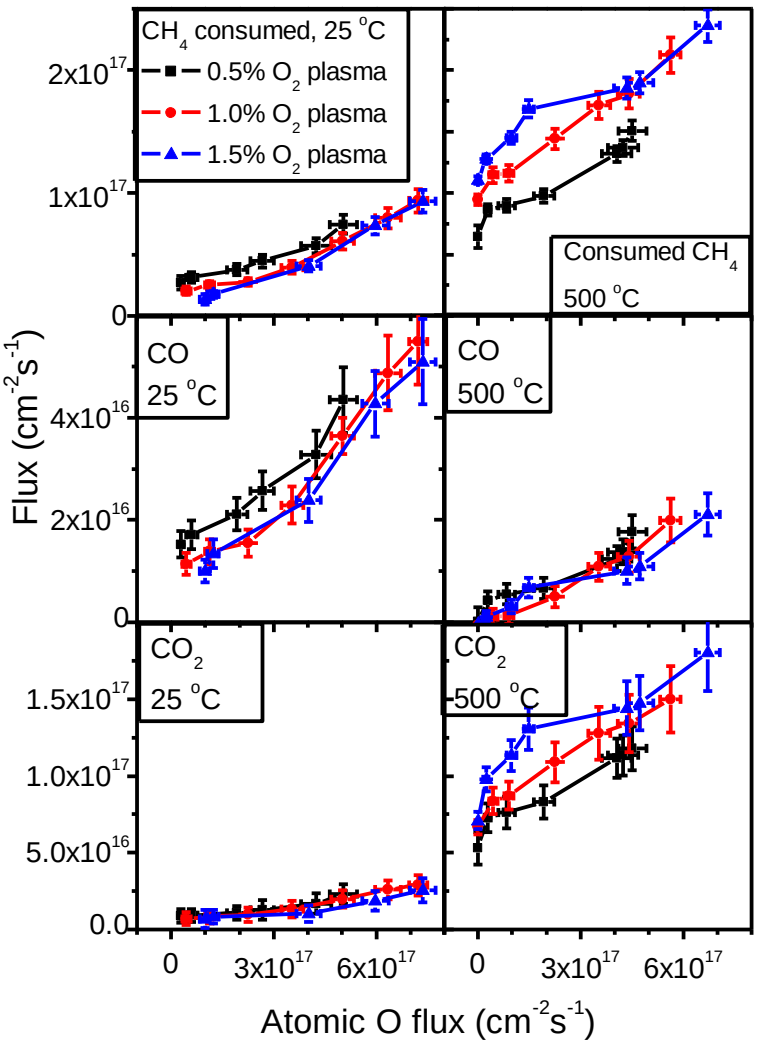

Figure 8.7: Correlation between the fluxes of consumed CH_4, produced CO and CO_2 and O at the applied catalyst bed temperature of 25 °C and 500 °C. The fluxes were calculated based on Eq. (8.1). Reprinted with permission from ref [124] © 2021 IOP Publishing.

8.3.5 Analysis of surface species and reaction mechanism

The downstream gas-phase measurements and the *in situ* DRIFTS measurements of the catalyst are compared in this section to assess the impact of the plasma on the catalyst . Figure 8.8 presents the surface CO and CH_n by DRIFTS together with the gas phase CO and CO_2 densities as a function of plasma dissipated power. The absence of surface CH_n and CO for both 25 ^oC and 500 ^oC without plasma suggests that the formation of CO_2 by thermal catalysis does not require CH_n and CO as the intermediate products. The oxidation of CH_4 into CO_2 in thermal catalysis is possibly due to the surface O from the breakdown of surface-adsorbed O_2 at active catalyst-sites, as suggested by Hu et al. [129]–[131]. At 25 ^oC, it is observed that both surface CO and CH_n increase almost linearly as a function of plasma dissipated power, indicating that plasma-produced species contribute to the formation of surface CO and CH_n. It is usually suggested in the literature that the formation of surface CH_n is caused by the adsorption of the vibrationally excited CH_4 produced by the plasma. The vibrational energy in CH_4 (v) lowers the energy barrier to dissociate C-H bond and contribute to the formation of surface CH_n. This might be applicable for the cases where plasma is in direct contact with the catalyst, but is not applicable in our study because the lifetime of CH_4(v) is on the order of ~10s μs and its densities should be rather low in the far afterglow region of APPJ when reaching the substrate in our plasma-catalyst reactor. We hypothesize postulate that the increase in surface CO and CH_n might be due to the long-lived plasma-produced species such as $O_2(a^1\Delta_g)$ and O_3. As indicated in figure 8.6 (c), $O_2(a^1\Delta_g)$ densities have a linear relationship with the plasma power. The internal energy from $O_2(a^1\Delta_g)$ might be transferred to help dissociate CH_4 when colliding with catalyst surfaces. Furthermore, the formation of surface CO might be enhanced from the oxidization of surface CH_n enabled by $O_2(a^1\Delta_g)$ or O_3. However, we cannot exclude the

possibility that it is partially due to the adsorption of plasma-produced CO on the catalyst surface.

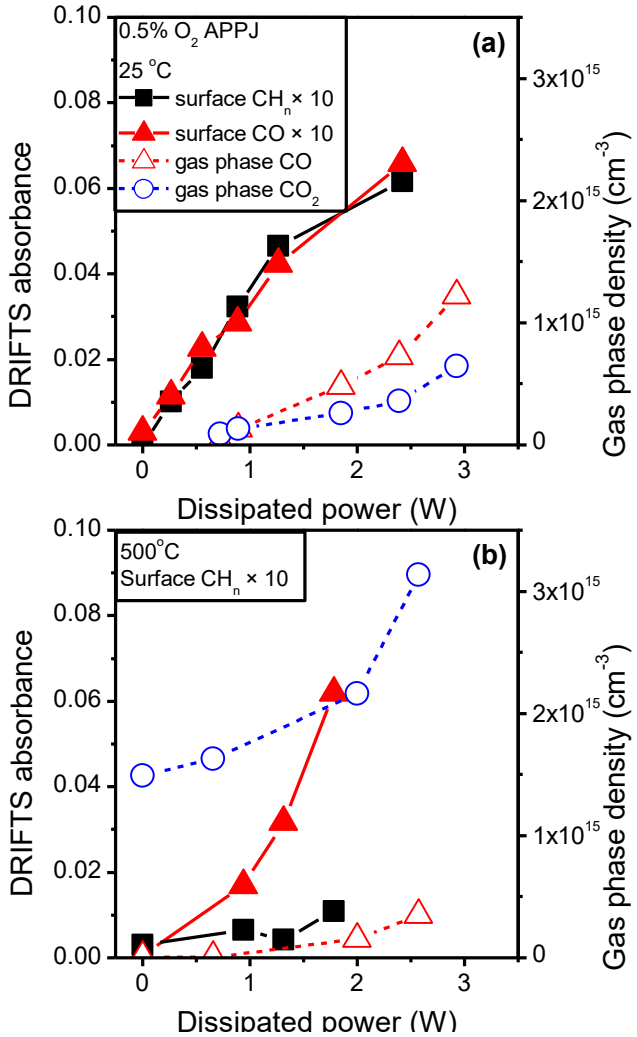

Figure 8.8: Surface CH_n and CO absorbance, and gas-phase CO and CO_2 densities as a function of plasma power at the applied catalyst bed temperature of 25 °C (a) and 500 °C (b). The absorbance of surface CO and CH_n at 25 °C and CH_n at 500 °C was multiplied by a factor of 10 for a clearer comparison. Reprinted with permission from ref [124] © 2021 IOP Publishing.

When the applied catalyst bed temperature increases to 500 °C, the trends of surface CH_n and CO significantly change compared to the 25 °C case. The relative absorbance of CH_n becomes low and its increase as a function of power is less obvious. The surface species measured by DRIFTS represent those adsorbed on the top layers of catalysts. As analyzed

before, the reactive species reaching the catalyst bed (the top layers of catalysts) should be similar for both 25 ^{o}C and 500 ^{o}C cases. Hence, it is suggested that the desorption or conversion of surface CH_n is much enhanced at 500 ^{o}C. It is also observed that there is a large amount of surface CO compared to surface CH_n. This is less likely due to the direct adsorption of gas-phase CO since its density is lower than at 25 ^{o}C and the high temperature (500 ^{o}C) is likely to enhance CO desorption. This suggests that there exists a production reaction of surface CO possibly involving surface CH_n, surface O, as well as plasma-produced species such as O. Although the surface CO densities are high at 500 ^{o}C, the formation of gas-phase CO, is inhibited which might be due to the oxidation of gas-phase CO by the surface O. Moreover, the surface CO might also react with gas-phase oxidizer O or surface O forming CO_2. This is consistent with the linear relationship between O and CO_2 observed in figure 8.7. Overall, at 500 ^{o}C, the formation of surface CH_n is suggested to be the rate-determining step of the production of CO and CO_2 in plasma catalysis.

8.4 Conclusion

An APPJ is incorporated into a catalyst reactor to study plasma catalysis in the context of partial oxidation of methane into syngas in this chapter. *In situ* plasma-produced species fluxes are correlated with the *in situ* changes of the catalytic surfaces as well as the downstream gas products to have a better understanding of the synergistic effect and reaction mechanism in plasma catalysis. At the University of Maryland, consumed CH_4, as well as produced CO and CO_2, were characterized downstream of the catalyst bed by FTIR, and the catalyst surface was analyzed by operando DRIFTS. The reactive species fluxes were characterized by MBMS under the same operating conditions at the University of Minnesota. Synergistic effects, although modest, were observed both in the form of

activation energy and CH_4 conversion. The Ni catalyst was activated at about 360 ^oC without the plasma, and this activation temperature was lowered to about 310 ^oC with the 1 W APPJ. Plasma catalysis at 500 ^oC consumes about 31% more CH_4 than the sum of plasma and thermal catalysis when using 3.5 W APPJs. In addition, the formation of gas-phase CO is inhibited at 500 ^oC. By correlating the quantified dominant plasma-produced reactive species fluxes (O, $O_2(a^1\Delta_g)$ and O_3) with the consumed CH_4 and produced CO and CO_2 fluxes, a strong correlation between atomic O flux and CH_4 conversion was identified suggesting its importance for the oxidation of CH_4 to CO and CO_2. The DRIFT measurements of surface CH_n and CO at 25 ^oC indicate that the formation of surface CH_n is mainly due to the plasma-produced species, and the change in surface species density seems to correlate with long-lived species such as $O_2(a^1\Delta_g)$ in the plasma catalysis reactor. It was also found that surface CH_n reduced at higher applied temperature (500 ^oC), suggesting that it could be efficiently converted into surface CO or other species. The formation of surface CH_n might be the rate-determining step of the production of CO and CO_2 at 500 ^oC in plasma catalysis.

Chapter 9

Investigation of mechanisms underpinning plasma-catalyst interaction for the direct conversion of methane to oxygenates

9.1 Introduction

Catalytic partial oxidation of CH_4 is a particularly interesting route for converting the abundantly available natural gas into higher energy density liquid fuels prior to transportation [132]. The conversion is triggered by the difficulties and costs associated with CH_4 transportation. Methanol (CH_3OH), one of the products of partial CH_4 oxidation, is furthermore a clean and renewable fuel source and is also in great demand as an intermediate source of green energy to provide electric energy generation via fuel cell technology applications [133].

The conventional approach to convert CH_4 into CH_3OH is a two-step catalytic process. The first step is to convert CH_4 into syngas ($CO + H_2$) at high temperature, and then the syngas is further converted to methanol or other liquid fuels at high temperature and pressures (typically 60–100 bar and 250–280 ºC) over Cu–ZnO-based catalysts. Due to the high cost of this high temperature and pressure process, alternative energy-efficient technologies to directly convert CH_4 into CH_3OH or other oxygenates are being developed based on the partial oxidation of methane.

$$CH_4 + \tfrac{1}{2} O_2 \rightarrow CH_3OH,\ \Delta H^0_{298K} = -126.2 \text{ kJ mol}^{-1} \qquad \text{(R1)}$$

Although significant efforts have been devoted to the investigation of direct conversion of methane to oxygenates via thermal catalysis, the reported product yields in terms of CH_3OH to date are insufficient to replace the conventional two-step process [134]. Plasma-catalysis has been proposed as one of the innovative approaches to further enhance direct methane to methanol conversion since the synergistic effect between plasma and thermal

catalysts were reported potentially enabling chemical conversion at lower temperatures and pressures as in conventional thermal catalytic processes [23].

Nozaki and Okazaki [135] experimentally and theoretically analyzed the energy efficiency of non-oxidative methane conversion using a dielectric barrier discharge (DBD), and the result indicated that DBD alone was less efficient. The authors also proposed a DBD-catalysts hybrid reactor and a synergistic effect was observed between reactive species produced by plasma and catalysts, suggesting that vibrationally excited species were crucial for enhancing the CH_4 conversion efficiency. Kim et al. [136] performed a detailed kinetic study of CH_4 activation in a DBD to quantify plasma-catalyst interactions via kinetic parameters. The results showed that the thermal catalysis had a typical Arrhenius behavior with an activation energy of ~73.5 kJ mol^{-1}, but the plasma catalysis exhibited non-Arrhenius behavior suggesting to be due to the interaction between plasma and catalysts. In addition, the reported energy barrier for plasma catalysis was found to be much lower than the activation energy needed in thermal catalysis. Another publication by Kim et al. [137] reported on the dry reforming of CH_4 with CO_2 using Ni/Al_2O_3 catalysts, and provided evidence that plasma-catalyst interaction indeed existed and was able to significantly enhance the activation of C-H bonds when the temperature >630 K. The comparison between the CH_4 conversions of thermal catalysis and plasma catalysis indicated a ~50 K shift in the activation energy. Such a small shift could be easily caused by localized plasma-induced gas heating. In addition to these synergistic effects, the use of non-thermal plasmas for catalyst regeneration was also reported [138]. The active species produced by the plasma can oxidize the coke formed on the catalyst and regenerate the

catalyst at room temperature (293 K), requiring potentially lower energy than the common thermal regeneration that takes place at ~800 K.

Recently, Chawdhury et al. [34] investigated the plasma-catalytic partial oxidation of methane into oxygenates in a dielectric barrier discharge (DBD) reactor at room temperature. Three different supported transition metal catalysts (N_i/γ-Al_2O_3, Cu/γ-Al_2O_3, and Fe/γ-Al_2O_3) were tested, and the result showed that Fe/γ-Al_2O_3 provided the highest methanol selectivity of 36% and a significant methanol yield of 4.7%. The authors postulated the possible reaction routes for the CH_3OH production on the catalyst surfaces, and CH_x species were suggested to be critical for CH_3OH production. De Bie et al. [139] established a one-dimensional fluid model for a DBD reactor in the context of the conversion of methane into oxygenates. The main underlying reaction pathways forming syngas, methanol and other oxygenates were determined for both partial oxidation and dry reforming of methane. Yi et al. [33] investigated the selective oxidation of CH_4 to CH_3OH over Ni-based catalysts at low temperature and atmospheric pressure and achieved 81% oxygenates selectivity and 50 % CH_3OH selectivity. This work also reported kinetic modelling results indicating that, in the plasma, CH_3OH was mainly produced through radical reactions starting from $CH_4 + O(^1D) \rightarrow CH_3O + H$, followed by $CH_3O + H + M \rightarrow CH_3OH + M$ and $CH_3O + HCO \rightarrow CH_3OH + CO$. In addition, the production of CH_3OH was attributed to chemisorbed oxygen species that could react with the plasma-produced gas-phase CH_3 radicals to form surface species CH_3O_{ad}. The authors also hypothesized that H_2O molecules produced by the plasma might be activated by the NiO/γ-Al_2O_3 catalyst and then further promote the desorption of CH_3OH from the catalyst surfaces, according to the findings from [140].

Although researchers have successfully increased CH_3OH yields enabled by plasma catalysis by adjusting the composition of catalysts and plasma conditions, such findings are enabled by trial-and-error large scale parametric studies and our understanding of the underpinning process remains limited. This hampers further improvements in energy efficiencies, selectivity and yield for CH_3OH conversion applications. Inspired by the work of Chawdhury et al. [34], in this chapter, we implemented, similar as in Chapter 8 a detailed study of plasma-produced species and conversion yields to investigate the plasma-catalyst interaction in the context of direct conversion of methane to oxygenates at room temperature. The products and plasma-produced species with or without catalysts were both quantified using molecular beam mass spectrometry (MBMS). Plasma-produced reactive species reaching the catalysts were correlated with the products downstream of the catalyst reactor to assess their importance in the plasma-catalyst interaction.

9.2 Experimental setups

9.2.1 Plasma jet and catalyst reactor

In this work, we coupled an atmospheric pressure plasma jet with a catalytic reactor downstream enabling the separation of the active plasma region and catalyst, as shown in figure 9.1. This configuration also allowed us to measure the species densities both at the entrance and exit of the catalytic reactor, as the catalyst reactor can be detached from the plasma jet. We used three different combinations of the plasma jet and the catalyst reactor, as shown in figure 9.1. These configurations allow for distinguishing effects of short-lived species and long-lived species by investigating two distances from the plasma jet electrode to the catalysis reactor (5 mm and 33 mm).

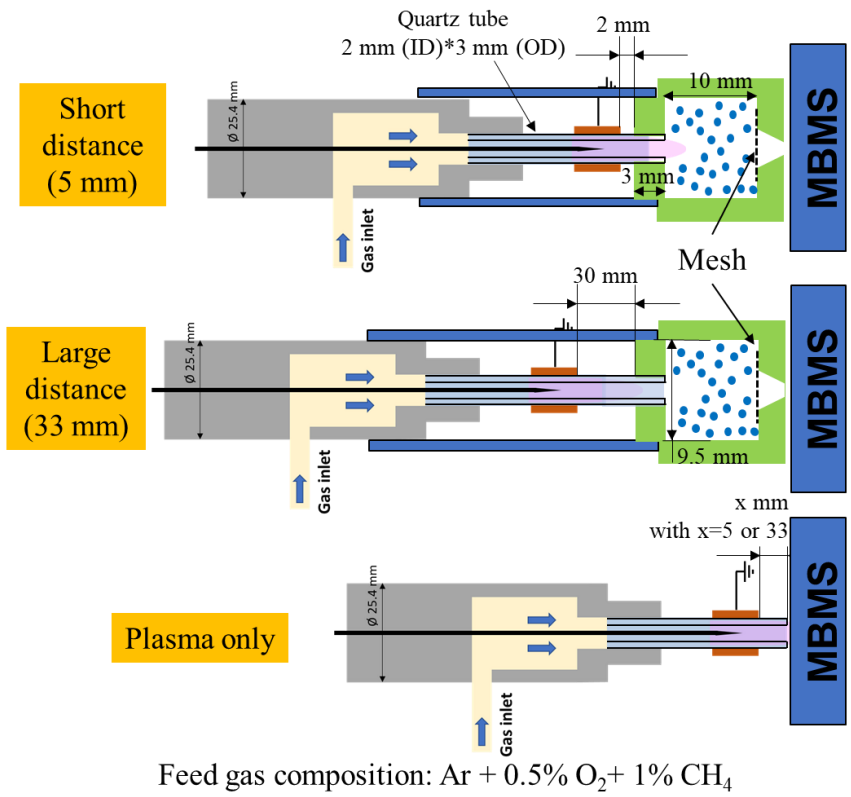

Figure 9.1: Schematic of the different configurations of the flow-through plasma-catalysis reactor used in this study.

The plasma jet used in this chapter is identical to the one used in chapter 8. The plasma jet was driven by a radiofrequency voltage waveform modulated by a 20 kHz modulation with a 20% duty cycle. The main difference with the work in chapter 8 is that CH_4 is added into the feed gas instead of being mixed downstream in the plasma effluent. The composition of the feed gas was fixed at Ar + 1% CH_4 + 0.5% O_2 for all the results in this study. The Ar flow rates were kept constant at 200 sccm in this study unless otherwise stated. Higher CH_4/O_2 ratios as used in [34] were also attempted in the preliminary experiments but resulted in carbon deposition or gas-phase carbon particle formation, which was not further pursued to avoid blocking of the sampling orifice of the MBMS. A 200 mesh was implemented at the outlet of the catalyst reactor to prevent the catalyst particles from being

blown out and similarly blocking the sampling orifice of the MBMS. The operation of the plasma jet and the plasma dissipated power calculation are described in detail elsewhere [141]. The gas temperature measurements in this study were performed with a K-type thermal couple and a temperature strip (OMEGA, RLC) with a temperature resolution of 5 K.

9.2.2 Catalyst information and preparation

Microsphere catalysts (20% wt% Fe/γ-Al_2O_3) and the control group γ-Al_2O_3 particles from Riogen, Inc. were used in this study. All the particles have the same size (~375 μm), and the entire catalytic reactor was loaded loosely without compressing the catalyst to ensure a low flow resistance. The weights of the loaded Fe/γ-Al_2O_3 and Al_2O_3 particles were 0.53 g and 0.39 g, respectively. The pretreatment consisted of an Ar+4% H_2 plasma treatment at atmospheric pressure for about 2 hours after the catalyst reactor was installed in the reactor.

9.2.3 Molecular beam mass spectrometry (MBMS)

MBMS was used to quantify the reactive species produced by the plasma as well as the downstream products of the catalyst reactor. The details of the MBMS system used can be found in Chapter 1 and 2. The species measured in this chapter includes the reactants (CH_4 and O_2), main products (CO, CO_2, H_2), minor products (oxygenates) and the short-lived species CH_3. While attempted, we were unable to measure atomic oxygen and hydrogen radicals. Table 9.1 provides a summary of the electron energy and calibration gas used for each species in MBMS measurements.

Table 9.1: Summary of electron energies and calibration gases for each species by MBMS.

Species name	Tracked species mass m/z (amu)	MBMS electron energy (eV)	MBMS calibrated gas	Ref. (method, σ_{EII})
CH_3/CH_3O_2	15	12.5	CH_4	[142]–[145]
CH_3OH or C_2H_5OH	31	70	O_2	[143],[146]
C_2H_6 or CH_2O	30	70	N_2	[143]
C_2H_5OH or HCOOH	46	70	None	[143],[147]
CH_3COCH_3	58	70	None	[148]
CH_3COOH	60	70	None	[149]
CO	28	70	N_2	[143]
CO_2	44	70	CO_2	
H_2	2	70	H_2	
O_2	32	70	O_2	
CH_4	15	70	CH_4	

The measurements of stable species including CO, CO_2, H_2, O_2, and CH_4 have been performed using electron energy of 70 eV. Their absolute calibrations are also straightforward because they can be achieved with known concentrations of these gases. For the short-lived reactive species, threshold ionization mass spectrometry (TIMS) is used to exclude the contribution from their parent molecules. An additional 50 Hz RF plasma modulation is implemented on top of the 20 kHz RF modulation to enable the accurate subtraction of the background signals. Details regarding the TIMS and the rationale and implementation of the background subtraction approach can be found in Chapter 2. We were only able to measure a radical signal at 15 amu, however, a detailed analysis in the result section suggests that this cannot be due to the methyl radical as initially expected but most likely to CH_3O_2 (see further).

The possible oxygenates produced in this work include methanol (CH_3OH), ethanol (C_2H_5OH), formaldehyde (CH_2O), formic acid (HCOOH), acetic acid (CH_3COCH_3), and acetone (CH_3COCH_3). Due to the possible existence of other hydrocarbons with the same masses such as C_2H_6 and the complex cracking pattern of these oxygenates in the mass spectrum, further analysis of the MBMS results is required. According to the mass spectrum of oxygenates and relative hydrocarbons, the masses (m/z=60 amu and m/z=58 amu) can represent formic acid and acetic acid, respectively. The mass (m/z=46 amu) is a combination of ethanol and formic acid, and the mass (m/z=30 amu) approximately represents C_2H_6 or CH_2O.

As for CH_3OH with a mass of 32 amu, we tracked the fragment (m/z=31 amu) which is the highest signal at 70 eV in CH_3OH mass spectrum, which could help to exclude the contribution from the abundant O_2 molecules having the same mass as methanol. Nevertheless, ethanol (C_2H_5OH) might also contribute significantly to the mass (m/z=31), but this fragment is less abundant (<1%) for other oxygenates at 70 eV. Hence the measured species with mass of 31 should be in principle linked to and represent CH_3OH or C_2H_5OH. The partial cross-sections of CH_3O^+ from CH_3OH and C_2H_5OH at 70 eV are 1.5×10^{-16} cm^{-3} and 2.5×10^{-16} cm^{-3}, respectively [146]. Nevertheless, both previously reported experimental [34] and modelling results [139] on CH_4-O_2 plasma catalysis indicate that the yield of CH_3OH is more than one order of magnitude higher than that of C_2H_5OH. Therefore, we referred to the measured species with the mass of 31 amu as CH_3OH in the remaining parts of this chapter.

In this work, the percentage conversion of CH_4 and O_2 are calculated as:

$$CH_4/O_2 \text{ conversion } (\%) = \frac{\text{Converted } CH_4/O_2 \text{ molecules}}{\text{Total } CH_4/O_2 \text{ molecules input}} \times 100. \quad (9.1)$$

The conversion/production rates of species are calculated as:

$$\text{Conversion/production rate } (s^{-1}) = n_i \cdot \Phi, \quad (9.2)$$

where n_i represents the measured species density of species i, and Φ the volumetric gas flow rate.

9.3 Results and discussion

9.3.1 CH_4 and O_2 conversion by plasma and product identification

In this section, a general overview of the CH_4 and O_2 conversion as well as the main products for the plasma without catalyst are provided as a baseline. Figure 9.2 (a) shows the CH_4 and O_2 conversion as a function of plasma dissipated power due to the plasma treatment. The influence of gas temperature is minimized by performing the measurements with an extended quartz tube (30 mm) which keeps the gas temperature near room temperature (below 340 K) at the nozzle. As both CH_4 and O_2 are flowing through the ionizing plasma region, CH_4 and O_2 conversions up to 30% and 50% respectively are already produced by the plasma in the investigated power range.

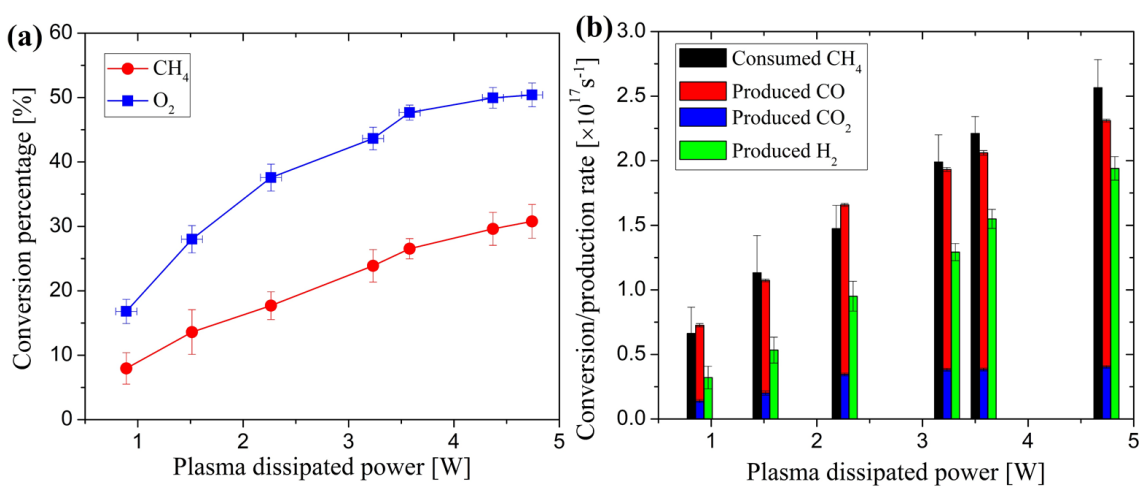

Figure 9.2: (a) CH_4 and O_2 conversions as a function of plasma dissipated power for the 'plasma only' case; (b) conversion/production rates of consumed CH_4 and produced CO and CO_2.

The results show that the conversion percentages of both CH_4 and O_2 increase with increasing plasma dissipated power. Figure 9.2 (b) compares the conversion rate of CH_4 with the production rate of CO and CO_2, the most dominant carbon-containing products. Comparing the combined CO and CO_2 production with the CH_4 conversion indicates that more than 90% of the CH_4 eventually converts into CO and CO_2, with CO accounting for about ~80% of the CH_4 conversion. This means that the selectivity of hydrocarbon to oxygenate conversion by the RF plasma jet is below ~10% and seems to be favored for higher plasma powers.

To quantify the up to 10% oxygenates produced by the plasma, measurements of methanol/ethanol (CH_3OH/ C_2H_5OH), formaldehyde (CH_2O), formic acid (HCOOH), acetic acid (CH_3COOH) and acetone (CH_3COCH_3) were performed with the MBMS. Figure 9.3(a) shows time-resolved measurements of the mass corresponding to several oxygenates with an electron energy of 70 eV. The partial cross-sections of these measured fragments from oxygenates are all within a factor of 2 and on the order of 10^{-16} cm^2 [146]–[149]. Nonetheless, smaller molecules would have larger losses during the supersonic expansion and molecular beam [101] than heavier molecules although their ionization cross-sections are generally smaller as well which will compensate to some extent for this difference. Hence, the relative mass spectrometry signals can in good approximation (within approximately a factor 2) represent the concentration of each oxygenate. The concentration is proportional to the 'plasma on' MS signal subtracted with the 'plasma off' signal.

Figure 9.3(b) shows that methanol (m/z=31) has the largest signal (difference between plasma ON and OFF) compared to the other measured oxygenates. Both CH_3COOH and CH_3COOH are approaching the detection limits hence their densities are negligible. To further evaluate the contribution from C_2H_5OH to the measured signals (m/z=31), we also measured the signals at m/z=45 and m/z=46 since C_2H_5OH and HCOOH have the same mass (46 amu). At an electron energy of 70 eV, the ratios of fragments at m/z=45 and m/z=46 for C_2H_5OH and HCOOH are about 2.5 and 0.8, respectively. Based on this fragment ratio (~2.0 in our experiments), a rough estimation of the density ratio of C_2H_5OH and HCOOH can be obtained, which is about 7:3. Furthermore, with this density ratio of C_2H_5OH and HCOOH, the contribution from C_2H_5OH to the signal at m/z=31 can be estimated, which is about 30%. In addition, the signals at m/z=30 are about 70% of that at m/z=31, which might be interpreted as formaldehyde (CH_2O) or C_2H_6 but is not distinguishable. The experimental results from [34] indicated that the CH_2O density might be comparable to that of C_2H_6.

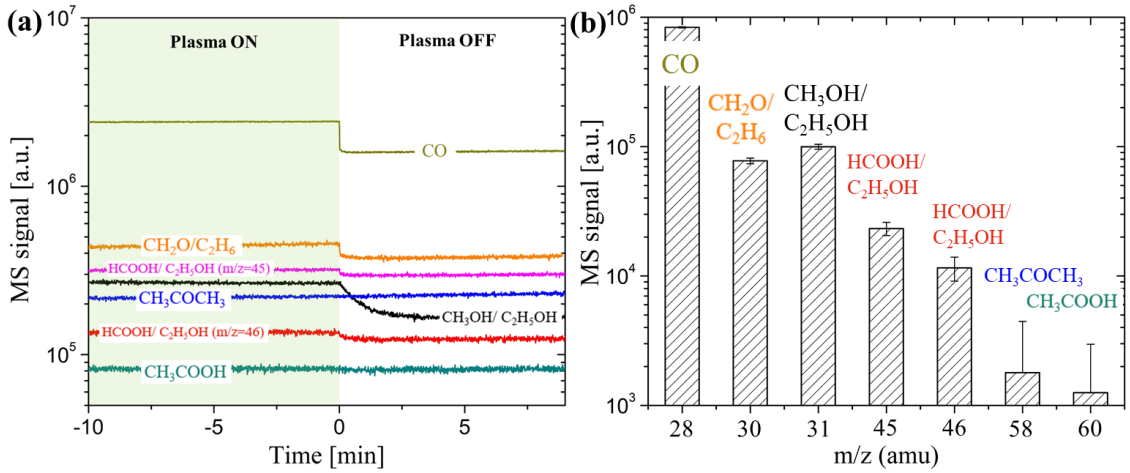

Figure 9.3: (a) Time-resolved mass spectrometry signals for CO and different oxygenates; (b) comparison of mass spectrometry signals (the difference between plasma ON and plasma OFF) for CO and different oxygenates. The plasma power was 4.7 W and the distance between the electrode and the nozzle was 5 mm.

The above comparison clearly shows that CH_3OH is the most dominant oxygenate produced by the plasma. Therefore, we chose to focus further on CH_3OH for the investigation of oxygenates in this study.

9.3.2 Comparison of plasma with and without catalyst

The observed synergy in plasma catalysis is recently becoming more and more attributed to radicals [33],[150] often based on indirect observations. To assess the role of short-lived species in plasma-catalyst interactions, we investigated in this study the two cases in figure 9.2 which enabled to study plasma-catalyst interactions for a distance of 5 and 33 mm between the active plasma region with the catalyst reactor.

As the plasma length of the maximum power is less than 5 mm, the case of 33 mm has a significant separation of the plasma and catalyst particles. Given that for the reference flow rate of 200 sccm, this distance corresponds to a gas residence time of 10s ms allowing for the recombination of most if not all short-lived radicals before they reach the catalyst reactor, and only the long-lived reactive species can reach the catalysts. In the case of 5 mm, the catalyst and the plasma remain separated (no direct coupling) but when the plasma power is increased the tip of the plasma plume can reach the entrance of the catalyst reactor. This might enable more complex interaction between the plasma and the catalyst, and a fraction of the plasma-produced radicals will reach the catalyst particles before recombining.

9.3.2.1 CH_4 and O_2 conversion

Figure 9.4 compares the CH_4 and O_2 conversion as a function of plasma power with catalyst particles or with alumina particles to evaluate potential synergistic effects. Nonetheless, the CH_4 conversion rates are identical within the experimental uncertainty (~5×10^{15} cm^{-3})

for the four cases showing that the addition of a catalyst does not enhance the CH_4 conversion for the investigated conditions. On the other hand, a significant enhancement of the O_2 conversion was observed at higher plasma power for the 5 mm case where radicals can reach the catalyst (see further). Considering that the enhancement in CH_4 conversion is negligible, it suggests an increase in oxygen-containing products, possible oxygenates or CO_2 (compared to CO). While O radicals cannot be measured by MBMS in the presence of CH_4, the higher conversion in O_2 suggests an increase in O radicals (the dominant radical in this RF plasma in the presence of O_2 [102]) up to ~2×10^{16} cm^{-3}.

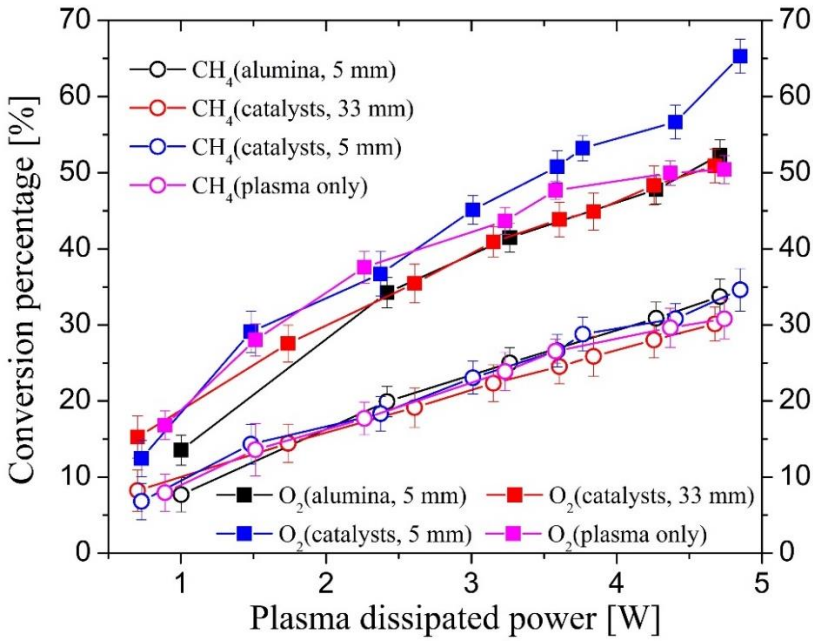

Figure 9.4: Comparison of CH_4 and O_2 conversion as a function of plasma dissipated power for plasma only and plasma-catalysts at a distance of 5 and 33 mm. A case where the catalyst was replaced with alumina pellets at a distance of 5 mm was also included as a reference.

9.3.2.2 Products

Figures 9.5 (a)-(d) show the densities of the dominant conversion products (H_2, CO, CO_2 and CH_3OH) as a function of plasma dissipated power for the same experimental conditions

as the CH_4 and O_2 conversion shown in Figure 9.4. The catalyst does not impact the H_2 and CO production significantly. Nonetheless, a significant increase in CO_2 production is observed for the 5 mm case with catalysts compared to the other cases. This increase in CO_2 density of ~0.7×10^{16} cm^{-3} correlates with the observed increase in O_2 conversion at higher plasma power as shown in Figure 9.4. As the increase is not found for alumina pellets without catalyst, the increase of CO_2 is enabled by catalytic reactions, as discussed in detail Chapter 8. However, the increase in CO_2 is less than half of the O_2 conversion increase and changes in oxygenates are anticipated as well.

Figure 9.5(d) shows the methanol/ethanol production which interestingly, shows two obvious different trends for low and high plasma powers. The following sections mostly focus on the explanation of these two changes. The 'plasma only' case can be regarded as a reference and does not show a strong dependence on the plasma dissipated power. Although at larger plasma powers, the CH_3OH density decreases likely due to the dissociation of the formed CH_3OH in the ionizing plasma.

At a small plasma power (1-2.5 W), the addition of catalyst and alumina particles leads to a remarkable reduction in the measured CH_3OH density. However, this effect is caused by the fact that it takes up to 3-4 hours for the system to reach a steady state. We confirmed this influence in the case of alumina in detail and showed that once the system is in steady-state the system yields, within the experimental accuracy, the same amount of CH_3OH as the 'plasma only' case. It was further confirmed that at larger plasma powers the system reaches a steady state on a timescale of 10s of minutes and this effect does not have an impact on the reported measurements. The increase found for the 5 mm case with catalyst suggests a plasma-catalyst synergy which is analyzed in more detail below but first we

assess why the times to reach a steady state in the CH_3OH production are so different for different plasma powers in the next section.

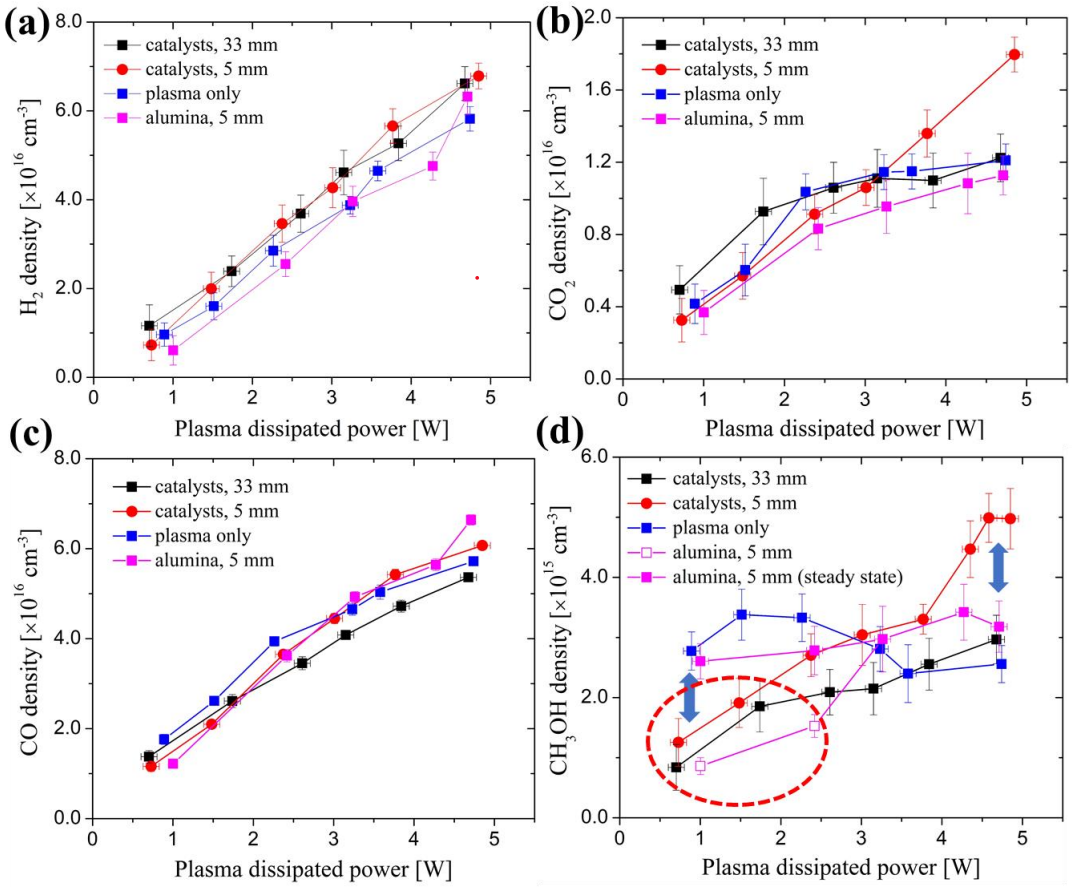

Figure 9.5: Product densities as a function of plasma dissipated power for identical experimental conditions as reported in Figure 9.4: (a) H_2 density (b) CO density (c) CO_2 density (d) CH_3OH density. The data encircled in figure 9.5. d is impacted by non-steady state effects and the blue arrow indicates plasma-catalyst synergy.

9.4 Absorption of methanol on catalyst substrate

A decay time of minutes up to hours was observed when measuring the mass spectrometry signal of methanol after switching off the plasma with continued gas feed both for catalysts and alumina particles. Examples of mass spectrometer signals detected as a function of time after switching off the plasma are shown in figure 9.6. Figure 9.3(a) shows that this minutes-long decay is found for CH_3OH but not for CO. The 'plasma only' case in Figure

9.6 shows that once the plasma is switched off, the production of CH_3OH stops and the MS signals decrease on a timescale of a few milliseconds. However, in the presence of catalyst and alumina particles, the MS signal decrease on a time scale of minutes to hours, orders of magnitude larger than the gas residence time in the system, suggesting another source of CH_3OH is present after switching off the plasma.

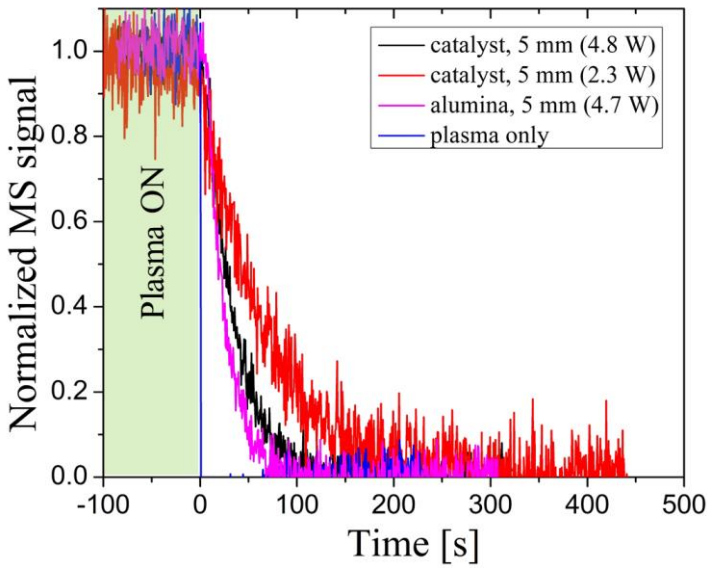

Figure 9.6: Time-resolved MS signal at 31 amu attributed to methanol after switching off the plasma at t=0.

This additional source of methanol can be due to the plasma-activated catalyst that is able to activate CH_4 in the gas stream at room temperature or due to desorption of previously adsorbed CH_3OH. The first hypothesis is less likely because this phenomenon is observed for alumina particles which cannot serve as catalysts nor be activated by plasma. The second explanation, due to the desorption of previously adsorbed CH_3OH, is further supported by several publications reporting the possibility of CH_3OH absorption on catalysts or Al_2O_3 support [151]–[153]. Therefore, we can safely assume that the various decay times for different conditions are due to adsorption. In addition, the comparison

between the decay curves for catalysts and alumina under a similar plasma dissipated power (4.7-4.8 W) in Figure 9.6 suggests that it takes a shorter time for the alumina particles to remove the absorbed CH_3OH molecules than the catalyst case under such a condition.

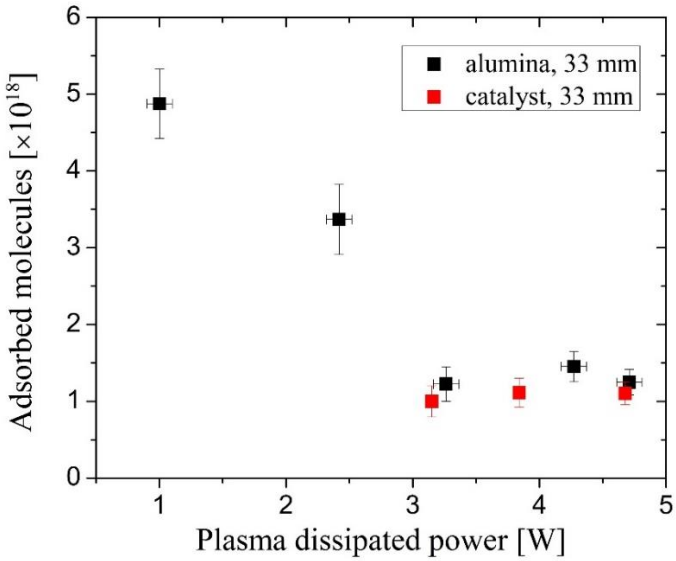

Figure 9.7: Amount of absorbed methanol molecules on the catalyst and alumina particles' surfaces as a function of plasma dissipated power for a distance of 33 mm.

The area under the decay curve in Figure 9.6. is the total amount of CH_3OH molecules absorbed on the particles at the time when the plasma is switching off. Figure 9.7 shows this total amount of absorbed molecules on the particle surface at a steady state as a function of plasma dissipated power. The amount of absorbed molecules at small plasma powers (~1 W) is about 5 times larger than the higher plasma power (> 3 W) which is indeed inconsistent with the view that plasma-activation of the catalyst would significantly contribute to this effect as higher plasma power should lead to a stronger activation of the catalyst. The 5 times larger amount of surface molecules for low plasma powers might further contribute to the longer time it takes to reach a steady state. Figure 9.7 also shows

that the absorption abilities of catalysts and alumina particles are very similar which might suggest the important contribution of the alumina substrate.

The observed change in the absorption ability of particles might be due to the change in gas temperature or plasma-produced reactive species as both scales with the plasma dissipated power. Considering that the absorption ability is also significantly impacted for the plasma at 33 mm from the catalytic reaction (see figure 9.7), it is unlikely that radicals play a dominant role in this effect and hence it must be due to long-lived reactive species or gas heating.

The gas temperatures at the nozzle (corresponding to the entrance of the catalytic reactor) are shown for an electrode-nozzle distance of 2 and 30 mm as a function of plasma dissipated power in figure 9.8. While the gas temperature increases significantly for the 2 mm distance the variation in surface coverage for the 33 mm case, if due to temperature variations must be caused by a mere change in gas temperature of 30 K.

Figure 9.9 shows the evolution of methanol signals after the Ar-CH_4-O_2 plasma is switched off for different sequential plasma exposures to evaluate the influence of gas temperature and plasma-produced species on the desorption. All three cases shown in Figure 9.9 have the same initial conditions, that is, the number of absorbed methanol molecules on the particle surface is the same. Note that the area under the curves is also the same within the experimental accuracy and hence no new sources of methanol are introduced by introducing the additional post plasma treatments.

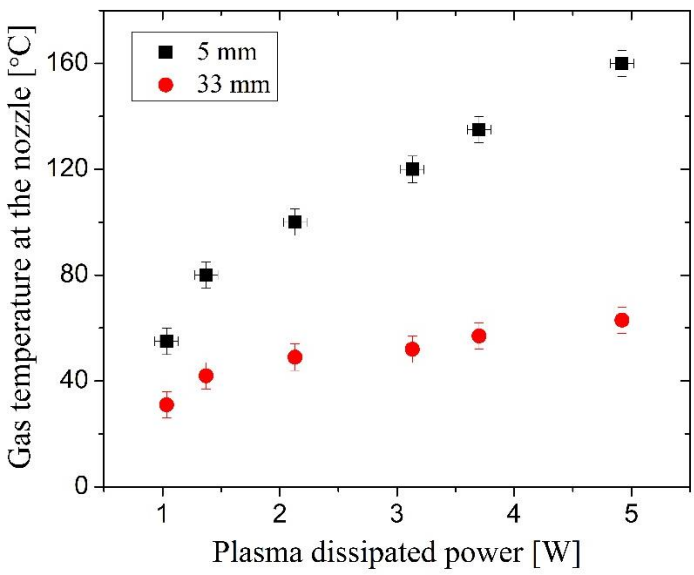

Figure 9.8: Gas temperature as measured at the nozzle with a thermocouple as a function of plasma dissipated power for an electrode to nozzle distance of 5 and 33 mm.

The initial rate of reduction in the MS signal corresponding to the mass of methanol while exposed to heated Ar gas of 65 ºC is 3 times faster than the case of Ar-CH_4-O_2 gas only at room temperature. The time constants of the three curves corresponding to Ar plasma (65 ºC), Ar + O_2 plasma (30 ºC) and no plasma (25 ºC) are 19.6 min, 10.2 min and 6.5 min, respectively. As the MS measures the desorbed methanol and the net desorption rate will be fixed at a given temperature, the slopes of the MS signal are a measure of the surface coverage and hence the time constant (inverse of the initial slope) yields a measure of the methanol desorption time. As the argon plasma does not produce reactive species with a lifetime exceeding or similar to the gas residence time, it can be concluded that gas heating of 30 – 40 K is able to significantly impact methanol desorption. This is further confirmed by the comparison with exposure of the catalyst to a low temperature Ar + O_2 plasma (Figure 9.9) operating at 30 ºC which has a significantly smaller impact on the methanol desorption than the heated Ar case. This suggests that small temperature variations are

more dominantly contributing to the desorption of methanol than long-lived plasma-produced species such as O_3 or $O_2(a^1\Delta_g)$. These results further suggest that small plasma-induced gas temperature increases of several 10s of K (and corresponding surface temperature increase of the catalyst and substrate) can significantly impact species desorption and hence potentially impact conversion rates in plasma catalysis.

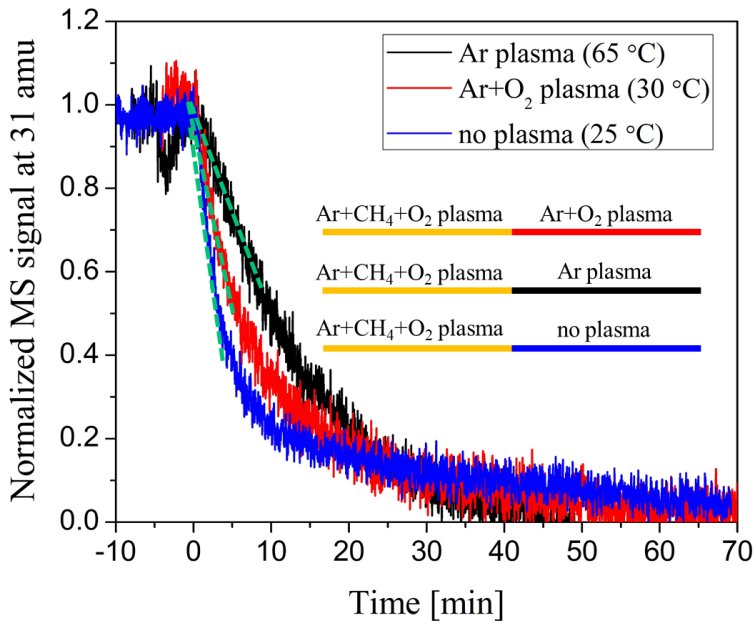

Figure 9.9: Time-resolved MS signal at 31 amu attributed to methanol after switching off the Ar-CH_4-O_2 plasma at t=0s for different post plasma exposure conditions: Ar plasma, Ar + CH_4 +O_2 and Ar+O_2 plasma yielding a gas temperature at the entrance of the catalytic reactor of 65 ºC, 25 ºC and 30 ºC respectively. The time constant corresponding to the initial slopes of the curves is also indicated.

9.5 Correlation between plasma-produced reactive species and methanol production

In the previous section, we showed that the impact of plasma-catalyst combination can impact desorption rates and CH_3OH yields at low power plasma. Importantly, this effect was shown not to significantly methanol yields produced by high power plasmas and we

will now analyze the synergistic enhancement in methanol production as reported in figure 9.5(d), at high plasma powers in more detail in this section. The largest increase in methanol production found for the investigated conditions in this study is 60% compared to the 'plasma only' case. This corresponds to an increase of the absolute density of methanol of ~2×10^{15} cm^{-3}. While this synergistic effect is moderate and insufficient to be valuable from an application perspective, the controlled decoupled plasma-catalysis experiments in this study provide an excellent opportunity to contribute to a more detailed understanding of the observed synergistic effect in plasma catalysis applications based on detailed experiments.

We measured the reactive species by MBMS implementing another 50 Hz modulation onto the plasma to enable the subtraction of the background [113]. While several radicals were probed, we were only able to measure a radical species at a mass of 15 amu corresponding to the mass of CH_3^+. Figure 9.10 (a) presents a time-resolved measurement of CH_3^+ with the electron energy of the ionizer of 12.5 eV at a plasma power of 5 W for an electrode to nozzle distance of 2 mm. Significant differences can be found between the 'plasma on' and 'plasma off' periods, indicating the existence of a radical species. The electron energy of 12.5 eV was chosen to be sufficiently above the ionization energy of the CH_3 radical (9.8 eV) and low enough to avoid the contribution of CH_3^+ formed by dissociative ionization of CH_4 molecules which requires an electron energy of 14.0 eV [154]. In addition, the contributions of CH_3^+ from other stable products like CH_3OH can be excluded as the measured signal dramatically dropped down below the detection limit when increasing the distance between the plasma to the detection orifice by only 1 mm.

Assuming the measured species is CH_3, an absolute calibration with CH_4, resulting in an absolute density of the order of ~10^{14} cm^{-3}. This seems however inconsistent with the kinetics of CH_3 and the CH_3 lifetime. The production reactions of CH_3 in the plasma afterglow was previously shown to be negligible compared to the destruction reactions [139] and the lifetime of CH_3 in the afterglow region can be estimated according to the dominant destruction reaction [139]

$$CH_3 + O_2 + M \rightarrow CH_3O_2 + M,\ k_1=9.79\times10^{-31}\ cm^6\ s^{-1}. \qquad (R2)$$

Assuming the gas temperature is 400 K and the O_2 density is depleted by 50% in the plasma, yields a lifetime of CH_3 of ~1 µs. This lifetime is significantly smaller than the time needed to transition the suction region of the mass spectrometer (~18 µs) [113] and hence the CH_3 density should drop below the MBMS detection limit before entering the molecular beam. This suggests that the measured MS signal at 15 amu is due to a reactive species with a lifetime between 10 µs to 1 ms (gas residence time corresponding to a gas plug of 1 mm in the reactor). We can further exclude the possibility of vibrationally excited CH_4 because its lifetime is even shorter than CH_3 [128]. CH_3O_2 is identified as the most abundant radical in models of CH_4-O_2 plasma [15] and is the most likely candidate. Unfortunately, the data regarding the electron impact ionization (EII) cross-section of CH_3O_2 is lacking and a quantitative study would require chemical ionization or photoionization [144],[155] which is not a capability of the MBMS used. Fu et al. [144] reported that the $CH_3O_2^+$ ion might be unstable and likely decomposes into CH_3^+ and O_2 depending on the excess energy during the ionization process. The calculated ionization potential of CH_3O_2 was 10.8 eV and the extra energy available from the 12.5 eV electrons in the ionizer would dissociate $CH_3O_2^+$ to yield CH_3^+. Meloni et al. [145] measured the photoionization efficiency curve for CH_3O_2,

yielding adiabatic ionization energy of CH_3O_2 to be (10.33±0.05 eV) and a CH_3^+– O_2 bond energy of 0.83±0.07 eV. The above information would suggest threshold energy of (11.2-11.5 eV) to produce CH_3^+ from CH_3O_2. This is consistent with our experimental findings showing that the CH_3^+ signal was close to the detection limit for an electron energy of 12.0 eV. The significant difference in CH_3^+ signals measured at 12.0 eV and 12.5 eV is more consistent with a threshold ionization of 12.0 eV rather than 9.84 eV of CH_3 as the ratio of the electron-impact ionization cross sections of CH_3 forming CH_3^+ at 12.0 eV and 12.5 eV is only 0.8. The above analysis is fully consistent with the interpretation of the MS signal at 15 amu to be due to CH_3O_2.

While there is no partial EII cross-section for CH_3^+ formation from CH_3O_2 available in the literature, we can still make an approximate estimation of the CH_3O_2 density based on the EII cross-section data for CH_3OH. The threshold energy to produce CH_3^+ from CH_3OH is about 13.8 eV, and the EII cross-section is about 2×10^{-18} cm^2 [146]. Assuming a similar EII cross-section for CH_3^+ formation from CH_3O_2 would yield the highest CH_3O_2 density in Figure 9.10(b) to be 2×10^{15} cm^{-3} with a calibration using CO_2 (m/z=44). Although this estimation has large uncertainties, it suggests that the density of CH_3O_2 can be on the order of 10^{15} cm^{-3}. This corresponds well to the observed increase of the absolute density of methanol of ~2×10^{15} cm^{-3}.

If assuming CH_3O_2 is the dominant radical in the afterglow region, its lifetime can be estimated according to its self-recombination reaction since its reaction with CH_4 or other long-lived molecules is very slow:

$$CH_4 + CH_3O_2 \rightarrow CH_3 + CH_3OOH\ ,\ k_3 = 1.03\times10^{-26}\ cm^3\ s^{-1}, \qquad \text{(R3)}$$

$$CH_3O_2 + CH_3O_2 \rightarrow CH_3OH + CH_2O + O_2,\ k_4 = 2.19\times10^{-13}\ cm^3\ s^{-1}, \quad (R4)$$

$$CH_3O_2 + CH_3O_2 \rightarrow 2CH_3O + O_2,\ k_5 = 1.29\times10^{-13}\ cm^3\ s^{-1}. \quad (R5)$$

The lifetime is estimated to be 1.4 ms if assuming an CH_3O_2 density of 2×10^{15} cm^{-3}. This lifetime is likely an overestimation as we neglected its reaction with other radicals such as H, O or OH. All the above analysis suggests that a density of CH_3O_2 on the order of 10^{15} cm^{-3} and its lifetime on the order of ~1 ms are consistent with our MBMS measurements.

Figure 9.10(b) shows the MS signal at 15 amu attributed to CH_3O_2 and the increase in the methanol as a function of plasma power. The trends of both CH_3O_2 and methanol as a function of plasma dissipated power are well correlated. In addition, the CH_3^+ signal is below the detection limit for plasma powers less than 4 W, consistent with the lack of increase in methanol compared to plasma only case suggestion that only for cases with a detectible amount of CH_3O_2 an enhancement of the methanol formation by the catalyst was found. This correlation suggests that CH_3O_2 might play a key role in the production of CH_3OH on the surface of the catalyst.

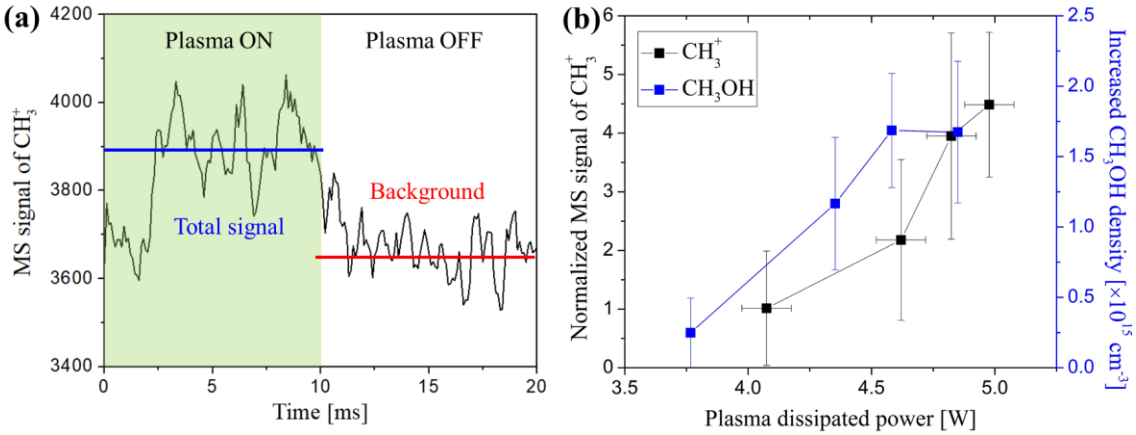

Figure 9.10: (a) Time-resolved MS signals of CH_3^+ attributed to CH_3O_2 (see text for details) for a plasma power of 4.7 W and an electrode to nozzle-distance of 5 mm; (b)

Correlation between the CH_3O_2 radical flux at the nozzle and the increase in CH_3OH production in the catalyst reactor as a function of plasma dissipated power.

Nonetheless, gas temperatures also vary with power as shown in Figure 9.8 which could impact catalytic reactions. At a distance of 5 mm, the gas temperature can reach 160 ºC at 5 W. The resulting elevation of the catalyst temperature might be able to trigger thermal catalysis which could enhance methanol production. To assess this effect, the impact of gas flow rates on the methanol production, gas temperature and radical density was measured. Figure 9.11 (a) shows that while the methanol density remains constant as a function of the gas flow rate for the plasma only case (resulting in a linear increase in methanol production as a function of gas flow rate), a reduction in the methanol density was observed when the catalyst is present resulting in the disappearance of a significant observed synergistic effect at a flow rate of 600 sccm.

Figure 9.11(b) shows the corresponding gas temperatures and MS signals of CH_3O_2. The gas temperature reduces from 160 ºC to about 100 ºC and the CH_3O_2 signal decrease about 70% with increasing gas flow rate from 200 sccm to 600 sccm. The similar trends do not allow to make a conclusion of the cause of the reduction in methanol-based on this data alone but a comparison with another condition at the same gas temperature provides more insights. The 400 sccm case has a gas temperature of about 125 ºC and the synergistic effect was observed. This case has the same gas temperature as the condition between 3 and 4 W in Figure 9.5(d), which does not show any synergistic effects. Hence, the observed synergistic effects can be attributed to plasma-produced species.

The strong correlation both for the power and gas flow variation between the CH_3O_2 signal and the CH_3OH suggests the dominant role of radicals and in particular radicals with an intermediate lifetime of 10s to 100s of microseconds like CH_3O_2.

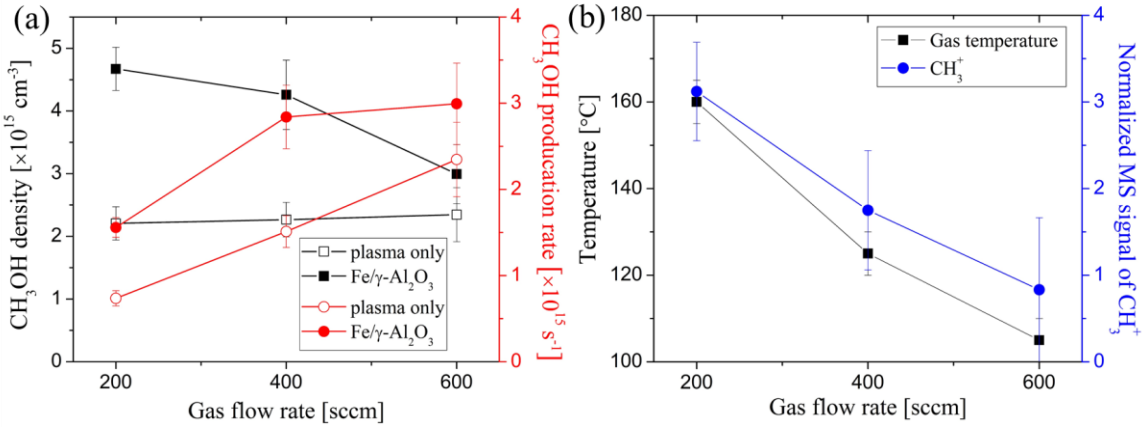

Figure 9.11: Impact of the gas flow rate at a fixed plasma dissipated power of 4.7 W±0.1 W on (a) CH_3OH density and production rates (b) gas temperature and MS signal of CH_3^+.

Yi et al [33] previously suggested that the production of CH_3OH could be attributed to the reaction between chemisorbed oxygen species with the plasma-produced CH_3 radicals to form CH_3O adsorbed at the surface. In the present study, this proposed mechanism is not able to explain the observed results in view of the sub-microsecond lifetime of the CH_3 radical. Nevertheless, another reaction pathway including the CH_3O_2 radicals is a more likely candidate to explain the increased CH_3OH production. For example, in the gas-phase plasma, the self-recombination of CH_3O_2 would lead to the formation of CH_3O radicals via R4-R5, which can chemisorb on the catalytic surface as CH_3O_{ad} yielding the same surface chemistry without the requirement of CH_3 radicals.

Further surface chemistry to form methanol from CH_3O_{ad} was proposed to involve H radicals [33]. If the reaction between H + CH_3O_{ad} is indeed responsible for the production of CH_3OH on the catalyst surface, the H density should be at least similar to the observed increase in methanol ~2×10^{15} cm^{-3}, the detection limit of the MBMS [156] hence this is highly unlikely as the lifetime of H is about ~2 µs (considering R2 and the three-body reaction between H and O_2 with a CH_3O_2 density of at least 2×10^{15} cm^{-3}). The diffusion

timescale of H over a distance of 20 µm is on the order of 4 µs according to the diffusion coefficients from [148]. which will lead to a large amount of gas phase recombination of H radicals before reaching the catalyst. This suggests that H cannot be responsible for the observed synergistic plasma-catalyst effect.

One possibility is that CH_3O_{ad} can react with itself to produce CH_3OH, like the equivalent gas-phase reaction:

$$CH_3O + CH_3O \rightarrow CH_2O + CH_3OH,\ k_6 = 1.0\times10^{-10}\ cm^3\ s^{-1}. \quad \text{(R6)}$$

Alternatively, reactions of CH_3O_{ad} with H_2, similar to their gas-phase equivalent might be possible if they would proceed at a higher rate than in the gas phase. In addition, Agarwal et al. [157] investigated aqueous selective CH_4 catalytic oxidation to CH_3OH and demonstrated that adding O_2 to the reaction mixture would produce CH_3O_2 radicals by reacting with CH_3 radicals. The proposed reaction pathway indicates the importance of CH_3O_2 radicals to enhance oxygenates' production in surface reactions.

While this study was performed in a separated plasma and catalyst reactor where the catalyst particles were not inside the active plasma region, an important outcome of this study is the large impact of transport limitations that will without doubt also play an important role for packed bed reactors where the catalyst is in 'direct contact' with the plasma. These transport limitations have been largely neglected when proposing surface reaction mechanisms in many plasma-catalysis studies. Even when a surface-hugging plasma might be in direct contact with the surface, a sheath will be present which depletes electrons near the interface of the catalyst and hence also radical production requiring radicals produced in the bulk plasma to diffuse through a sheath region. As a typical sheath

thickness at atmospheric pressure is of the order of 100 µm [104], this requires a diffusion time of the order of 10 to 100 µs for H and CH_3 at 400 K, suggesting that radicals with a lifetime of ~ 1 µs might even in the case of plasma in direct contact with the catalyst not dominantly contribute to plasma-catalyst interactions. We showed in this work that plasma-catalyst synergy is possible due to long-lived radical species such as alkylperoxy radicals with lifetimes comparable or larger than these diffusive timescales. While these species might be less reactive in the gas phase or on the surface they can still play a dominant role in plasma catalysis as they are less impacted by transport limitations on the typical length scales between pellets of hundreds of micrometers in pack-bed reactors.

9.6 Conclusion

In this chapter, the mechanisms underpinning the interaction of plasma with Fe/γ-Al_2O_3 catalyst in the context of direct conversion of methane to CO, CO_2 and oxygenates at room temperature are investigated by incorporating the catalyst reactor downstream of the plasma jet. An enhancement of CH_3OH in the presence of a catalyst compared to plasma only case is observed for the shortest distance between the plasma and catalyst studied in this work. Correlations between MBMS measurements and estimates of species lifetimes suggest that this synergistic effect is caused by radical species most likely CH_3O_2. It was possible to exclude dominant contributions of plasma-enabled heating on thermal catalysis for the synergistic effect while it was shown that gas heating even as low as 30-40 K was significantly impacting desorption rates of CH_3OH on alumina particles. While most studies in plasma catalysis seem to focus on Elay-Rideal reactions by primary radicals such as H and CH_3, this study shows that surface reactions induced by secondary more long-

lived radicals such as alkylperoxy radicals might be less impacted by transport limitations and their role in surface reactions might deserve more detailed attention.

Chapter 10

Summary and Future work

10.1 Summary

This research was motivated by the need to increase an understanding of plasma-catalyst interaction as plasma catalysis shows promise for gas conversion applications. The observed synergistic effects in plasma catalysis motivate researchers to perform detailed investigations of the used plasma sources as well as the catalyst surfaces. The main goal of this work is to correlate the changes in plasma-produced reactive species with the changes in catalyst surface species and chemical conversion yields to identify the key species responsible for the synergistic effects. The capability of MBMS to measure a broad range of species makes it the most suitable diagnostic technique for measuring gas-phase species at substrates.

Although MBMS is widely used and investigated by the combustion community, there are still many possibilities to improve and extend its detection ability particularly for species uniquely produced by plasmas. I spent the first year of my Ph.D. period designing and building an adjustable MBMS system to enable optimal operation conditions for both neutral and ionic species measurements. The first objective of this dissertation was to test the capabilities of the system and to interpret quantitatively the MBMS results. The change of the flow field in the presence of the sampling plate was considered and models to account for reactions in the near-surface boundary layer were developed to interpret the measured species densities by MBMS.

In addition, as electronically and vibrationally excited species are important and can be present at high densities in plasma, I developed detection and calibration methods for two excited species in this dissertation, $O_2(a^1\Delta_g)$ and $N_2(v)$. This enables a quantitative assessment of these two species in plasma catalysis or other applications. The ability to

measure axial and radial profiles of these two excited species impinging on a substrate is a key advantage of the MBMS diagnostic method over previously reported optical methods. In addition, a new ion calibration method by MBMS is proposed for cold ions present in the effluents of the APPJ. The absolute densities of positive ions presented in this dissertation enable for the first time a quantitative evaluation of both neutral and ionic species in APPJs by experiments. More broadly, these results in this dissertation further extend the capability of the MBMS technique, which could be beneficial for the low-temperature plasma community or beyond.

The new capabilities of the MBMS not only helped us to reveal mechanisms in plasma-surface interaction, but also enable a better understanding of the plasma source studied in this work. The second part of this dissertation focuses on the influences of plasma parameters on species fluxes impinging on substrates. The studies showed that the sensitivities of parameters are different, and species fluxes can be tuned and controlled by some key parameters. The impact of the surface-dependent loss probability and boundary layer reactions on the species flux to a substrate and how this qualitatively relates to the MBMS density measurements were also investigated. In addition, it is also found that the MBMS can be a good technique, due to its excellent detection limit, to quantify pre-ionization in plasmas leading to 'memory effects'. We measured absolute ion density in modulated plasma immediately before the plasma ignition enabling for the first time a quantitative correlation between pre-ionization densities and observed memory effects.

Lastly, the MBMS characterization is correlated with the surface characterization of a catalytic bed to shed light on the mechanism of the plasma catalysis in the context of partial oxidation of methane to both syngas and oxygenates. A strong correlation between atomic

O flux and CH_4 conversion was identified suggesting its importance for the oxidation of CH_4 to CO and CO_2. The formation of surface CH_n was found to likely be the rate-determining step of the production of CO and CO_2 at 500 ^oC in plasma catalysis. In addition, the plasma-induced gas heating effects were shown to significantly impact the desorption rates of methanol from particle surfaces. Correlations between MBMS measurements and estimates of species lifetimes suggest that the synergistic effect in methanol production is caused by radical species most likely CH_3O_2, indicating surface reactions induced by secondary more long-lived radicals such as alkylperoxy radicals might be less impacted by transport limitations. These results are important to gain insights into plasma catalysis and beneficial for bringing up possible strategies to further improve the synergistic effects and energy efficiency ultimately enabling plasma catalysis to contribute to the electrification of the chemical industry.

10.2 Future work

The results in this dissertation suggest these remnants still several important tasks to be performed. Although the measurement method of vibrationally excited $N_2(v)$ was developed in this study, it is based on several assumptions of which the most important one is the Treanor-like vibrational distribution function. Hence it would be highly beneficial to have a direct comparison between MBMS and another diagnostic technique for identical plasma conditions to fully validate the interpretation of the MBMS measurements. In addition, other vibrationally excited species such as $CH_4(v)$ and $CO_2(v)$ of which are also believed to be important in plasma catalysis might also be detectable using MBMS and would be highly valuable for the plasma catalysis community.

In addition, a detailed model considering surface reactions needs to be developed for partial oxidation of methane similar to the work of NH_3 synthesis. Considering the huge difference observed in one-stage and two-stage plasma-catalyst reactors and the focus of this work on the latter it would be interesting to extend the work to *in situ* measurements of surface ionization waves on the catalyst/support surface. The sampling plate of MBMS can be made of dielectric materials, enabling the investigation of plasma-dielectric surface interaction. Instead of radio-frequency power sources, other sources such as high-voltage pulses can be used to create surface ionization waves on dielectric surfaces. These possible studies could help us have a better understanding of the plasma sources and also the plasma-surface interaction in plasma catalysis, particularly for ionic species which were not dominant species for the conditions studied in this work.

Reference

[1] Fricke, K.; Steffen, H.; von Woedtke, T.; Schröder, K.; Weltmann, K.-D. High Rate Etching of Polymers by Means of an Atmospheric Pressure Plasma Jet. *Plasma Process. Polym.* **2011**, *8* (1), 51–58.

[2] Niemira, B. A. Cold Plasma Decontamination of Foods. *Annu. Rev. Food Sci. Technol.* **2012**, *3* (1), 125–142.

[3] Foster, J.; Sommers, B. S.; Gucker, S. N.; Blankson, I. M.; Adamovsky, G. Perspectives on the Interaction of Plasmas With Liquid Water for Water Purification. *IEEE Trans. Plasma Sci.* **2012**, *40* (5), 1311–1323.

[4] Lieberman, M. A.; Lichtenberg, A. J. *Principles of Plasma Discharges and Materials Processing*; John Wiley & Sons, Inc.: Hoboken, NJ, USA, 2005.

[5] Bárdos, L.; Baránková, H. Cold Atmospheric Plasma: Sources, Processes, and Applications. *Thin Solid Films* **2010**, *518* (23), 6705–6713.

[6] Lu, X.; Laroussi, M.; Puech, V. On Atmospheric-Pressure Non-Equilibrium Plasma Jets and Plasma Bullets. *Plasma Sources Sci. Technol.* **2012**, *21* (3), 034005.

[7] Bekeschus, S.; Schmidt, A.; Weltmann, K.-D.; von Woedtke, T. The Plasma Jet KINPen – A Powerful Tool for Wound Healing. *Clin. Plasma Med.* **2016**, *4* (1), 19–28.

[8] Schutze, a; Jeong, J. Y.; Babayan, S. E.; Park, J.; Selwyn, G. S.; Hicks, R. F. The Atmospheric-Pressure Plasma Jet: A Review and Comparison to Other Plasma Sources. *Plasma Sci. IEEE Trans.* **1998**, *26* (6), 1685–1694.

[9] Aboubakr, H. A.; Gangal, U.; Youssef, M. M.; Goyal, S. M.; Bruggeman, P. J. Inactivation of Virus in Solution by Cold Atmospheric Pressure Plasma: Identification of Chemical Inactivation Pathways. *J. Phys. D. Appl. Phys.* **2016**, *49*

(20), 204001.

[10] Hofmann, S.; van Gils, K.; van der Linden, S.; Iseni, S.; Bruggeman, P. Time and Spatial Resolved Optical and Electrical Characteristics of Continuous and Time Modulated RF Plasmas in Contact with Conductive and Dielectric Substrates. *Eur. Phys. J. D* **2014**, *68* (3), 56.

[11] Park, S.; Liao, F.; Larson, J. M.; Girshick, S. L.; Zachariah, M. R. Molecular Beam Mass Spectrometry System for Characterization of Thermal Plasma Chemical Vapor Deposition. *Plasma Chem. Plasma Process.* **2004**, *24* (3), 353–372.

[12] Dünnbier, M.; Schmidt-Bleker, A.; Winter, J.; Wolfram, M.; Hippler, R.; Weltmann, K.-D.; Reuter, S. Ambient Air Particle Transport into the Effluent of a Cold Atmospheric-Pressure Argon Plasma Jet Investigated by Molecular Beam Mass Spectrometry. *J. Phys. D. Appl. Phys.* **2013**, *46* (43), 435203.

[13] Benedikt, J.; Ellerweg, D.; Von Keudell, A. Molecular Beam Sampling System with Very High Beam-to-Background Ratio: The Rotating Skimmer Concept. *Rev. Sci. Instrum.* **2009**, *80* (5).

[14] Scoles, G. *Atomic and Molecular Beam Methods*; Oxford university press, 1988.

[15] Große-Kreul, S.; Hübner, S.; Schneider, S.; Ellerweg, D.; von Keudell, A.; Matejčík, S.; Benedikt, J. Mass Spectrometry of Atmospheric Pressure Plasmas. *Plasma Sources Sci. Technol.* **2015**, *24* (4), 044008.

[16] Bruggeman, P.; Iza, F.; Lauwers, D.; Gonzalvo, Y. A. Mass Spectrometry Study of Positive and Negative Ions in a Capacitively Coupled Atmospheric Pressure RF Excited Glow Discharge in He–Water Mixtures. *J. Phys. D. Appl. Phys.* **2010**, *43* (1), 012003.

[17] Whitehead, J. C. Plasma Catalysis: A Solution for Environmental Problems. *Pure Appl. Chem.* **2010**, *82* (6), 1329–1336.

[18] Tu, X.; Whitehead, J. C. Plasma-Catalytic Dry Reforming of Methane in an Atmospheric Dielectric Barrier Discharge: Understanding the Synergistic Effect at Low Temperature. *Appl. Catal. B Environ.* **2012**, *125*, 439–448.

[19] Allah, Z. A.; Whitehead, J. C. Plasma-Catalytic Dry Reforming of Methane in an Atmospheric Pressure AC Gliding Arc Discharge. *Catal. Today* **2015**, *256* (P1), 76–79.

[20] Nozaki, T.; Muto, N.; Kadio, S.; Okazaki, K. Dissociation of Vibrationally Excited Methane on Ni Catalyst: Part 2. Process Diagnostics by Emission Spectroscopy. *Catal. Today* **2004**, *89* (1–2), 67–74.

[21] Zhang, A. J.; Zhu, A. M.; Guo, J.; Xu, Y.; Shi, C. Conversion of Greenhouse Gases into Syngas via Combined Effects of Discharge Activation and Catalysis. *Chem. Eng. J.* **2010**.

[22] Bröer, S.; Hammer, T. Selective Catalytic Reduction of Nitrogen Oxides by Combining a Non-Thermal Plasma and a V_2O_5-WO_3/TiO_2 Catalyst. *Appl. Catal. B*

Environ. **2000**, *28* (2), 101–111.

[23] Bogaerts, A.; Tu, X.; Whitehead, J. C.; Centi, G.; Lefferts, L.; Guaitella, O.; Azzolina-Jury, F.; Kim, H.-H.; Murphy, A. B.; Schneider, W. F.; et al. The 2020 Plasma Catalysis Roadmap. *J. Phys. D. Appl. Phys.* **2020**, *53* (44), 443001.

[24] Whitehead, J. C. Plasma–Catalysis: The Known Knowns, the Known Unknowns and the Unknown Unknowns. *J. Phys. D. Appl. Phys.* **2016**, *49* (24), 243001.

[25] Li, S.; Ahmed, R.; Yi, Y.; Bogaerts, A. Methane to Methanol through Heterogeneous Catalysis and Plasma Catalysis. *Catalysts* **2021**, *11* (5), 590.

[26] Nozaki, T.; Okazaki, K. Non-Thermal Plasma Catalysis of Methane: Principles, Energy Efficiency, and Applications. *Catal. Today* **2013**, *211*, 29–38.

[27] Snoeckx, R.; Zeng, Y. X.; Tu, X.; Bogaerts, A. Plasma-Based Dry Reforming: Improving the Conversion and Energy Efficiency in a Dielectric Barrier Discharge. *RSC Adv.* **2015**, *5* (38), 29799–29808.

[28] Khoja, A. H.; Tahir, M.; Amin, N. A. S. Recent Developments in Non-Thermal Catalytic DBD Plasma Reactor for Dry Reforming of Methane. *Energy Convers. Manag.* **2019**, *183*, 529–560.

[29] Pietruszka, B.; Anklam, K.; Heintze, M. Plasma-Assisted Partial Oxidation of Methane to Synthesis Gas in a Dielectric Barrier Discharge. *Appl. Catal. A Gen.* **2004**, *261* (1), 19–24.

[30] Song, L.; Kong, Y.; Li, X. Hydrogen Production from Partial Oxidation of Methane over Dielectric Barrier Discharge Plasma and NiO/γ-Al_2O_3 Catalyst. *Int. J. Hydrogen Energy* **2017**, *42* (31), 19869–19876.

[31] Shareei, M.; Taghvaei, H.; Azimi, A.; Shahbazi, A.; Mirzaei, M. Catalytic DBD Plasma Reactor for Low Temperature Partial Oxidation of Methane: Maximization of Synthesis Gas and Minimization of CO_2. *Int. J. Hydrogen Energy* **2019**, *44* (60), 31873–31883.

[32] Loenders, B.; Engelmann, Y.; Bogaerts, A. Plasma-Catalytic Partial Oxidation of Methane on Pt(111): A Microkinetic Study on the Role of Different Plasma Species. *J. Phys. Chem. C* **2021**, *125* (5), 2966–2983.

[33] Yi, Y.; Li, S.; Cui, Z.; Hao, Y.; Zhang, Y.; Wang, L.; Liu, P.; Tu, X.; Xu, X.; Guo, H.; et al. Selective Oxidation of CH_4 to CH_3OH through Plasma Catalysis: Insights from Catalyst Characterization and Chemical Kinetics Modelling. *Appl. Catal. B Environ.* **2021**, *296*, 120384.

[34] Chawdhury, P.; Wang, Y.; Ray, D.; Mathieu, S.; Wang, N.; Harding, J.; Bin, F.; Tu, X.; Subrahmanyam, C. A Promising Plasma-Catalytic Approach towards Single-Step Methane Conversion to Oxygenates at Room Temperature. *Appl. Catal. B Environ.* **2021**, *284*, 119735.

[35] Zhang, S.; Li, Y.; Knoll, A.; Oehrlein, G. S. Mechanistic Aspects of Plasma-Enhanced Catalytic Methane Decomposition by Time-Resolved Operando Diffuse

Reflectance Infrared Fourier Transform Spectroscopy. *J. Phys. D. Appl. Phys.* **2020**, *53* (21), 215201.

[36] Knoll, A. J.; Zhang, S.; Lai, M.; Luan, P.; Oehrlein, G. S. Infrared Studies of Gas Phase and Surface Processes of the Enhancement of Catalytic Methane Decomposition by Low Temperature Plasma. *J. Phys. D. Appl. Phys.* **2019**, *52* (22), 225201.

[37] Mehta, P.; Barboun, P.; Herrera, F. A.; Kim, J.; Rumbach, P.; Go, D. B.; Hicks, J. C.; Schneider, W. F. Overcoming Ammonia Synthesis Scaling Relations with Plasma-Enabled Catalysis. *Nat. Catal.* **2018**, *1* (4), 269–275.

[38] Barboun, P.; Mehta, P.; Herrera, F. A.; Go, D. B.; Schneider, W. F.; Hicks, J. C. Distinguishing Plasma Contributions to Catalyst Performance in Plasma-Assisted Ammonia Synthesis. *ACS Sustain. Chem. Eng.* **2019**, *7* (9), 8621–8630.

[39] Winter, L. R.; Ashford, B.; Hong, J.; Murphy, A. B.; Chen, J. G. Identifying Surface Reaction Intermediates in Plasma Catalytic Ammonia Synthesis. *ACS Catal.* **2020**, *10* (24), 14763–14774.

[40] Barboun, P. M.; Daemen, L. L.; Waitt, C.; Wu, Z.; Schneider, W. F.; Hicks, J. C. Inelastic Neutron Scattering Observation of Plasma-Promoted Nitrogen Reduction Intermediates on Ni/γ-Al2O3. *ACS Energy Lett.* **2021**, *6* (6), 2048–2053.

[41] Neyts, E. C. Plasma-Surface Interactions in Plasma Catalysis. *Plasma Chem. Plasma Process.* **2016**, *36* (1), 185–212.

[42] Yu, Q.; Kong, M.; Liu, T.; Fei, J.; Zheng, X. Characteristics of the Decomposition of CO2 in a Dielectric Packed-Bed Plasma Reactor. *Plasma Chem. Plasma Process.* **2012**, *32* (1), 153–163.

[43] Park, S.; Lee, M.; Bae, J.; Hong, D. Y.; Park, Y. K.; Hwang, Y. K.; Jeong, M. G.; Kim, Y. D. Plasma-Assisted Non-Oxidative Conversion of Methane over Mo/HZSM-5 Catalyst in DBD Reactor. *Top. Catal.* **2017**, *60* (9–11), 735–742.

[44] Neyts, E. C.; Ostrikov, K. (Ken); Sunkara, M. K.; Bogaerts, A. Plasma Catalysis: Synergistic Effects at the Nanoscale. *Chem. Rev.* **2015**, *115* (24), 13408–13446.

[45] van Ham, B. T. J.; Hofmann, S.; Brandenburg, R.; Bruggeman, P. J. In Situ Absolute Air, O_3 and NO Densities in the Effluent of a Cold RF Argon Atmospheric Pressure Plasma Jet Obtained by Molecular Beam Mass Spectrometry. *J. Phys. D. Appl. Phys.* **2014**, *47* (22), 224013.

[46] Zhang, S.; Sobota, A.; van Veldhuizen, E. M.; Bruggeman, P. J. Gas Flow Characteristics of a Time Modulated APPJ: The Effect of Gas Heating on Flow Dynamics. *J. Phys. D. Appl. Phys.* **2015**, *48* (1), 015203.

[47] Zhang, S.; van Gaens, W.; van Gessel, B.; Hofmann, S.; van Veldhuizen, E.; Bogaerts, A.; Bruggeman, P. Spatially Resolved Ozone Densities and Gas Temperatures in a Time Modulated RF Driven Atmospheric Pressure Plasma Jet: An Analysis of the Production and Destruction Mechanisms. *J. Phys. D. Appl. Phys.* **2013**, *46* (20), 205202.

[48] Kong, M. G.; Kroesen, G.; Morfill, G.; Nosenko, T.; Shimizu, T.; van Dijk, J.; Zimmermann, J. L. Plasma Medicine: An Introductory Review. *New J. Phys.* **2009**, *11* (11), 115012.

[49] Fridman, G.; Friedman, G.; Gutsol, A.; Shekhter, A. B.; Vasilets, V. N.; Fridman, A. Applied Plasma Medicine. *Plasma Process. Polym.* **2008**, *5* (6), 503–533.

[50] Adamovich, I.; Baalrud, S. D.; Bogaerts, A.; Bruggeman, P. J.; Cappelli, M.; Colombo, V.; Czarnetzki, U.; Ebert, U.; Eden, J. G.; Favia, P.; et al. The 2017 Plasma Roadmap: Low Temperature Plasma Science and Technology. *J. Phys. D. Appl. Phys.* **2017**, *50* (32), 323001.

[51] Weltmann, K.-D.; Kindel, E.; Brandenburg, R.; Meyer, C.; Bussiahn, R.; Wilke, C.; von Woedtke, T. Atmospheric Pressure Plasma Jet for Medical Therapy: Plasma Parameters and Risk Estimation. *Contrib. to Plasma Phys.* **2009**, *49* (9), 631–640.

[52] Stoffels, E.; Sakiyama, Y.; Graves, D. B. Cold Atmospheric Plasma: Charged Species and Their Interactions With Cells and Tissues. *IEEE Trans. Plasma Sci.* **2008**, *36* (4), 1441–1457.

[53] Kondeti, V. S. S. K.; Phan, C. Q.; Wende, K.; Jablonowski, H.; Gangal, U.; Granick, J. L.; Hunter, R. C.; Bruggeman, P. J. Long-Lived and Short-Lived Reactive Species Produced by a Cold Atmospheric Pressure Plasma Jet for the Inactivation of Pseudomonas Aeruginosa and Staphylococcus Aureus. *Free Radic. Biol. Med.* **2018**, *124*, 275–287.

[54] Zhang, S.; Sobota, A.; van Veldhuizen, E. M.; Bruggeman, P. J. Temporally Resolved Ozone Distribution of a Time Modulated RF Atmospheric Pressure Argon Plasma Jet: Flow, Chemical Reaction, and Transient Vortex. *Plasma Sources Sci. Technol.* **2015**, *24* (4), 045015.

[55] Reuter, S.; Winter, J.; Schmidt-Bleker, A.; Schroeder, D.; Lange, H.; Knake, N.; Schulz-von der Gathen, V.; Weltmann, K.-D. Atomic Oxygen in a Cold Argon Plasma Jet: TALIF Spectroscopy in Ambient Air with Modelling and Measurements of Ambient Species Diffusion. *Plasma Sources Sci. Technol.* **2012**, *21* (2), 024005.

[56] Azarpazhooh, A.; Limeback, H. The Application of Ozone in Dentistry : A Systematic Review of Literature. **2008**, *36*, 104–116.

[57] Ho, M.-H.; Lee, J.-J.; Fan, S.-C.; Wang, D.-M.; Hou, L.-T.; Hsieh, H.-J.; Lai, J.-Y. Efficient Modification on PLLA by Ozone Treatment for Biomedical Applications. *Macromol. Biosci.* **2007**, *7* (4), 467–474.

[58] Mokoena, M. L.; Brink, C. B.; Harvey, B. H.; Oliver, D. W. Appraisal of Ozone as Biologically Active Molecule and Experimental Tool in Biomedical Sciences. *Med. Chem. Res.* **2011**, *20* (9), 1687–1695.

[59] Ellerweg, D.; von Keudell, A.; Benedikt, J. Unexpected O and O_3 Production in the Effluent of He/O_2 Microplasma Jets Emanating into Ambient Air. *Plasma Sources Sci. Technol.* **2012**, *21* (3), 034019.

[60] Yanallah, K.; Pontiga, F.; Fernández-Rueda, A.; Castellanos, A. Experimental

Investigation and Numerical Modelling of Positive Corona Discharge: Ozone Generation. *J. Phys. D. Appl. Phys.* **2009**, *42* (6), 065202.

[61] Pekárek, S. Non-Thermal Plasma Ozone Generation. *Acta Polytech.* **2003**, *43* (6).

[62] Voráč, J.; Britun, N.; Nikiforov, A.; Snyders, R.; Leys, C.; Krumpolec, R.; Zemánek, M. Photofragmentation Laser-Induced Fluorescence of Ozone: An in Situ Tool for Precise Mapping of Ozone Concentration in Non-Thermal Plasmas. *Appl. Phys. Express* **2019**, *12* (10), 106001.

[63] Schmidt-Bleker, A.; Winter, J.; Iseni, S.; Dünnbier, M.; Weltmann, K.-D.; Reuter, S. Reactive Species Output of a Plasma Jet with a Shielding Gas Device—Combination of FTIR Absorption Spectroscopy and Gas Phase Modelling. *J. Phys. D. Appl. Phys.* **2014**, *47* (14), 145201.

[64] Robert, E.; Sarron, V.; Darny, T.; Riès, D.; Dozias, S.; Fontane, J.; Joly, L.; Pouvesle, J.-M. Rare Gas Flow Structuration in Plasma Jet Experiments. *Plasma Sources Sci. Technol.* **2014**, *23* (1), 012003.

[65] Kondeti, V. S. S. K.; Gangal, U.; Yatom, S.; Bruggeman, P. J. Ag^+ Reduction and Silver Nanoparticle Synthesis at the Plasma–Liquid Interface by an RF Driven Atmospheric Pressure Plasma Jet: Mechanisms and the Effect of Surfactant. *J. Vac. Sci. Technol. A Vacuum, Surfaces, Film.* **2017**, *35* (6), 061302.

[66] Hofmann, S.; van Gessel, A. F. H.; Verreycken, T.; Bruggeman, P. Power Dissipation, Gas Temperatures and Electron Densities of Cold Atmospheric Pressure Helium and Argon RF Plasma Jets. *Plasma Sources Sci. Technol.* **2011**, *20* (6), 065010.

[67] Agarwal, S.; Quax, G. W. W.; van de Sanden, M. C. M.; Maroudas, D.; Aydil, E. S. Measurement of Absolute Radical Densities in a Plasma Using Modulated-Beam Line-of-Sight Threshold Ionization Mass Spectrometry. *J. Vac. Sci. Technol. A Vacuum, Surfaces, Film.* **2004**, *22* (1), 71–81.

[68] Krähling, T.; Ellerweg, D.; Benedikt, J. The Influence of the Ionizer Geometry on the Absolute Density Calibration of Reactive Neutral Species in a Molecular Beam Mass Spectrometry. *Rev. Sci. Instrum.* **2012**, *83* (4), 045114.

[69] Ellerweg, D.; Benedikt, J.; Von Keudell, A.; Knake, N.; Schulz-Von Der Gathen, V. Characterization of the Effluent of a He/O_2 Microscale Atmospheric Pressure Plasma Jet by Quantitative Molecular Beam Mass Spectrometry. *New J. Phys.* **2010**, *12*, 0–12.

[70] Aranda Gonzalvo, Y.; Whitmore, T. D.; Rees, J. A.; Seymour, D. L.; Stoffels, E. Atmospheric Pressure Plasma Analysis by Modulated Molecular Beam Mass Spectrometry. *J. Vac. Sci. Technol. A Vacuum, Surfaces, Film.* **2006**, *24* (3), 550–553.

[71] Guha, J.; Donnelly, V. M.; Pu, Y. K. Mass and Auger Electron Spectroscopy Studies of the Interactions of Atomic and Molecular Chlorine on a Plasma Reactor Wall. *J. Appl. Phys.* **2008**, *103* (1), 013306.

[72] Willems, G.; Benedikt, J.; von Keudell, A. Absolutely Calibrated Mass Spectrometry Measurement of Reactive and Stable Plasma Chemistry Products in the Effluent of a He/H_2O Atmospheric Plasma. *J. Phys. D. Appl. Phys.* **2017**, *50* (33), 335204.

[73] Cunge, G.; Bodart, P.; Brihoum, M.; Boulard, F.; Chevolleau, T.; Sadeghi, N. Measurement of Free Radical Kinetics in Pulsed Plasmas by UV and VUV Absorption Spectroscopy and by Modulated Beam Mass Spectrometry. *Plasma Sources Sci. Technol.* **2012**, *21* (2), 024006.

[74] Bohlmark, J.; Lattemann, M.; Gudmundsson, J. T.; Ehiasarian, A. P.; Aranda Gonzalvo, Y.; Brenning, N.; Helmersson, U. The Ion Energy Distributions and Ion Flux Composition from a High Power Impulse Magnetron Sputtering Discharge. *Thin Solid Films* **2006**, *515* (4), 1522–1526.

[75] Singh, H.; Coburn, J. W.; Graves, D. B. Appearance Potential Mass Spectrometry: Discrimination of Dissociative Ionization Products. *J. Vac. Sci. Technol. A Vacuum, Surfaces, Film.* **2000**, *18* (2), 299–305.

[76] Thompson, W. R.; Shah, M. B.; Gilbody, H. B. Single and Double Ionization of Atomic Oxygen by Electron Impact. *J. Phys. B At. Mol. Opt. Phys.* **1995**, *28* (7), 1321–1330.

[77] Orient, O. J.; Strivastava, S. K. Electron Impact Ionisation of H_2O, CO, CO_2 and CH_4. *J. Phys. B At. Mol. Phys.* **1987**, *20* (15), 3923–3936.

[78] Nayak, G.; Sousa, J. S.; Bruggeman, P. J. Singlet Delta Oxygen Production in a 2D Micro-Discharge Array in Air: Effect of Gas Residence Time and Discharge Power. *J. Phys. D. Appl. Phys.* **2017**, *50* (10), 105205.

[79] Gaens, W. Van; Bogaerts, A. Kinetic Modelling for an Atmospheric Pressure Argon Plasma Jet in Humid Air. *J. Phys. D. Appl. Phys.* **2013**, *46* (27), 275201.

[80] Stafford, D. S.; Kushner, M. J. $O_2(\Delta^1)$ Production in He/O_2 Mixtures in Flowing Low Pressure Plasmas. *J. Appl. Phys.* **2004**, *96* (5), 2451–2465.

[81] Gaens, W. Van; Bruggeman, P. J.; Bogaerts, A. Numerical Analysis of the NO and O Generation Mechanism in a Needle-Type Plasma Jet. *New J. Phys.* **2014**, *16* (6), 063054.

[82] Lietz, A. M.; Kushner, M. J. Air Plasma Treatment of Liquid Covered Tissue: Long Timescale Chemistry. *J. Phys. D. Appl. Phys.* **2016**, *49* (42), 425204.

[83] Jeong, J. Y.; Park, J.; Henins, I.; Babayan, S. E.; Tu, V. J.; Selwyn, G. S.; Ding, G.; Hicks, R. F. Reaction Chemistry in the Afterglow of an Oxygen−Helium, Atmospheric-Pressure Plasma. *J. Phys. Chem. A* **2000**, *104* (34), 8027–8032.

[84] Schmidt, J. B. Ultrashort Two-Photon-Absorption Laser-Induced Fluorescence in Nanosecond-Duration, Repetitively Pulsed Discharges. PhD thesis, The Ohio State University 2015.

[85] van Gessel, B.; Brandenburg, R.; Bruggeman, P. Electron Properties and Air Mixing

in Radio Frequency Driven Argon Plasma Jets at Atmospheric Pressure. *Appl. Phys. Lett.* **2013**, *103* (6), 064103.

[86] Wende, K.; Williams, P.; Dalluge, J.; Van Gaens, W.; Aboubakr, H.; Bischof, J.; von Woedtke, T.; Goyal, S. M.; Weltmann, K.-D.; Bogaerts, A.; et al. Identification of the Biologically Active Liquid Chemistry Induced by a Nonthermal Atmospheric Pressure Plasma Jet. *Biointerphases* **2015**, *10* (2), 029518.

[87] Vieceli, J.; Roeselová, M.; Potter, N.; Dang, L. X.; Garrett, B. C.; Douglas J. Tobias. Molecular Dynamics Simulations of Atmospheric Oxidants at the Air−Water Interface: Solvation and Accommodation of OH and O_3. *J. Phys. Chem. B* **2005**, *109* (33), 15876–15892.

[88] Zehr, J. P.; Capone, D. G. Fundamentals of N_2 Fixation. In *Marine Nitrogen Fixation*; Springer International Publishing: Cham, 2021; pp 9–29.

[89] Vakili, R.; Gholami, R.; Stere, C. E.; Chansai, S.; Chen, H.; Holmes, S. M.; Jiao, Y.; Hardacre, C.; Fan, X. Plasma-Assisted Catalytic Dry Reforming of Methane (DRM) over Metal-Organic Frameworks (MOFs)-Based Catalysts. *Appl. Catal. B Environ.* **2020**, *260*, 118195.

[90] Fan, X.; Kang, S.; Li, J.; Zhu, T. Formation of Nitrogen Oxides (N_2O, NO, and NO_2) in Typical Plasma and Plasma-Catalytic Processes for Air Pollution Control. *Water, Air, Soil Pollut.* **2018**, *229* (11), 351.

[91] Xie, Q.; Zhuge, S.; Song, X.; Lu, M.; Yu, F.; Ruan, R.; Nie, Y. Non-Thermal Atmospheric Plasma Synthesis of Ammonia in a DBD Reactor Packed with Various Catalysts. *J. Phys. D. Appl. Phys.* **2020**, *53* (6), 064002.

[92] Carreon, M. L. Plasma Catalytic Ammonia Synthesis: State of the Art and Future Directions. *J. Phys. D. Appl. Phys.* **2019**, *52* (48), 483001.

[93] Rouwenhorst, K. H. R.; Jardali, F.; Bogaerts, A.; Lefferts, L. From the Birkeland–Eyde Process towards Energy-Efficient Plasma-Based NO_X Synthesis: A Techno-Economic Analysis. *Energy Environ. Sci.* **2021**, *14* (5), 2520–2534.

[94] Rouwenhorst, K. H. R.; Engelmann, Y.; Van 'T Veer, K.; Postma, R. S.; Bogaerts, A.; Lefferts, L. Plasma-Driven Catalysis: Green Ammonia Synthesis with Intermittent Electricity. *Green Chem.* **2020**, *22* (19), 6258–6287.

[95] Rouwenhorst, K. H. R.; Kim, H. H.; Lefferts, L. Vibrationally Excited Activation of N2 in Plasma-Enhanced Catalytic Ammonia Synthesis: A Kinetic Analysis. *ACS Sustain. Chem. Eng.* **2019**, *7* (20), 17515–17522.

[96] Montello, A.; Yin, Z.; Burnette, D.; Adamovich, I. V.; Lempert, W. R. Picosecond CARS Measurements of Nitrogen Vibrational Loading and Rotational/Translational Temperature in Non-Equilibrium Discharges. *J. Phys. D. Appl. Phys.* **2013**, *46* (46), 464002.

[97] Roettgen, A.; Lempert, W.; Adamovich, I. Measurements of N_2 Vibrational Distribution Function in Pulsed Nanosecond Nonequilibrium Discharge by Spontaneous Raman Scattering. In *51st AIAA Aerospace Sciences Meeting including*

the New Horizons Forum and Aerospace Exposition; American Institute of Aeronautics and Astronautics: Reston, Virigina, 2013.

[98] Kuhfeld, J.; Lepikhin, N. D.; Luggenhölscher, D.; Czarnetzki, U. Vibrational CARS Measurements in a Near-Atmospheric Pressure Plasma Jet in Nitrogen: I. Measurement Procedure and Results. *J. Phys. D. Appl. Phys.* **2021**, *54* (30), 305204.

[99] Kuhfeld, J.; Luggenhölscher, D.; Czarnetzki, U. Vibrational CARS Measurements in a Near-Atmospheric Pressure Plasma Jet in Nitrogen: II. Analysis. *J. Phys. D. Appl. Phys.* **2021**, *54* (30), 305205.

[100] Agarwal, S.; Hoex, B.; van de Sanden, M. C. M.; Maroudas, D.; Aydil, E. S. Absolute Densities of N and Excited N2 in a N2 Plasma. *Appl. Phys. Lett.* **2003**, *83* (24), 4918–4920.

[101] Große-Kreul, S.; Hübner, S.; Schneider, S.; Ellerweg, D.; von Keudell, A.; Matejčík, S.; Benedikt, J. Mass Spectrometry of Atmospheric Pressure Plasmas. *Plasma Sources Sci. Technol.* **2015**, *24* (4), 044008.

[102] Jiang, J.; Gonzalvo, Y. A.; Bruggeman, P. J. Spatially Resolved Density Measurements of Singlet Delta Oxygen in a Non-Equilibrium Atmospheric Pressure Plasma Jet by Molecular Beam Mass Spectrometry. *Plasma Sources Sci. Technol.* **2020**, *29* (4), 045023.

[103] Miller, R. E. The Absolute Energy of the State of Nitrogen. *J. Mol. Spectrosc.* **1966**, *19* (1–4), 185–187.

[104] Benedikt, J.; Hecimovic, A.; Ellerweg, D.; von Keudell, A. Quadrupole Mass Spectrometry of Reactive Plasmas. *J. Phys. D. Appl. Phys.* **2012**, *45* (40), 403001.

[105] Silva, T.; Grofulović, M.; Klarenaar, B. L. M.; Morillo-Candas, A. S.; Guaitella, O.; Engeln, R.; Pintassilgo, C. D.; Guerra, V. Kinetic Study of Low-Temperature CO_2 Plasmas under Non-Equilibrium Conditions. I. Relaxation of Vibrational Energy. *Plasma Sources Sci. Technol.* **2018**, *27* (1), 015019.

[106] Capitelli, M.; Colonna, G.; D'Ammando, G.; Pietanza, L. D. Self-Consistent Time Dependent Vibrational and Free Electron Kinetics for CO_2 Dissociation and Ionization in Cold Plasmas. *Plasma Sources Sci. Technol.* **2017**, *26* (5), 055009.

[107] Lino da Silva, M.; Guerra, V.; Loureiro, J.; Sá, P. A. Vibrational Distributions in N_2 with an Improved Calculation of Energy Levels Using the RKR Method. *Chem. Phys.* **2008**, *348* (1–3), 187–194.

[108] Rusanov, V. D.; Fridman, A. A.; Sholin, G. V. The Physics of a Chemically Active Plasma with Nonequilibrium Vibrational Excitation of Molecules. *Uspekhi Fiz. Nauk* **1981**, *134* (6), 185.

[109] Rusanov, V. D.; Fridman, A. A.; Sholin, G. V. Population of Vibrationally Excited States of Diatomic Molecules in a Nonequilibrium Plasma in the Diffusion Approximation. *Sov. physics. Tech. Phys.* **1979**, *49*, 554–561.

[110] Fridman, A. *Plasma Chemistry*; Cambridge University Press: Cambridge, 2008.

[111] Viegas, P.; van de Sanden, M. C. M.; Longo, S.; Diomede, P. Validation of the Fokker–Planck Approach to Vibrational Kinetics in CO_2 Plasma. *J. Phys. Chem. C* **2019**, *123* (37), 22823–22831.

[112] Caleb Richards; Elijah Jans; Ilya Gulko; Keegan Orr; Igor V. Adamovich. N_2 Vibrational Excitation in Atmospheric Pressure Ns Pulse and RF Plasma Jets. *Plasma Sources Sci. Technol.* **2022**, *under review*.

[113] Jiang, J.; Luo, Y.; Moldgy, A.; Aranda Gonzalvo, Y.; Bruggeman, P. J. Absolute Spatially and Time-resolved O, O_3 , and Air Densities in the Effluent of a Modulated RF-driven Atmospheric Pressure Plasma Jet Obtained by Molecular Beam Mass Spectrometry. *Plasma Process. Polym.* **2020**, *17* (6), 1900163.

[114] Herron, J. T.; Green, D. S. Chemical Kinetics Database and Predictive Schemes for Nonthermal Humid Air Plasma Chemistry. Part II. Neutral Species Reactions. *Plasma Chem. Plasma Process.* **2001**, *21* (3), 459–481.

[115] Nikitin, E. E.; Berry, R. S. Theory of Elementary Atomic and Molecular Processes in Gases. *Phys. Today* **1975**, *28* (12), 54–55.

[116] Hong, J.; Pancheshnyi, S.; Tam, E.; Lowke, J. J.; Prawer, S.; Murphy, A. B. Kinetic Modelling of NH_3 Production in N_2 –H_2 Non-Equilibrium Atmospheric-Pressure Plasma Catalysis. *J. Phys. D. Appl. Phys.* **2017**, *50* (15), 154005.

[117] Jiang, J.; Bruggeman, P. J. Tuning Plasma Parameters to Control Reactive Species Fluxes to Substrates in the Context of Plasma Catalysis. *J. Phys. D. Appl. Phys.* **2021**, *54* (21), 214005.

[118] Esposito, F.; Capitelli, M. QCT Calculations for the Process $N_2(v) + N \rightarrow N_2(v') + N$ in the Whole Vibrational Range. *Chem. Phys. Lett.* **2006**, *418* (4–6), 581–585.

[119] Laporta, V.; Celiberto, R.; Wadehra, J. M. Theoretical Vibrational-Excitation Cross Sections and Rate Coefficients for Electron-Impact Resonant Collisions Involving Rovibrationally Excited N_2 and NO Molecules. *Plasma Sources Sci. Technol.* **2012**, *21* (5), 55018–55028.

[120] Gordiets, B. F.; Ferreira, C. M.; Guerra, V. L.; Loureiro, J. M. A. H.; Nahorny, J.; Pagnon, D.; Touzeau, M.; Vialle, M. Kinetic Model of a Low-Pressure N_2-O_2 Flowing Glow Discharge. *IEEE Trans. Plasma Sci.* **1995**, *23* (4), 750–768.

[121] Gordiets, B.; Ferreira, C. M.; Pinheiro, M. J.; Ricard, A. Self-Consistent Kinetic Model of Low-Pressure - Flowing Discharges: I. Volume Processes. *Plasma Sources Sci. Technol.* **1998**, *7* (3), 363–378.

[122] Capitelli, M.; Ferreira, C. M.; Gordiets, B. F.; Osipov, A. I. Plasma Kinetics in Atmospheric Gases. *Plasma Phys. Control. Fusion* **2001**, *43* (3), 371–372.

[123] Kondeti, V. S. S. K.; Gangal, U.; Yatom, S.; Bruggeman, P. J. Ag^+ Reduction and Silver Nanoparticle Synthesis at the Plasma–Liquid Interface by an RF Driven Atmospheric Pressure Plasma Jet: Mechanisms and the Effect of Surfactant. *J. Vac. Sci. Technol. A Vacuum, Surfaces, Film.* **2017**, *35* (6), 061302.

[124] Li, Y.; Jiang, J.; Hinshelwood, M.; Zhang, S.; Bruggeman, P.; Oehrlein, G. S. Characterization of Plasma Catalytic Decomposition of Methane: Role of Atomic O and Reaction Mechanism. *J. Phys. D. Appl. Phys.* **2021**, *accepted*.

[125] Winters, H. F. Dissociation of Methane by Electron Impact. *J. Chem. Phys.* **2008**, *63* (8), 3462.

[126] Hagelaar, G. J. M.; Pitchford, L. C. Solving the Boltzmann Equation to Obtain Electron Transport Coefficients and Rate Coefficients for Fluid Models. *Plasma Sources Sci. Technol.* **2005**, *14* (4), 722–733.

[127] Pitchford, L. C.; Alves, L. L.; Bartschat, K.; Biagi, S. F.; Bordage, M.-C.; Bray, I.; Brion, C. E.; Brunger, M. J.; Campbell, L.; Chachereau, A.; et al. LXCat: An Open-Access, Web-Based Platform for Data Needed for Modeling Low Temperature Plasmas. *Plasma Process. Polym.* **2017**, *14* (1–2), 1600098.

[128] Nozaki, T.; Muto, N.; Kado, S.; Okazaki, K. Dissociation of Vibrationally Excited Methane on Ni Catalyst: Part 1. Application to Methane Steam Reforming. *Catal. Today* **2004**, *89* (1–2), 57–65.

[129] Hu, Y. H.; Ruckenstein, E. Broadened Pulse-Step Change−Isotopic Sharp Pulse Analysis of the Mechanism of Methane Partial Oxidation to Synthesis Gas. *J. Phys. Chem. B* **1998**, *102* (1), 230–233.

[130] Hu, Y. H; Ruckenstein, E. Multiple Transient Response Methods To Identify Mechanisms of Heterogeneous Catalytic Reactions. *Acc. Chem. Res.* **2003**, *36* (10), 791–797.

[131] Hu, Y. H; Ruckenstein*, E. Isotopic GCMS Study of the Mechanism of Methane Partial Oxidation To Synthesis Gas. *J. Phys. Chem. A* **1998**, *102* (51), 10568–10571.

[132] Ravi, M.; Ranocchiari, M.; van Bokhoven, J. A. The Direct Catalytic Oxidation of Methane to Methanol-A Critical Assessment. *Angew. Chemie Int. Ed.* **2017**, *56* (52), 16464–16483.

[133] Joghee, P.; Malik, J. N.; Pylypenko, S.; O'Hayre, R. A Review on Direct Methanol Fuel Cells–In the Perspective of Energy and Sustainability. *MRS Energy Sustain.* **2015**, *2* (1), 3.

[134] Larkin, D. W.; Lobban, L. L.; Mallinson, R. G. The Direct Partial Oxidation of Methane to Organic Oxygenates Using a Dielectric Barrier Discharge Reactor as a Catalytic Reactor Analog. *Catal. Today* **2001**, *71* (1–2), 199–210.

[135] Nozaki, T.; Okazaki, K. Non-Thermal Plasma Catalysis of Methane: Principles, Energy Efficiency, and Applications. *Catal. Today* **2013**, *211*, 29–38.

[136] Kim, J.; Go, D. B.; Hicks, J. C. Synergistic Effects of Plasma–Catalyst Interactions for CH 4 Activation. *Phys. Chem. Chem. Phys.* **2017**, *19* (20), 13010–13021.

[137] Kim, J.; Abbott, M. S.; Go, D. B.; Hicks, J. C. Enhancing C-H Bond Activation of Methane via Temperature-Controlled, Catalyst-Plasma Interactions. *ACS Energy Lett.* **2016**, *1* (1), 94–99.

[138] Astafan, A.; Batiot-Dupeyrat, C.; Pinard, L. Mechanism and Kinetic of Coke Oxidation by Nonthermal Plasma in Fixed-Bed Dielectric Barrier Reactor. *J. Phys. Chem. C* **2019**, *123* (14), 9168–9175.

[139] De Bie, C.; Van Dijk, J.; Bogaerts, A. The Dominant Pathways for the Conversion of Methane into Oxygenates and Syngas in an Atmospheric Pressure Dielectric Barrier Discharge. *J. Phys. Chem. C* **2015**, *119* (39), 22331–22350.

[140] Lustemberg, P. G.; Palomino, R. M.; Gutiérrez, R. A.; Grinter, D. C.; Vorokhta, M.; Liu, Z.; Ramírez, P. J.; Matolín, V.; Ganduglia-Pirovano, M. V.; Senanayake, S. D.; et al. Direct Conversion of Methane to Methanol on Ni-Ceria Surfaces: Metal-Support Interactions and Water-Enabled Catalytic Conversion by Site Blocking. *J. Am. Chem. Soc.* **2018**, *140* (24), 7681–7687.

[141] Hofmann, S.; van Gessel, A. F. H.; Verreycken, T.; Bruggeman, P. Power Dissipation, Gas Temperatures and Electron Densities of Cold Atmospheric Pressure Helium and Argon RF Plasma Jets. *Plasma Sources Sci. Technol.* **2011**, *20* (6), 065010.

[142] Baiocchi, F. A.; Wetzel, R. C.; Freund, R. S. Electron-Impact Ionization and Dissociative Ionization of the CD_3 and CD_2 Free Radicals. *Phys. Rev. Lett.* **1984**, *53* (8), 771–774.

[143] Itikawa, Y.; Ichimura, A.; Onda, K.; Sakimoto, K.; Takayanagi, K.; Hatano, Y.; Hayashi, M.; Nishimura, H.; Tsurubuchi, S. Cross Sections for Collisions of Electrons and Photons with Oxygen Molecules. *J. Phys. Chem. Ref. Data* **1989**, *18* (1), 23–42.

[144] Fu, H. B.; Hu, Y. J.; Bernstein, E. R. Generation and Detection of Alkyl Peroxy Radicals in a Supersonic Jet Expansion. *J. Chem. Phys.* **2006**, *125* (1), 014310.

[145] Meloni, G.; Zou, P.; Klippenstein, S. J.; Ahmed, M.; Leone, S. R.; Taatjes, C. A.; Osborn, D. L. Energy-Resolved Photoionization of Alkylperoxy Radicals and the Stability of Their Cations. *J. Am. Chem. Soc.* **2006**, *128* (41), 13559–13567.

[146] Nixon, K. L.; Pires, W. A. D.; Neves, R. F. C.; Duque, H. V.; Jones, D. B.; Brunger, M. J.; Lopes, M. C. A. Electron Impact Ionisation and Fragmentation of Methanol and Ethanol. *Int. J. Mass Spectrom.* **2016**, *404*, 48–59.

[147] Zawadzki, M. Electron-Impact Ionization Cross Section of Formic Acid. *Eur. Phys. J. D* **2018**, *72* (1), 12.

[148] Vacher, J. R.; Jorand, F.; Blin-Simiand, N.; Pasquiers, S. Partial Ionization Cross-Sections of Acetone and 2-Butanone. *Int. J. Mass Spectrom.* **2008**, *273* (3), 117–125.

[149] Możejko, P. Calculations of Electron Impact Ionization Cross Section for Simple Biomolecules: Formic and Acetic Acids. *Eur. Phys. J. Spec. Top. 2007 1441* **2007**, *144* (1), 233–237.

[150] Loenders, B.; Engelmann, Y.; Bogaerts, A. Plasma-Catalytic Partial Oxidation of Methane on Pt(111): A Microkinetic Study on the Role of Different Plasma Species. *J. Phys. Chem. C* **2021**, *125* (5), 2966–2983.

[151] Greenler, R. G. Infrared Study of the Adsorption of Methanol and Ethanol on Aluminum Oxide. *J. Chem. Phys.* **1962**, *37* (9), 2094–2100.

[152] Korhonen, S. T.; Bañares, M. A.; Fierro, J. L. G.; Krause, A. O. I. Adsorption of Methanol as a Probe for Surface Characteristics of Zirconia-, Alumina-, and Zirconia/Alumina-Supported Chromia Catalysts. *Catal. Today* **2007**, *126* (1–2), 235–247.

[153] Schauermann, S.; Hoffmann, J.; Johánek, V.; Hartmann, J.; Libuda, J. Adsorption , Decomposition and Oxidation of Methanol on Alumina Supported Palladium Particles. *Phys. Chem. Chem. Phys.* **2002**, *4* (15), 3909–3918.

[154] Plessis, P.; Marmet, P.; Dutil, R. Ionisation and Appearance Potentials of CH_4 by Electron Impact. *J. Phys. B At. Mol. Phys.* **1983**, *16* (7), 1283–1294.

[155] Nozière, B.; Hanson, D. R. Speciated Monitoring of Gas-Phase Organic Peroxy Radicals by Chemical Ionization Mass Spectrometry: Cross-Reactions between CH_3O_2, $CH_3(CO)O_2$, $(CH_3)_3CO_2$, and c-$C_6H_{11}O_2$. *J. Phys. Chem. A* **2017**, *121* (44), 8453–8464.

[156] Jiang, J.; Santosh K Kondeti, V. S.; Nayak, G.; Bruggeman, P. J. Experimental and Modeling Studies of the Plasma Chemistry in a Humid Ar Radiofrequency Atmospheric Pressure Plasma Jet. *J. Phys. D. Appl. Phys.* **2021**, *submitted*.

[157] Agarwal, N.; Freakley, S. J.; McVicker, R. U.; Althahban, S. M.; Dimitratos, N.; He, Q.; Morgan, D. J.; Jenkins, R. L.; Willock, D. J.; Taylor, S. H.; et al. Aqueous Au-Pd Colloids Catalyze Selective CH_4 Oxidation to CH_3OH with O_2 under Mild Conditions. *Science.* **2017**, *358* (6360), 223–227.